



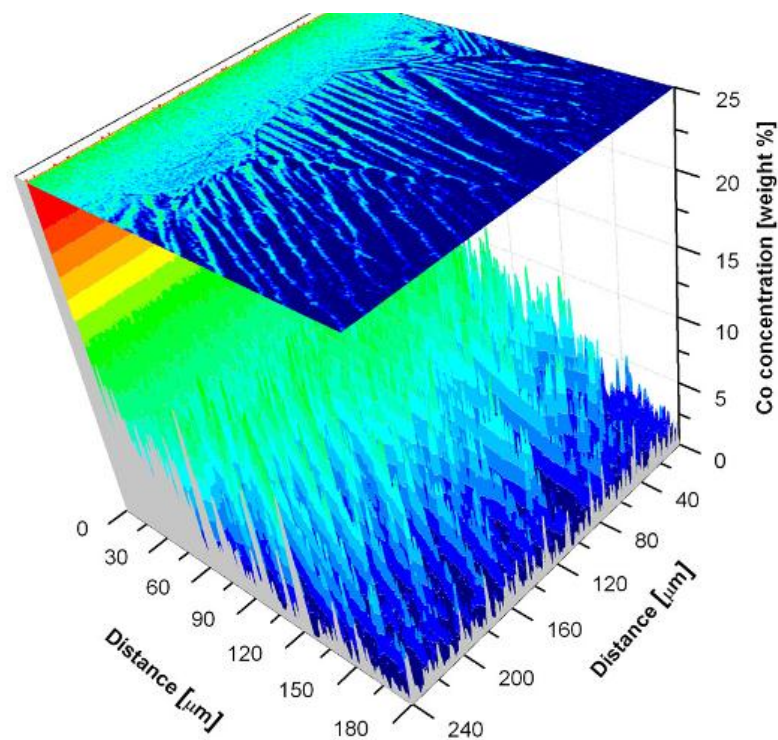
UNIVERSITY
OF TRENTO - Italy

Department of Materials Engineering
and Industrial Technologies

Doctoral School in Materials Science and Engineering – XXIV cycle

SPARK PLASMA SINTERING OF TITANIUM AND COBALT ALLOYS FOR BIOMEDICAL APPLICATION

Nério Vicente Junior



April 2012

**SPARK PLASMA SINTERING OF TITANIUM AND COBALT
ALLOYS BY FOR BIOMEDICAL APPLICATION**

Nério Vicente Junior

Tutor:

Prof. Alberto Molinari

Doctoral Committee:

Prof. Paolo Scardi – University of Trento (ITA)

Prof. Scott Misture – Alfred University (USA)

Prof. Silvia L. Cuffini – Federal University of Santa Catarina (BRA)

26th April 2012

To my parents and my wife.

INDEX

CHAPTER 1 - INTRODUCTION	7
1.1 - GENERAL ASPECTS	7
1.2 - OBJECTIVES	8
1.3 - THESIS OVERVIEW	9
CHAPTER 2 - THEORETICAL FRAMEWORK	11
2.1 - BIOMATERIALS	11
2.1.1 - Introduction	11
2.1.2 - Requirements of Biomaterials	12
2.1.2.1 - Mechanical Properties	12
2.1.2.2 - Corrosion Resistance	13
2.1.2.3 - Biocompatibility	14
2.2 - POROUS STRUCTURES	15
2.2.1 - Introduction	15
2.2.2 - Fabrication Methods	17
2.2.3 - Scaffolds	20
2.3 - BIOMEDICAL ALLOYS	21
2.3.1 - Cobalt and its alloys	21
2.3.1.1 - Introduction	21
2.3.1.2 - Cobalt Alloys	22
2.3.1.3 - Co-28Cr-6Mo	23
2.3.2 - Titanium and its alloys	24
2.3.2.1 - Introduction	24
2.3.2.2 - Titanium alloys	25
2.3.2.3 - Ti-6Al-4V	26
2.4 - PULSED ELECTRIC CURRENT SINTERING	28
2.4.1 - Introduction	28
2.4.2 - Heating Mechanisms	29
2.4.3 - Processing and Manufacturing	30
CHAPTER 3 - EXPERIMENTAL PROCEDURES	32
3.1 - SPS APPARATUS AND SINTERING CYCLE	32
3.2 - SAMPLES PREPARATION	32
3.3 - METALLOGRAPHIC MICROSTRUCTURE INVESTIGATION	33
3.4 - DENSITY	33

3.5 - POROSITY _____	33
3.6 - X-RAY DIFFRACTION _____	37
3.7 - HARDNESS AND MICROHARDNESS _____	38
3.8 - ADHESION TEST _____	38
3.9 - STATIC SHEAR TEST _____	38
3.10 - FATIGUE SHEAR TEST _____	39
3.11 - ABRASION TEST _____	39
3.12 - TENSILE TESTS _____	39
3.13 - REVERSE BENDING FATIGUE TEST _____	39
3.14 - OPEN CIRCUIT POTENTIAL TEST _____	40
3.15 - CYCLIC POTENTIODYNAMIC POLARIZATION TEST _____	41
CHAPTER 4 - POROUS STRUCTURE _____	42
4.1 - SCAFFOLD PREPARATION _____	43
4.2 - MORPHOLOGICAL ASPECTS _____	45
4.2 - POROSITY CHARACTERIZATION _____	51
4.3 - INTERFACIAL INTERACTIONS _____	52
4.4 - MECHANICAL PROPERTIES _____	54
4.4.1 - Adhesion Test _____	54
4.4.2 - Static Shear Test _____	55
4.4.3 - Fatigue Shear Test _____	55
4.4.4 - Taber Abrasion Test _____	56
4.5 - SUMMARY OF THE RESULTS _____	57
CHAPTER 5 - FULL DENSITY SUBSTRATES _____	59
5.1 Co-28Cr-6Mo _____	59
5.1.1 - Powder Microstructure _____	59
5.1.2 - Effect of Sintering Temperature _____	61
5.1.2.1 - Relative Density _____	68
5.1.3 - Effect of Pressure _____	70
5.1.4 - Influence of Powder _____	74
5.1.5 - Mechanical Properties _____	79
5.1.5.1 - Tensile properties _____	79
5.1.5.2 - Fatigue Properties _____	83
5.1.6 - Corrosion Properties _____	85
5.1.6.1 - Open Circuit Potential (OCP) Test _____	85
5.1.6.2 - Cyclic Potentialdynamic Polarization (CPP) Test _____	86
5.2 - Ti-6Al-4V _____	88
5.2.1 - Mechanical Properties _____	88
5.2.1.1 - Tensile Properties _____	89

5.2.1.2 - Fatigue Properties _____	92
5.2.2 - Corrosion Properties _____	93
5.2.2.1 - Open Circuit Potential (OCP) Test _____	93
5.2.3.2 - Cyclic Potentialdynamic Polarization (CPP) Test _____	94
5.3 - SUMMARY OF THE RESULTS _____	95
CHAPTER 6 - CO-SINTERING _____	97
6.1 - CP-Ti/CO-28CR-6MO _____	97
6.1.1 - Microstructure _____	97
6.1.2 - Sinter-bonding _____	100
6.1.3 - Interface Characterization _____	102
6.1.4 - Fatigue Properties _____	109
6.2 - CP-Ti/TI-6AL-4V _____	111
6.2.1. Microstructure _____	111
6.2.2 - Interface Characterization _____	112
6.2.2 - Fatigue Properties _____	116
6.3 - SUMMARY OF THE RESULTS _____	117
CHAPTER 7 - CONCLUSIONS _____	120
REFERENCES _____	121
ACKNOWLEDGEMENTS _____	134
PUBLICATIONS _____	135

Chapter 1 - INTRODUCTION

1.1 - General Aspects

Commercial pure titanium (cp-Ti), Ti-6wt.%Al-4wt.%V (Ti-6Al-4V) and Co-28wt.%Cr-6wt.%Mo (Co-28Cr-6Mo) alloys are nowadays the most worldwide applied metals in orthopedic field (along with AISI316L stainless steel) due to their good mechanical properties, corrosion resistance and biocompatibility. In the case of Powder Metallurgy products, mechanical and corrosion resistance are maximized by a full density microstructure, but in the case of tissue regeneration, a porous structure (scaffold) is an essential characteristic. Scaffolds have been extensively assessed by the scientific community as the best design for bone regeneration because they mimic the architecture of the trabecular portion of the bone. They facilitate a prompt extra cellular matrix recognition, rapid healing and bone stable interlocking. However, a porous structure has poor mechanical properties, mainly fatigue resistance, and therefore it has to be combined with a full density substrate for long withstand applications.

The Co alloy is used in the biomedical field since 50 years. It is produced mainly by investment casting and utilized for those applications where high wear resistance is required. Numerous studies have been carried out in order to improve its mechanical properties by modifying the microstructural characteristics and some Powder Metallurgy processes (HIP, MIM, SLM, EBM) are contributing to this objective.

The Ti alloy was firstly developed for aircraft applications owing to its high weight-to-strength ratio. The excellent corrosion resistance supported the

development of the applications in biomedical field. It is more resistant to mechanical loading than pure titanium with minimal biocompatibility losses. Forging is the main process utilized to produce components made of Ti-6Al-4V alloy, since interstitials pick-up arises as a serious problem in casting, resulting in severe ductility loss. Even in this case, Powder Metallurgy is an excellent technological alternative based mainly on HIP, MIM, SLM, EBM.

Commercial pure titanium is effectively the best biocompatible material among those investigated in this work, and it was chosen for the production of the porous scaffold. It has modest mechanical property and therefore it does not have applications as structural material, even in the biomedical field. It faces the same technological difficulties of any other titanium alloy, and can be successfully produced by Powder Metallurgy by the above mentioned routes.

1.2 - Objectives

This work was carried out in the frame of an industrial research project in cooperation with K4Sint Srl (Pergine Valsugana, Trento), and Eurocoating SpA (Pergine Valsugana, Trento) aimed at the development of the production of commercial pure titanium (cp-Ti), Ti-6wt.%Al-4wt.%V (Ti-6Al-4V) and Co-28wt.%Cr-6wt.%Mo (Co-28Cr-6Mo) alloys by Spark Plasma Sintering for biomedical application. The final objective is the definition of the process parameters for the production of a highly porous (cp-Ti), full density materials (Ti-6Al-4V and Co-28Cr-6Mo), and their combination in a surface functionalized full density substrate.

1.3 - Thesis Overview

Gas atomized pre-alloyed powders and the Spark Plasma Sintering (SPS) process were employed to manufacture the specimens. SPS is an emerging Powder Metallurgy process, which makes use of a pulsed electric current and a compaction pressure for densification and sintering of powders. It is particularly suitable to process hard-to-sinter powders to the full density with a strict control of the microstructure, due to the relatively low heat input.

Co-sintering and sinter-bonding were the processing approaches used to join the scaffold and the full density substrate. Actually, the scaffold consisted in a sort of blend (cp-Ti/CP) during sintering with subsequent space holder extraction; this ensures a careful control of the final porosity volume fraction, shape and size. The porous scaffold was produced by means of the space holder technique, making use of calcium phosphate (CP) particles.

The thesis is organized in the following chapters. In chapter 2 the theoretical framework is presented. In chapter 3 the methodology and characterization techniques are presented. Chapter 4 deals with the porous scaffold. The microstructural and morphological characteristics, as well as some mechanical and wear properties of the porous material are presented. Chapter 5 deals with the full density materials: density, microstructure, hardness and microhardness, tensile and fatigue, as well as corrosion properties are presented and discussed for the Co-28Cr-6Mo alloy and Ti-6Al-4V alloys. In chapter 6 the co-sintering and sinter-bonding approaches to produce the porous scaffold on a full density substrate are presented. Attention is focused not only on density and microstructure, but

even on the interfaces between the cp-Ti and Ti-6Al-4V and the Co-28Cr-Mo substrates. Interdiffusion of alloying elements was verified. Bending fatigue tests were also carried out on specimens representative of the scaffold coated full density materials. The conclusive remarks are summarized in Chapter 7.

Chapter 2 - THEORETICAL FRAMEWORK

2.1 - BIOMATERIALS

2.1.1 - Introduction

Materials in medicine date back to ancient civilizations in India, China and Egypt, where the medicine was practiced as part of the religious and mystical activities. Metallurgical tools were used for surgical treatment, tendons for suture etc. The first implanted material was gold plate for cleft palate in 1588. Till the polymer industry was developed in 1950s, the metallic materials like silver, platinum, stainless steel and cobalt base alloys were mainly used. [1]

A biomaterial is a synthetic material used to replace part of a living system or function in intimate contact with living tissue [2]. Another definition is proposed by [3]: a biomaterial is defined as any systemically, pharmacologically inert substance or combination of substances utilized for implantation within or incorporation with a living system to supplement or replace functions of living tissues or organs.

More recently, Guelcher said that a biomaterial is a material that has been shown to be compatible with living tissue and that demonstrates suitable structural and mechanical stability for its desired use [4]. Here, the definition takes also an engineering point of view using the structural and mechanical stability concepts, being in this way much closer to the actual successful of long term implantation.

A biomaterial may act as a biological device that substitute or repair bone, cartilages, ligaments or tendons. To be utilized in bone repair or bone

substitute a material of course must be comparable to the bone in terms of mechanical properties. In practice, it does not must be chemically comparable to the bone, but at least it must show inertness in order to avoid implant rejection. Requirements of biomaterials are nowadays very well understood thanks to common efforts of doctors, biologists and engineers.

2.1.2 - Requirements of Biomaterials

The design and selection of the biomaterial depend on the medical application. Regardless the application, a biomaterial must be non-carcinogenic, non-allergic and nontoxic [5]. Others prerequisites concerning biomaterials are related to the material reliability, whose are: mechanical properties (2.1.3) and corrosion properties (2.1.4) and minimal material-to-bone affinity, that is, biocompatibility.

2.1.2.1 - Mechanical Properties

For orthopedic biomaterials the prime mechanical properties are elastic modulus, tensile strength and elongation, fatigue resistance and wear resistance [6,7,8]. In majority of the cases fatigue is the cause of prosthesis failure [7,8].

A high tensile strength and high elongation lead to a high toughness. This is the motive why metals are usually chosen for orthopedics. Commonly, ceramics show high strength, but very limited elongation, leading to a poor toughness. Wear resistance, on the other hand, is occasionally a weakness point of metallic materials. Low wear resistance may results in metallic ions releasing. The released ions are found to cause allergic and toxic reactions [9,10].

Elastic modulus (stiffness), differently to tensile, fatigue and wear resistance, is a property which promotes the improvement of biological reactions. Material for bone replacement is expected to have a stiffness equivalent to that of bone. The elastic modulus of the bone varies from 4 to 30 GPa depending on the type of the bone and the direction of measurement [11], whilst that of customary metallic biomaterials is between 100-200 GPa [5]. Elastic modulus mismatch among the metallic biomaterial and the surrounding bone has been identified as a major reason for implant loosening due to stress shielding [12].

Porous structure is a current approach to overcome the problem of high elastic modulus intrinsic to the metallic biomaterials. Literature concerning this topic is revised in the successive section (2.2).

2.1.2.2 - Corrosion Resistance

Metal implant corrosion is controlled by:

- (1) the extent of the thermodynamic driving force;
- (2) physical barriers which limit the kinetics of corrosion.

Orthopedic alloys rely on the formation of passive films to prevent significant corrosion [13].

These films consist of metal oxides (ceramic films) which form spontaneously on the surface of the metal in such a way that they prevent further transport of metallic ions and/or electrons across the film. To be effective barriers, the films must be compact and strongly adherent on the metal surface; they must have an atomic structure that limits the migration of ions and/or electrons across the metal oxide–solution interface; and they must be able to remain on the surface of the alloys even when mechanically stressed or abraded [13].

Even with a passivated metal, there will be a finite rate of diffusion of ions through the oxide layer, and possible minimal dissolution of the layer itself. [5]

Some specific mechanism of corrosion are listed:

Pitting corrosion is a localized accelerated dissolution of metal that occurs as a result of a breakdown of the protective passive film on the metal surface. Metallic biomaterials as stainless steels, cobalt alloys and titanium when exposed to chloride ions and sufficiently positive potential, lead to breakdown, giving rise to pits. Stainless steels are unlikely to resist pitting when exposed to the body fluids indefinitely; the cobalt-based alloys may well withstand such exposure for long times; titanium and some of its alloys should withstand such exposure for an indefinite period [14].

Fretting corrosion takes place when the passive layer is removed by mechanical process leaving the metallic material vulnerable. In this case wear resistance is also concerned. Moreover, the ability to re-passivate is of great importance. In joint implants, fretting corrosion is produced by relatively small-scale (< 100 μm) motions between components induced by cyclic loading. The motion may increase corrosion rates because oxide layers are continually fractured and reformed [15].

Galvanic corrosion can take place if two different metals are placed in contact within the same solution. Electrons passing from the more anodic to the more cathodic metal induce continuous dissolution. Evidences of this type of corrosion have been exposed [16].

2.1.2.3 - Biocompatibility

A biomaterial distinguishes from any other material for its ability to stay in contact with the pertinent tissues of the human body, or components of

tissues, without producing an unacceptable degree of injury to those tissues or components [17].

According to [18], the term biocompatibility is misused if treated simply as the evaluation of cell culture onto the material (in vitro test). This term refers to a collection of mechanisms involving different but independent reactions between a material and its host tissue.

Biocompatibility refers to ability of material to perform a function depending not only on its interaction with tissue but also on the intrinsic mechanical and physical properties [18]. A successful long term usage has to be considered.

Osteointegration is another term used in biomedical science. Now, the material-to-tissue interaction is concerned in mechanical point of view. From [19], osteointegration is a condition “in which solid anchoring of an alloplastic material in bone is achieved, and retained under functional loading” [20]. Therefore, surface composition, hydrophilicity, porosity and roughness are parameters that influence the rate and quality of osseointegration [21].

2.2 - POROUS STRUCTURES

Regarding the mechanical requirements and the biocompatibility of biomaterials a precise feature is desired for orthopedic implants: porous structure. Summarily, it is positive for reducing stiffness and in turn it offers a support for bone fixation.

2.2.1 - Introduction

Despite of the high corrosion resistance exhibited by ceramic materials, they cannot be employed as load bearing implants, due to their intrinsic

brittleness. Polymeric materials, on the other hand, cannot withstand to cyclic loading during long time (low fatigue resistance). Alternatively, metallic materials portray high toughness, high fatigue resistance, corrosion resistance and biocompatibility. Porous structure made of metals are then suitable for orthopedic implantation in the case of long term application.

The three leaders metallic materials used to fabricate porous structures (foams) are aluminum, magnesium and titanium. In the majority, research of metallic foams processing has been focused on melt-processing of aluminum foams with open or closed cells [22], owing to the low melting point (662°C) and low reactivity of molten Al [23]. Nevertheless, titanium is by far the metallic material with best properties for biomedical use [6]. It has a melting point of 1670°C and, in this case, powder metallurgy emerges as the main feasible route to produce foams.

Titanium foams are largely used in structural applications (closed pores) thanks to their exceptional density-compensated strength and corrosion resistance. But currently, biomedical application has taken further attention [24].

The foam properties are controlled by the pore feature, i.e. size, shape, volume percentage, interconnection, surface area and uniformity of pores, which may be rather different in various fabrication methods [25].

Figure 2.1 shows some foam and dense materials properties. The vast list of properties shown by foams in general cannot be obtained by dense materials.

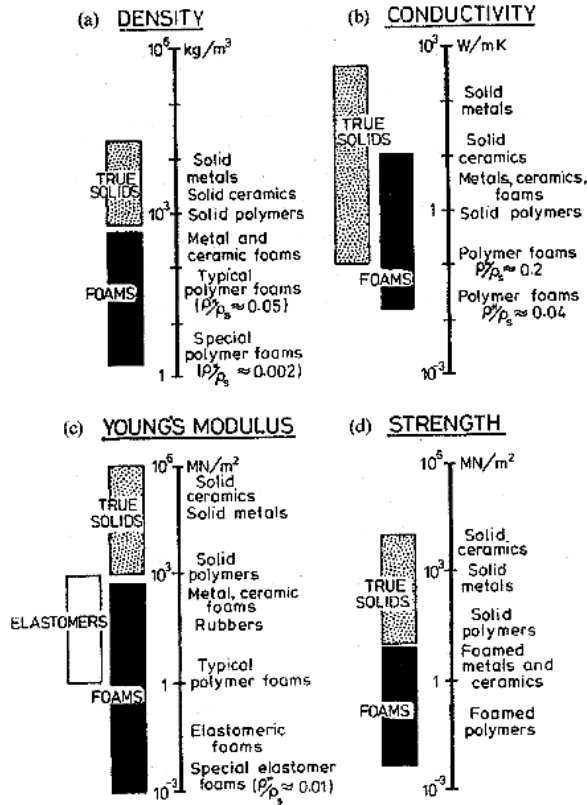


Fig. 2.1 - Properties range of foams and full density materials [26].

2.2.2 - Fabrication Methods

Ryan *et al* [27], reviewed the fabrication methods of porous structures made of metals for use in orthopedic applications. Pore distribution was selected as the main aspect to discriminate the methods. Into the fabrication methods of non-homogeneous pores distribution accounted: furnace sintering, space holder, replication and combustion synthesis; homogenous pore distribution: orderly oriented wire mesh, ferromagnetic fibres and vapor deposition; and functionally graded pore distribution: electric field assisted sintering and rapid prototyping. Some of non-

homogenous and functionally graded material methods further are presented.

Furnace sintering of loose powders or powder beads. It is based on the partial sintering of powders in order to keep voids between particles. This method is utilized either for manufacturing full porous structure or porous surfaced materials. Pores are rather irregular. The volume of pores depend on several parameters, such as: chemical composition, powder size, powder distribution, powder shape, compaction pressure and sintering temperature. The application of this method in the biomedical field has its roots on 70's, with Galante [28] and Pilliar [29], whose published and patented their results, respectively. Several authors have dealt with this method [30-33].

Space holder method consists in the mixing of at least two types of particles, one to form the structural framework after sintering and another (space holder) used to create a collection of pores. The latter is usually extracted after shaping, but in some cases can be extracted after sintering. In principle, space holder particles must touch one each other, creating a continuous channel, in order to allow the extraction of material. Pore features are changeable by varying the space holder feature. High amount of porosity can be achieved (~70%), but in some cases warping may be a drawback. [Fig. 2.2](#) schematically shows the steps of space holder method. Several authors have worked with this method [34-40].

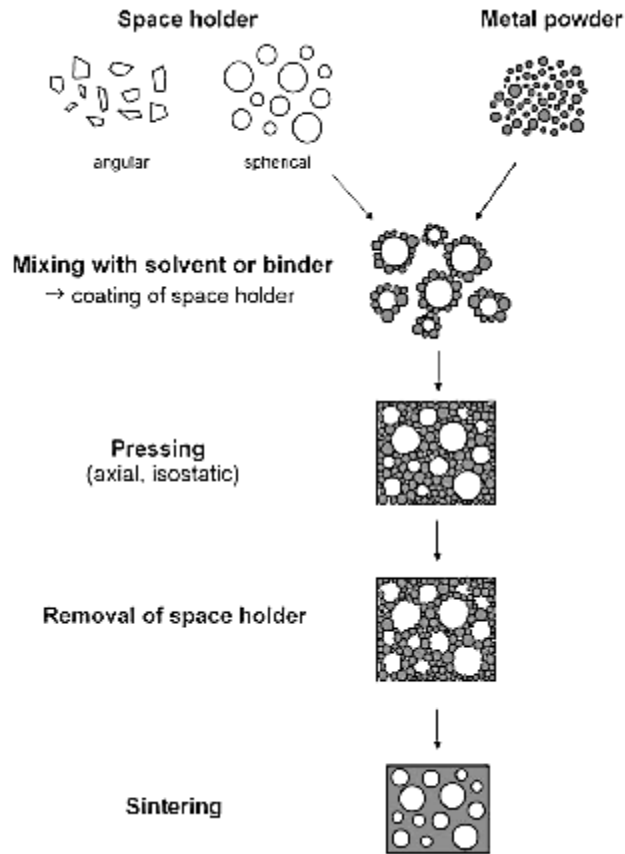


Fig. 2.2 - Process steps in space holder method [34].

Rapid prototyping is the most powerful method for porous structure manufacturing. It is based on the application of a beam (laser or electrons) to melt or to sinter powders. The pores assembly is defined by means of computer aided design (CAD) platform, and therefore it has a practically unlimited architecture. A limitation regards the pore size since it is normally linked to the beam thickness and the powder particles diameter. One interesting use is the manufacturing of prosthesis with proper complex design, such as used to maxillary reconstruction. A potential drawback is the formation of metastable phases due to extremely high cooling rate. Several authors have worked with this method [41-44].

2.2.3 - Scaffolds

A scaffold is an artificial three-dimensional frame structure that serves as a mimic of extracellular matrix for cellular adhesion, migration, proliferation, and tissue regeneration in three dimensions [45].

In the case of orthopedic applications the scaffold must offer an appropriate surface to cell adhesion (differentiation and proliferation) as well as an appropriate assembly to latter bone interlocking. The former focus is intensely related to surface chemistry while the last regards the design of the scaffold.

The bone is formed by two main constituents: the compact (cortical) and the trabecular (cancellous) bone. The former is hard, shows some porosity and is situated at outer part, acting as a wall. The latter is stiff, highly porous and is located on the inner part [46]. Fig. 2.3 shows a schematic of the bone [47].

Compact Bone & Spongy (Cancellous Bone)

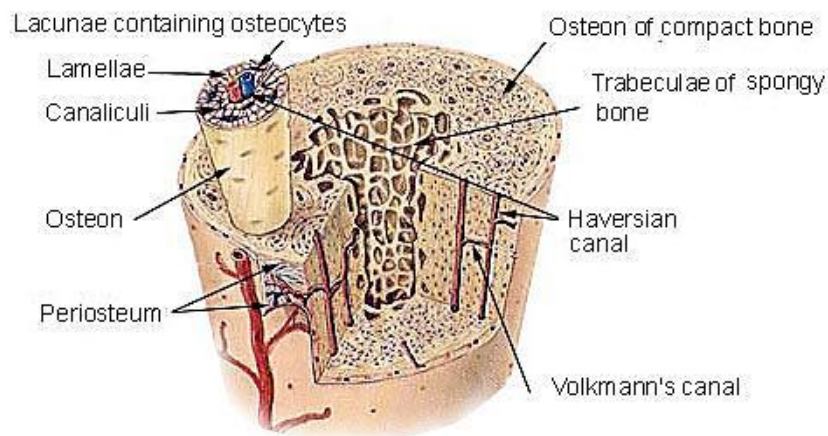


Fig. 2.3 – The bone structure [47].

A proper scaffold for bone regeneration must be similar to the trabecular bone in design and mechanical properties.

2.3 - BIOMEDICAL ALLOYS

2.3.1 - Cobalt and its alloys

2.3.1.1 - Introduction

Isolated in 1735 by Brandt, the cobalt element had its true nature extensively studied about 40 years later by Bergman. Cobalt situates in the transition group VIII, between iron and nickel, in the Mendeleef's periodic table [48].

Metallurgical uses of cobalt include the wear resistant, corrosion resistant, and heat resistant cobalt-based alloys, the use of cobalt in nickel-base superalloys (the largest end-use sector for cobalt), iron-based superalloys, cemented carbides, magnetic materials, low expansion alloys, steels, and, to a lesser extent, nonferrous alloys and cobalt coatings [49].

Cobalt exists in two atomic forms: a low temperature stable hexagonal close packed (h.c.p.) form and a high temperature stable face centered cubic (f.c.c.) form. The transformation temperature of pure cobalt is 417 °C. Alloying elements such as nickel, iron, and carbon (within its soluble range) are known as f.c.c. stabilizers, and, suppress the transformation temperature. Chromium, molybdenum, and tungsten, on the other hand, are h.c.p. stabilizers and have the opposite effect. [50]

Actually, the transformation is extremely sluggish, and most cobalt-base alloys exhibit a (metastable) f.c.c. structure at room temperature, even if their transformation temperatures are considerably higher. Partial transformation (from f.c.c. to h.c.p.) of most cobalt-based alloys is, however, easily induced at room temperature by plastic deformation (under the action of mechanical stress), also called strain induced martensitic transformation [51,52], the extent of the transformation being related to the composition (in particular the ratio of h.c.p. stabilizers to f.c.c. stabilizers).

The transformation under stress progresses by the creation of large stacking faults (the f.c.c. form of these alloys having very low stacking fault energies) and by subsequent coalescence. Extensive micro twinning is also observed in plastically-deformed, cobalt based alloys. Crystal structure of cobalt are shown in Fig. 2.4.

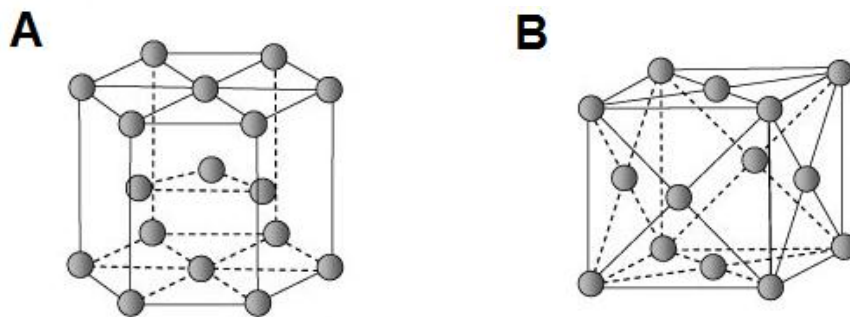


Fig. 2.4 - Crystal structures of cobalt. A) Martensite (h.c.p.) and B) Alpha phase (f.c.c.)

2.3.1.2 - Cobalt Alloys

Cobalt-base alloys are strengthened either by solid-solution on the matrix or by precipitation of carbides. While the first is correlated to stress imposed by distortion in the atomic arrangement the last regards the presence of hard particles distributed both on the matrix and at grain boundaries.

Element usually added to solid-solution strengthen are chromium, tungsten, niobium and tantalum. But normally, chromium is added with the aim of confer corrosion resistance by forming oxides on the surface.

Tungsten and molybdenum serve to provide additional strength to the matrix, owing to the virtue of their large atomic size. When present in large quantities, they participate in the formation of carbides during alloy solidification and promote the precipitation of M_6C ; molybdenum may also form intermetallic compounds with cobalt [53].

The second-phase strengthening (precipitates) in cobalt-based alloys is achieved by the addition of carbon or nitrogen. Both elements can form compounds with high hardness (carbides or carbonitrides). Some types of carbides can be formed in cobalt-based alloys, such as MC, M_6C , M_7C_3 , $M_{23}C_6$ and occasionally M_2C_3 .

The strengthening mechanisms provided by solid solution elements and precipitates are different, mainly when the latter is located at grain boundary. Solid solution of elements contribute to strengthen by adding internal stress and defects. Carbides when located within the grain provide obstacles to the movement of dislocations also second phase, and thus inhibiting slip. At grain boundaries the precipitates prevent gross sliding [48].

2.3.1.3 - Co-28Cr-6Mo

Cobalt-chromium-molybdenum-carbon alloys are widely employed in aircraft engines and prosthetic implants. High strength and wear resistance are the main properties of this alloy, but high chromium quantities afford very good corrosion resistance in chloride environments.

As cast Co-28Cr-6Mo alloy shows some microstructures features that result in tensile and fatigue properties losses. Microstructural inhomogeneities observed in cast Co-Cr-Mo alloy include porosity, coring, oxides, sigma phase formation, large grains and grain boundary precipitates [54]. These adversities are intrinsic to the cast processing and some of them can be eliminated by post thermomechanical treatments.

Powder Metallurgy appears as an attractive technology to process the Co-28Cr-6Mo alloy due to the prospective of microstructure control.

Using the traditional press-and-sinter P/M process, [55] obtained a Co-28Cr-6Mo alloy with only 0,02% of porosity when sintered at 1350°C during

90 minutes in inert gas. Moreover, grains do not growth excessively, reaching up to 87 μm . Metal Injection Moulding (MIM) [56], Electron Beam Melting (EBM) [57] and Selective Laser Melting (SLM) [58] are also suitable P/M technologies.

2.3.2 - Titanium and its alloys

2.3.2.1 - Introduction

Discovered in England by Gregor in 1790, the element titanium was denominated five years later by Klaproth. Its name remind the mythological first sons of the earth, the Titans. Titanium is one of the transition elements in group IV and period 4 of Mendeleef's periodic table. It has an atomic number of 22 and an atomic weight of 47.9. Being a transition element, titanium has an incompletely filled d shell in its electronic structure [59].

Titanium has a high melting point (1668 $^{\circ}\text{C}$) and possesses a hexagonal closely packed crystal structure alpha (h.c.p.) (Fig. 2.5A) up to a temperature of 882,5 $^{\circ}\text{C}$. Titanium transforms into a body centered cubic structure beta (b.c.c.) (Fig. 2.5B) above this temperature [60].

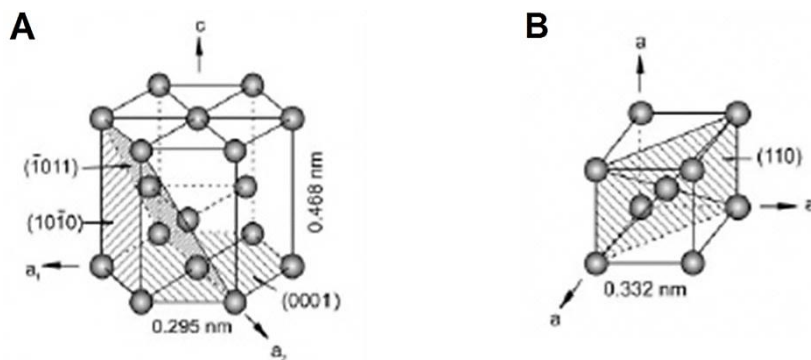


Fig. 2.5 - Crystal structures of titanium. A) alpha phase (h.c.p.) and B) Beta phase (b.c.c.) [59]

Titanium is worldwide recognized as a metal with high strength-to-weight ratio, high corrosion resistance and chemical inertness. These properties have pushed the research in order to minimize production costs.

Titanium and its alloys are strategic advanced materials for high performance requirements, being systematically used in aircraft, aerospace, jet engine, chemical and petroleum, automotive and biomedical. Some biomedical applications are reported in [Table 2.1](#).

[Table 2.1](#) - Some biomedical application of Titanium and its alloys.

Artificial joint prostheses
Bone plates, intramedullary rods, etc.
Heart valves
Dental implants
Attachment wire
Surgical instruments
Wheelchairs

2.3.2.2 - Titanium alloys

Titanium alloys can be classified as alpha, near-alpha, alpha + beta, metastable beta, or stable beta depending on the room temperature microstructure [61].

In pure titanium beta phase is stable only at high temperature. At given amount of specific alloying elements this beta phase is hindered on cooling. If such elements are added in a high amount the beta phase can be full hindered, but sensitive to be transformed in alpha (metastable beta), at still higher amounts the full stable beta phase is achieved ([Fig. 2.6](#)).

Alloying elements usually added in titanium may be divided in three categories:

- (i) Alpha-stabilizers, such as Al, O, N, C;
- (ii) Beta-stabilizers, such as Mo, V, Nb, Ta (isomorphous), Fe, W, Cr, Si, Co, Mn, H (eutectoid);
- (iii) Neutrals, such as Zr.

The effect of beta stabilizer elements on the phase diagram can be seen in Fig. 2.6.

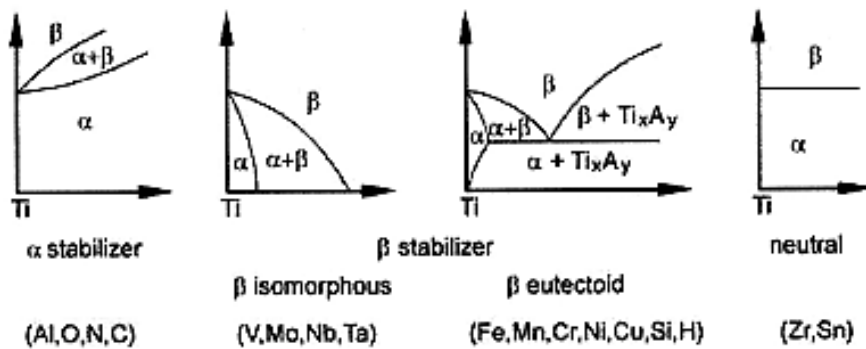


Fig. 2.6 - Schematic effect of alloying elements on phase diagrams of Ti alloys [62].

The properties of the alpha + beta alloys depend on the chemical composition, relative amounts and arrangement of phases, and the processing history [63].

2.3.2.3 - Ti-6Al-4V

Developed in 50's in the United States at the Illinois Institute of Technology Among the Ti-6Al-4V alloy is the most widespread alpha + beta titanium alloy. More than 50% of all alloys in use today are of this composition [61].

The alpha + beta microstructure can be modified by heat treatment as well as thermomechanical treatment [64]. Fig. 2.7 shows some of these microstructures.

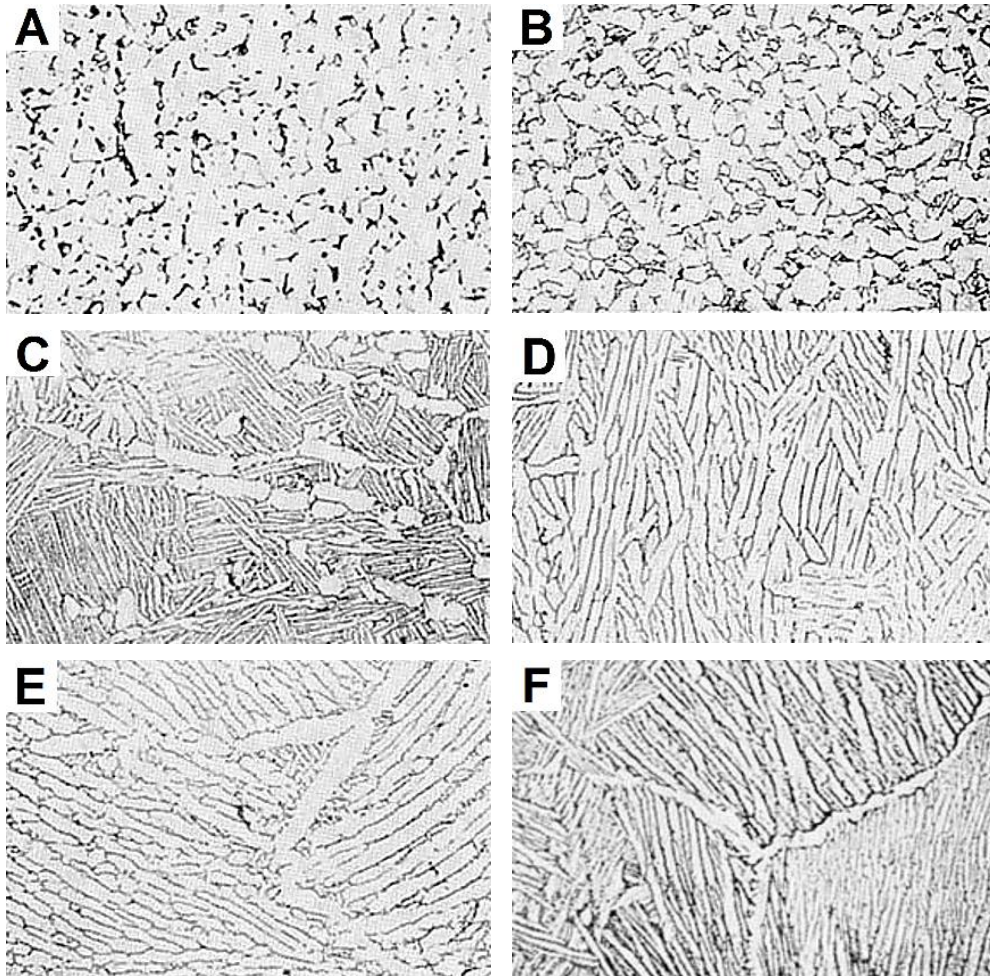


Fig. 2.7 - Microstructure of an alpha-beta titanium alloy (Ti-6Al-4V) in representative metallurgical conditions. (a) Equiaxed alpha and alpha small amount of intergranular beta. (b) Equiaxed and acicular alpha and a small amount of intergranular beta. (c) Equiaxed alpha in an acicular alpha matrix. (d) Small amount of equiaxed alpha in an acicular alpha matrix. (e) Plate-like acicular alpha (transformed beta); alpha at prior beta grain boundaries. (f) Blocky and plate-like acicular alpha; α at prior beta grain boundaries [65]

Although the recognized potential of titanium and its alloys there is a limitation in their application in consequence of high price [66]. The high cost of producing titanium-based materials as compared to competing materials has led to investigations of potentially lower cost processes, such as net-shape powder metallurgy (P/M) techniques [67,68]. Titanium P/M fabrication offers the potential for true net shape capability combined with mechanical properties that are equal to, or exceed, cast and wrought products [63]. Titanium P/M has been developed as a net-shape technique only in the last 20 years. According to the raw material, P/M can be divided into two major categories [69]:

i) Elemental Blend (BE), in which a blend of elemental powders, along with master alloy or other desired additions, is cold pressed into shape and subsequently sintered to higher density and uniform chemistry; ii) Pre-alloyed (PA), which is based on hot consolidation of powder produced from a pre-alloyed stock. Hot Isostatic Pressing (HIP) is the primary hot consolidation method for PA powders, but vacuum hot pressing (VHP), extrusion, and rapid omnidirectional compaction (ROC) have also been successfully used [70]. Some Advanced P/M techniques used to consolidate titanium powders are: i) Metal Injection Moulding (MIM) [71]; ii) Electron Beam Melting (EBM) [72]; iii) Selective Laser Melting [73]; iv) Spark Plasma Sintering [74].

2.4 - PULSED ELECTRIC CURRENT SINTERING

2.4.1 - Introduction

Sintering of materials by ohmic resistance dates to 30's. Taylor used hot pressing to processing cemented carbides [75]. Likewise, a method based

on electric discharge was patented in 40's. It was applied to aid the sintering of powders and the sinter-joining of metals [76]. Subsequently, so called "spark sintering" was proposed by Lenel in the 50's [77].

Commercial units developed over the past few decades include "plasma-assisted sintering" (PAS) [78], "pulsed electric current sintering" (PECS) [79], "electroconsolidation" also known as electric pulsed assisted consolidation (EPAC) [80], and "spark plasma sintering" (SPS) [81], being the last the most employed name nowadays.

The SPS process is based on the simultaneous application of pulsed DC current and uniaxial compaction pressure. The high pulsed DC current flows through the conductive punches and dies (made of graphite) like in a closed electric circuit. Depending on the magnitude of electric resistance offered by the sample the current may either flow or not throughout the powder particles as well.

2.4.2 - Heating Mechanisms

Tokita *et al* [81] argued that spark discharge and plasma took place between adjacent particles in the case of conductive powders. They proposed that these phenomena could remove the species adsorbed as well as destabilize oxides, which result in improvement of sintering.

Recently, on the other hand, Hulbert *et al* [82] shown the absence of plasma into SPS chamber. Lee *et al* [83] advocated that pulsed electric field contributes to the fast densification, whilst Groza *et al* [84] do not consider plasma, but claimed that surface oxide films are pierced when a certain voltage level is achieved. Anderson *et al* [85] verified that oxides were effectively removed.

Chen *et al* [86] added that the direction of the current had no effect on the thickness of the product layer between Si and Mo. Furthermore, the growth rate of the same product was significantly higher under current than in the absence of current. Song *et al* [87] and Diouf and Molinari [88] shown that overheating can take place on the contact between particles due to Joule heating maximization in reduced area (neck).

The pulsed DC electric current (via Joule heating) then seems to be the central element of the heating mechanism. Such effectiveness might be correlated to the enhancement of vacancies concentration.

2.4.3 - Processing and Manufacturing

Due to the high heating rate and peculiar heating mechanisms a gradient in the temperature can be generated either in relation to the sample itself (external to inner part) or in relation to the difference between sample and dies.

Modeling of the current flux can give an indication how it is distributed and in consequence how the temperature is scattered as well. Anselmi-Tamburini *et al* [89] used copper powder and alumina (Al_2O_3) powder to have an insight about these extents. Fig. 2.8 shows the modeling of current distribution in a SPS process for those both materials above mentioned.

They noted that the difference between thermocouple and pyrometer accounted to about 150 °C at 1350 °C. Using a sample 20 mm in diameter and 3 mm thick a radial gradient temperature of only 5 °C was detected for copper. Eriksson *et al* [90] observed the same magnitude (150 °C) in their studies.

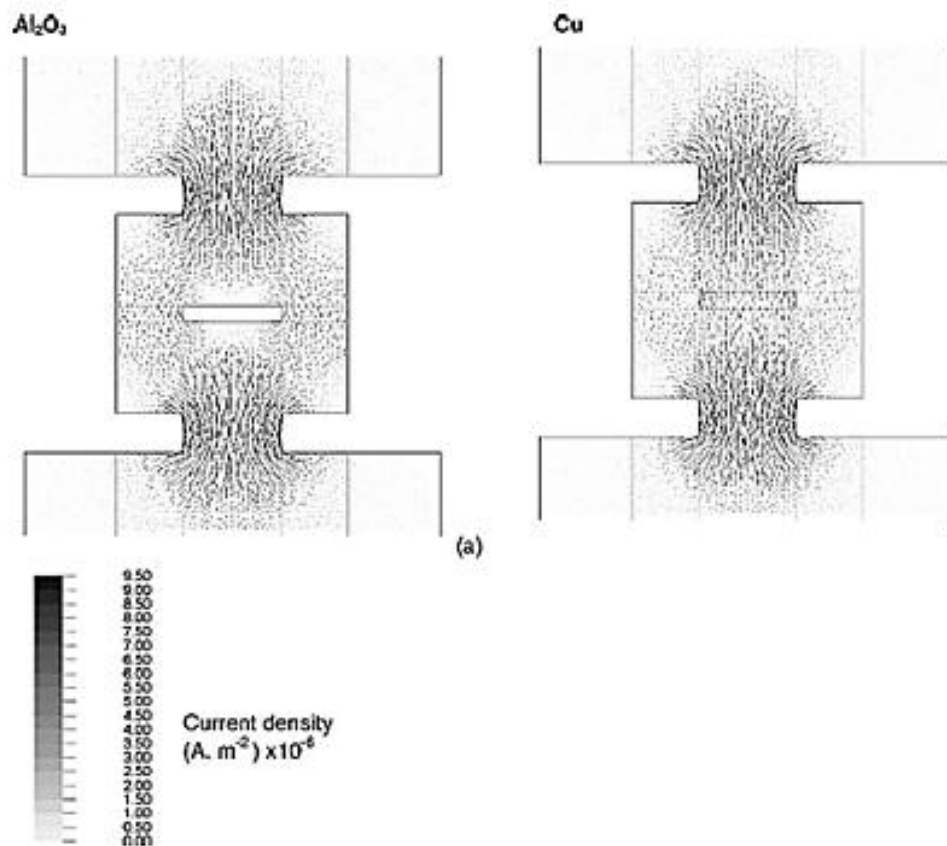


Fig. 2.8 - Current distributions in the SPS die for alumina and copper samples. Applied voltage=5V. [89].

Gradient of temperature on the sample itself and between the sample and the dies may be linked also to the punch and dies design, and to the contact between them, which is plausible since essentially the process is a sort of electric circuit.

A clear example of the punches and dies design is shown by [91]. From the top of the upper punch (also the widest) to the bottom of the lower punch a difference in temperature reach about 500K, using an up to down current orientation.

Chapter 3 - EXPERIMENTAL PROCEDURES

3.1 - SPS Apparatus and Sintering Cycle

Spark Plasma Sintering (SPS) was carried out on a DR. SINTER SPS1050 (Sumitomo Coal & Mining, now SPS Syntex Inc.) apparatus with graphite punches and die. Fig. 3.1 reports an example of the SPS cycle.

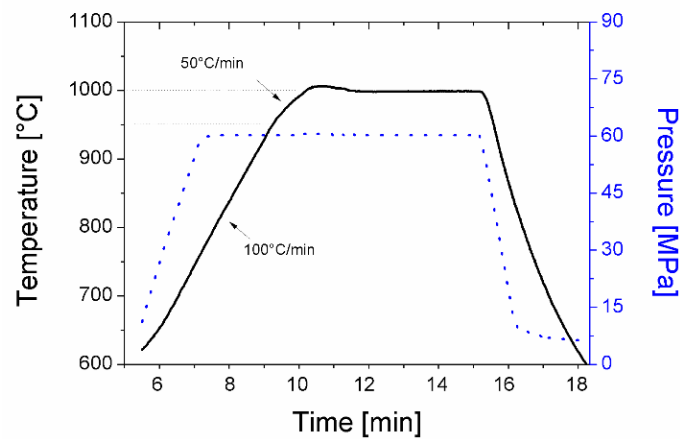


Fig. 3.1 - SPS processing curve. 1000°C / 5 min / 60 MPa

3.2 - Samples Preparation

Co-28Cr-6Mo

Sample preparation for metallographic analysis was carried out by water-grinding with 220, 440, 800 and 1200-grit SiC paper, in sequence, followed by a mechanical polishing using 3 microns diamond abrasive.

Electrolytic etching was carried out with 94 ml distilled water, 4.5 ml HNO₃ and 1.5 ml H₂O₂ solution for 3V and 4sec.

Cp-Ti and Ti-6Al-4V

Samples preparation was carried out by water-grinding with 220, 440, 800 and 1200-grit SiC paper, followed by a mechanical polishing using OPS suspension (colloidal silica suspension) containing 6,5 vol.% H₂O₂ and 1,3 vol.% NH₃. Kroll's reagent (100 ml water, 2 ml hydrofluoric acid, 5 ml nitric acid) was used for metallographic etching.

3.3 - Metallographic Microstructure Investigation

Metallographic characterization was carried out by a LOM microscopy (Leica DC300) and by environmental scanning electron microscopy (ESEM, Philips XL 30) before and after electrolytic etching. Microanalysis was carried out by energy dispersive X-ray spectroscopy (EDXS).

3.4 - Density

Determination of the density was performed by Archimede's method, according to standard ASTM B962-08. The Archimede's density (ρ_s) was calculated by [Equation 1](#).

$$\rho_s = \left(\frac{m}{m-ma} \right) \rho_{water} \quad (1)$$

where m is the mass of the sample, ma is the apparent mass and ρ_{water} is the density of water.

Weight measurements were carried out with a precision balance (AdventurerSL - OHAUS) with a sensibility of 0.0001g.

3.5 - Porosity

The imageJ ® software was employed to evaluate porosity and pores characteristics by image analyses.

Pores Individuation

Micro pores individuation from micrographies was carried out by image analyses using a sequence of steps.

i) Binary: images were converted in a two colors image. Discoloration, spot and tarnish defects are subtracted by gray scale range selection.

The software default takes white color as the selected extent in analyses, there the struts becomes black. The correspondence among the original and the resultant binary micrograph is very good, as can be seen in [Fig. 3.2](#).

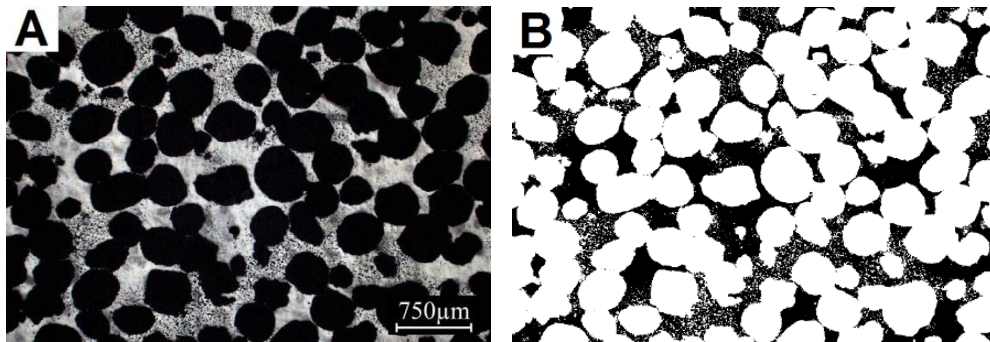


[Fig. 3.2](#) – Section of Scaffold. A) Micrograph; B) Binary image.

ii) Invert: As the aim of analyses is the porosity, the invert process was applied. A simple coupled conversion was carried out. At this point the total amount of porosity, micro and macro-pores can be individuated for subsequent quantification. The result on inversion is shown in [Fig. 3.3](#).

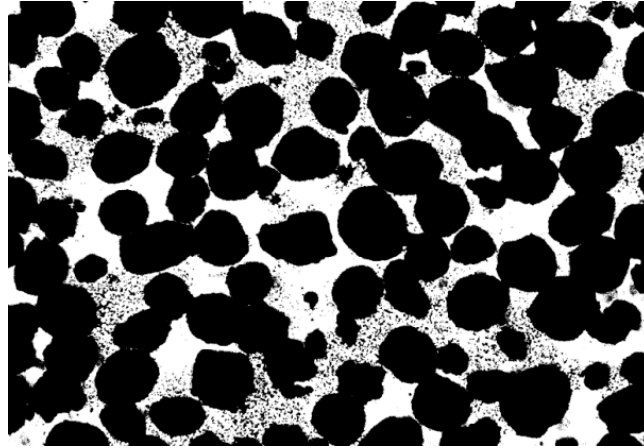


Fig. 3.3 - Scaffold inverted binary image

iii) Analyze Particles: In order to individuate the micropores, those with diameter between 0 and 50 μm were considered. The mask result can be seen in Fig. 3.4.

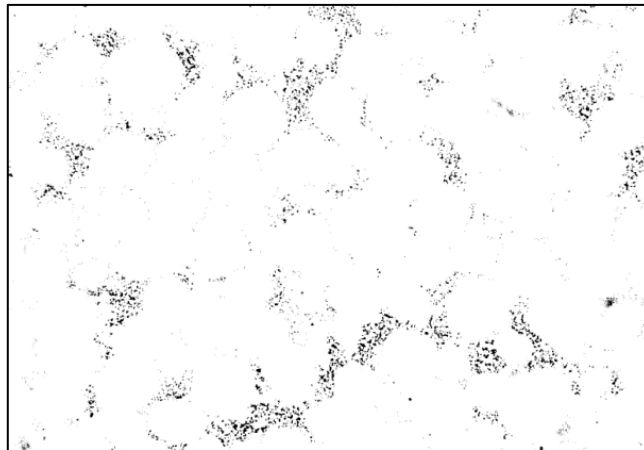


Fig. 3.4 - Selected pores with diameter between 0 and 50 μm .

The Fig. 3.5 shows the result of pores with diameter above 51 μm .

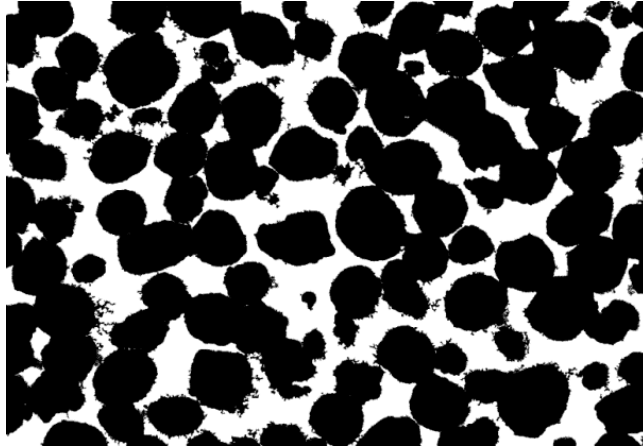


Fig. 3.5 - Selected pores with diameter above 51 μm .

There are some micropores in contact to the macropores which cannot be distinguished. To overcome this weakness Erode and Dilate tools were employed.

iv) Erode + Dilate: In a binary system it is possible to increase one of the two colors using contrast. For example, using Erode black is minimized. With this logics the pores are minimized and in contrast the strut (white) is maximized. The contrary effect can be obtained by using Dilate. For this study where micro- and macro-pores are very dissimilar in size, these combined tools work very well together. The result is shown in Fig. 3.6. It presents exactly the same macropores diameter, but with the absence of micro pores.

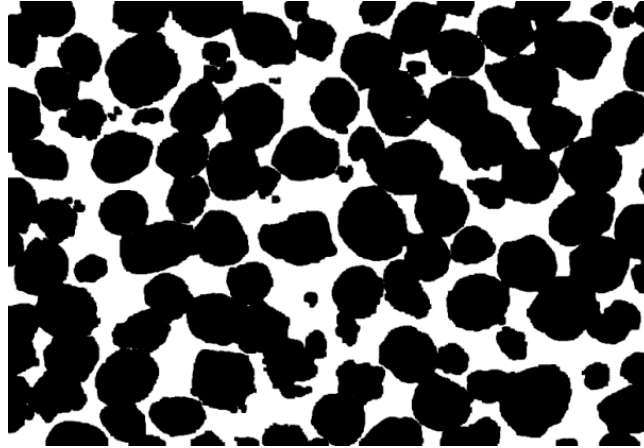


Fig. 3.6 - Only pores with diameter above 51 μm .

Fig. 3.7 shows is the mathematical sum of Fig. 3.4 and Fig. 3.6, a reconstruction of comparable starting binary image.

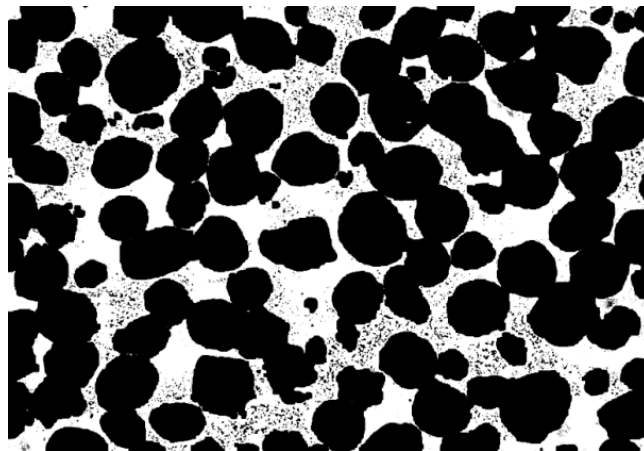


Fig. 3.7 - Whole spectra of individuated pores after image adjustment.

3.6 - X-Ray Diffraction

X-Ray Diffractometry (XRD) was used to investigate the cobalt matrix constitution (f.c.c./h.c.p. phases) and the type and amount of carbides. The

diffraction patterns were collected using a Cu-K α source and the experimental data were elaborated with the Rietveld method using the MAUD software (“Materials Analysis Using Diffraction”) [92,93].

3.7 - Hardness and Microhardness

The microhardness was measured by the Vickers methods, according to ASTM384, with a MHT-4 machine (Anton Paar), on etched metallographic specimens, with a load of 0.5N (HV0.05). The hardness was measured by the Vickers method, according to ASTM 18, with an Emco test machine, on unetched metallographic specimens, with a load of 300N (HV30).

3.8 - Adhesion Test

Static tensile test was carried out with an Universal Test Machine - Tabletop - 10 kN (2,250 lb) | 311 Series. A polymeric adhesive with a minimum tensile strength of 24.1 MPa was used to glue the specimens. Specimens were 25,4 mm in diameter. Procedures followed the ASTM F1147-03

3.9 - Static Shear Test

Static tensile test was carried out with an Universal Test Machine - Tabletop - 10 kN (2,250 lb) | 311 Series. A polymeric adhesive with a minimum tensile strength of 24.1 MPa was used to glue the specimens. Specimens were 20 mm in diameter. Procedures followed the ASTM F1044.

3.10 - Fatigue Shear Test

Samples underwent fatigue test at frequency of 30 Hz, ratio 0,1, applied stress 1-10 MPa, in air. Run out test was assumed at 10^7 cycles. Procedures followed the ASTM F1160.

3.11 - Abrasion Test

The Taber Abraser was loaded with an H-22 wheel, use a total load of 250 g-f and each sample should be run for 100 cycles. Procedures followed the ASTM F1978-00.

3.12 - Tensile Tests

Tensile tests were carried out in an Instron 8516 SH 100 kN machine, at a strain rate of 0.1 s⁻¹ and measuring strain with an axial extensometer with a gauge length of 12.5 mm. The morphology of the fracture surfaces was examined by ESEM. Test bars were in agreement to ASTM E 8M-03.

3.13 - Reverse Bending Fatigue Test

Tests were carried out at room temperature, in air, at zero mean stress, $R=-1$, at nominal frequency of 30 Hz. It was assumed 2×10^6 cycles (standard MPIF 56 as run out test. The staircase step was fixed at 15 MPa. It was adopted a reduction of 5% of applied stress as failure criterion.

The fatigue limit corresponding to 50% of failure probability was obtained by a staircase procedure. P_{90} and P_{10} denote the 90% and 10% levels of failure probability, respectively.

Unnotched specimens, shown in [Fig. 3.8](#), were machined from sintered blanks.

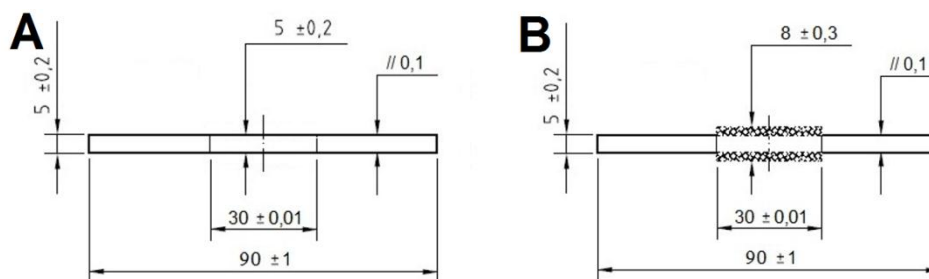


Fig. 3.8 - Fatigue specimens. A) Unnotched test specimen without porous coating; B) Unnotched test specimen with porous coating.

3.14 - Open Circuit Potential Test

The electrochemical tests were performed using a Princeton Applied Research Potentiostat 273A. A classical three electrodes arrangement was used. A Ag/AgCl/KCl(3.5M) reference electrode (+0.207 V vs SHE) and a platinum ring counter electrode were used while the working electrode was the bare substrate. The immersed areas were about 1.4 cm².

The measurements were carried out in a thermostatically controlled cell at 37°C. For the open circuit potential monitoring the electrolyte was 0,9% NaCl under either air or nitrogen purge.

The open circuit potential was recorded for 72 hours both under air and nitrogen purge. The inert nitrogen gas was continuously flushed during the test in order to remove oxygen from the solution. Procedures followed the ISO 16429.

3.15 - Cyclic Potentiodynamic Polarization Test

The potentiodynamic anodic polarizations were carried out after the stabilization of open circuit potential immersing the sample in the cell under nitrogen purge for 30 minutes before the test start.

The potential range applied was from -0.25 mV vs OCP to 1 V for the Co-28Cr-6Mo and 2 V for Ti-6Al-4V, with a scan rate of 0.1 mV/s. Three measurements were performed for each sample.

Chapter 4 - POROUS STRUCTURE

Porous structures have reduced stiffness, high specific area and an intricate architecture, beneficial features for material-to-bone interaction, which are widely preferable against compact surfaces. Studies dealing with surface functionalization by porous coating, thermal or etching treatments have been proposed. It is noted that cells have superior responses to nano and micro roughened surfaces than to a complete smooth one [94]. Besides, porous structures allow tissue ingrowth regeneration by cell migration and nutrients transportation [95]. The biological performance concerning the material-to-bone communication has a two-scale surface topography interaction. The former on 2 dimensions, where cell adhesion, differentiation and proliferation are concerned. The latter on 3 dimensions, where tissue ingrowth arises. In the case of the rigid tissue regeneration the use of porous structures is evidently rather attractive. They can offer a proper environment for bone ingrowth and subsequent stable interlocking, very important issue in permanent implants.

Such porous structures are called scaffold in tissue engineering and therefore this denomination is adopted along this chapter. There are at least three very important characteristics whose make a scaffold prone to have good biological response. They are:

- Pores size;
- Pores interconnection;
- Mechanical reliability.

These three aspects are considered in this chapter. The first two topics are discussed mainly by using metallographic procedure followed by digital images analyses, since they are strongly related to the scaffold design. Mechanical properties were measured by means of wear, shear and pull off

tests. The effect of the porous structure on the substrate fatigue properties is, on the other hand, presented in the chapter 6, where co-sintering subject is developed. Results presented here are always concerning the investigation of the scaffold produced by co-sintering at specific temperature, that is, the same route projected for the final component manufacturing.

This chapter is ordered formerly on the description of scaffold preparation (4.1), followed by morphological aspects (4.2), porosity quantification (4.3), some mechanical properties (4.4) and a summary of results (4.5).

4.1 - Scaffold Preparation

In order to obtain a controlled porosity the space holder technique was employed. It consists of at least two powders mixing, one for building the actual framework (strut) and another for acting as filler that will be chemically extracted after sintering (in our case). Usually, space holder particles are extracted after shaping and before sintering, since the majority of applied space holder materials are organic and consequently decompose at relative low temperature. In the present study the space holder cannot be extracted after shaping, since the two steps of the process (shaping and sintering) occur simultaneously. Poly-methyl-methacrylate (PMMA), ammonium bicarbonate (NH_4HCO_3), carbamide ($\text{CH}_4\text{N}_2\text{O}$), and NaCl are the common space holder materials. In this study the application of PMMA could lead to carbon contamination by thermal decomposition. NH_4HCO_3 is water soluble, but in the presence of oxygen it shows a fair temperature resistance (decomposes at about 50 °C). Moreover, the decomposition product is very dangerous (ammonia). Carbamide resists to about 150 °C and has larger solubility in water compared to the previous ones, but anyway it could contaminate the Ti alloy by carbon. The last is the safest among the others, but has improper

mechanical resistance, with particular brittle behavior. Metallic and ceramic materials have high thermal resistance. Magnesium for instance, does not add carbon, but needs for rather high extraction temperature and slow heating rate. At high temperature and long time either diffusion or reactions leading to compounds formation can take place. In the case of space holder made of steel the extraction is made by electrolytic reaction in acid aqueous solution fully saturated with NaCl. Again, thermal diffusion or reactions could take place during SPS. Hydroxyapatite has also been used by [96] with poor product of interaction. In the present study a similar material was chosen, here called as calcium phosphate (CP).

It consists of a ceramic material with renowned safe behavior into the human body, and valuable features are mechanical strength and temperature resistance, both mandatory to withstand the compaction pressure of 60 MPa at high temperature (around 1000 °C). Moreover, its rounded geometric aspect is beneficial for particles packing. As the scaffold does not play a mechanical role, considering the implant overview, it was shaped as a layer (like a coating) placed on a fully dense substrate. The layer and the substrate were 1,5 mm and 5 mm thick (z axis), respectively, totalizing a 6,5 mm thick assembly. The area were was about 4 x 4 mm² (x-y axes). The blend containing the cp-Ti2 powder and the CP particles in the ratio 30/70 vol.% was prepared in a Turbula mixer for 1 hour. Neither lubricant nor binder was utilized. The blend was then pre-sintered, to avoid space holder particles segregation during die feeding. Segregation can indeed take place due to very different particle size. [Table 4.1](#) reports the cp-Ti2 and space holder particle size range.

[Table 4.1.](#) Cp-Ti2 and CP particles size range.

Materials	Particle Size [µm]
Cp-Ti2	< 45
Space Holder	400-600

The procedure followed for the production of the porous coated specimen is made of the following steps:

- i) Blend pre-sintering at 600 °C and 20 MPa without any holding time;
- ii) Pre-sintered body placed into a proper cut-down punch (inferior);
- iii) Powder feeding (Co or Ti) to fill-up a post sintering height of 5 mm;
- iv) Cut-down punch (superior) positioning with subsequent die closing;
- v) Sintering in SPS apparatus.

Co-sintering of the blend/Co alloy was carried out at 900 °C, at which temperature the Co alloy shows the highest hardness without significant ductility loss, as shown in Chapter 6. Co-sintering of the blend/Ti alloy was carried out at 950 °C, at which temperature the Ti alloy is into the alpha + beta field. Sintering in beta field could result in grain growth and in a microstructure containing alpha lamellae colony plus primary grain boundary alpha, both features leading to low high cycle fatigue resistance. These microstructural features are not accepted by biomedical standard ISO 20160. Fully dense substrates and co-sintering results are further discussed in chapter 5 and chapter 6, respectively.

4.2 - Morphological Aspects

An example of the CP particles distribution on the x-y coordinate (4 x 4 mm²) is shown in [Fig. 4.1](#). The stereoscopic low magnification image displays the metallic strut as black, while the CP particles are gray. Particles are homogeneously distributed, being this feature associated to the effectiveness of pre-sintering before die feeding. In some regions they do not touch each other, leading to build up a strut as thick as 500 µm.

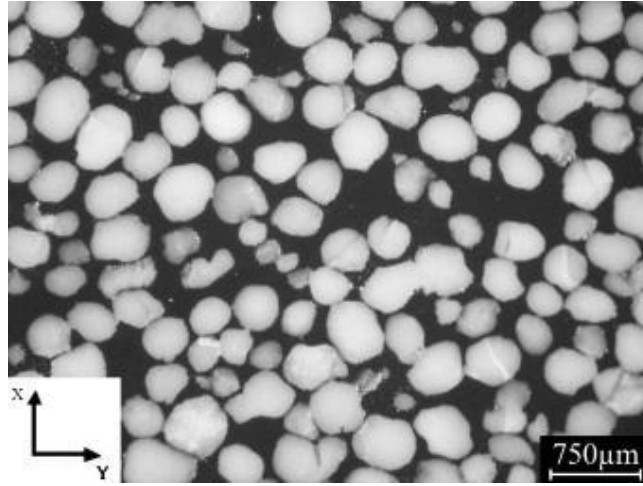


Fig. 4.1. Sintered blend containing the metallic strut and CP particles.

The first requirement for pore interconnection is related to the space holder extraction. As this step is carried out by chemical dissolution in liquid medium, good pore interconnection is necessary in order to reach particles far from external surface. An example of the particles distribution on the z axis is shown in Fig 4.1.

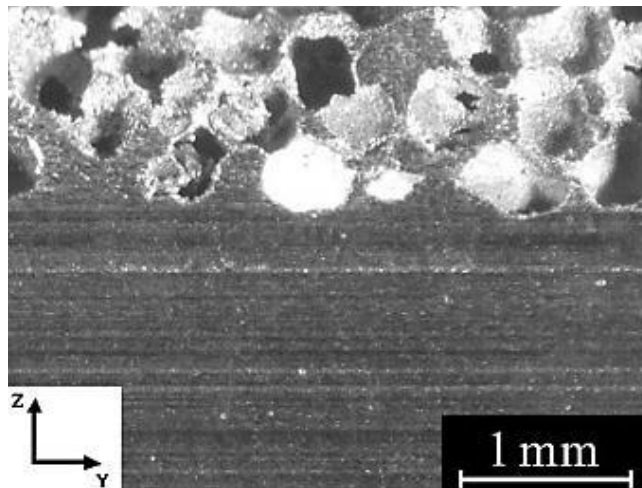


Fig. 4.2. Sintered porous/substrate cross section (z axis).

Despite the thin layer, the interconnection is actually not perfectly continuous across the z axis. The region nearby the punch (top) tends to show larger interconnection gaps since hard particles interact each other. On the other hand, the region nearby the substrate (bottom) suffers the effect of the plastic deformation of the softer metallic powder, accommodating particles and therefore offering reduced mechanical support to the greatest hard particles packing. An evidence of this behavior is observed in Fig 4.2, where a CP particle is found close to the substrate. Such CP particle could be extracted as the superficial ones, but long times would be required. As mentioned before, the calcium phosphate does not have any hazardous effect on human body and therefore the extraction time was limited to 8 hours.

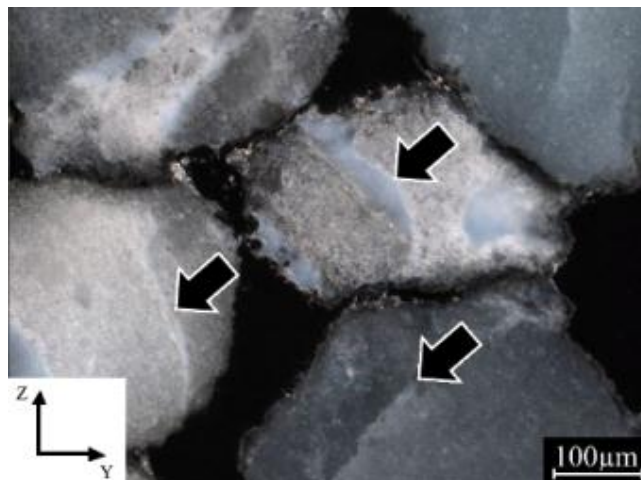


Fig. 4.3. Cracks identified in CP particles.

Cracks in the CP particles can be observed in the in Fig. 4.3. They are caused by the effect of the compaction pressure on the contact point between adjacent hard particles. Even so, a mechanical collapsing was not

verified even at 60 MPa. These cracks actually contribute for particles accommodation and packing improvement.

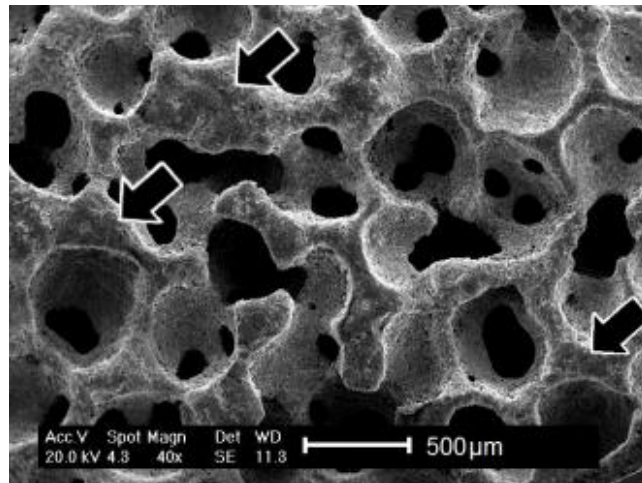


Fig. 4.4. The scaffold obtained after space holder extraction. Arrows indicating zones in contact with the graphite die.

The final structure of the scaffold is shown in Fig. 4.4. It is formed by two types of pores. Macropores are essentially the cavities left by space holder extraction and show a rounded geometric shape. They are randomly distributed with size corresponding to that of the largest space holder particle. The interconnection gaps are generally larger than 100 microns. This dimension has been pointed out by some authors as the smallest magnitude for nutrients transportation and later bone firm fixation [97].

Flat regions signed by arrows are formed by the contact of the cp-Ti powder with the graphite punch. As carbon finds high solubility in titanium some diffusion takes place. Such superficial contamination is limited to a few microns due to the short sintering time. It can be removed from the surface by low pressure blasting process, which also open some residual surface closed pores.

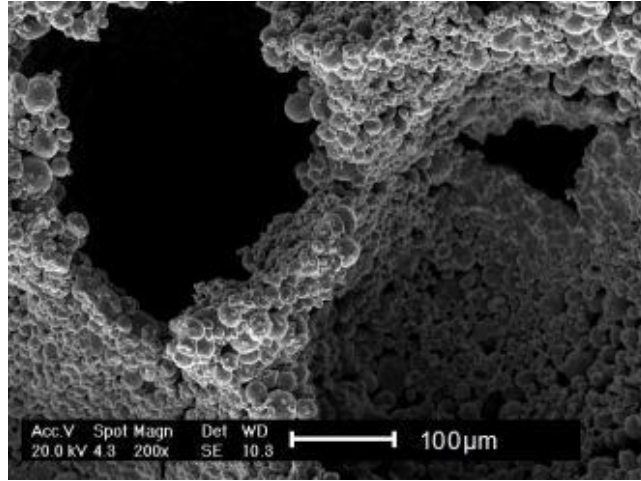


Fig. 4.5. Metallic strut after cryogenic fracture.

The metallic strut consists in cp-Ti powder particles partially densified, as can be seen Fig. 4.5, after cryogenic fracture. It is evident a micro-scale roughness due to the preservation of the powder particles shape. Interparticle necks did not grow very much. For neck enhancement, sintering temperature or sintered time could be increased, but in contrast the micro-scale roughness would be diminished. As shown by Chen *et al* [98], a positive biological behavior may outcomes from this micro-scale roughness. Bone cells (osteoblast-like) are prone to adhere onto the necks since they have high superficial energy due to stress concentration caused by the curvature. Subsequently, new cells will develop a sort of bridging over the primary cells, resulting in proliferation rate improvement.

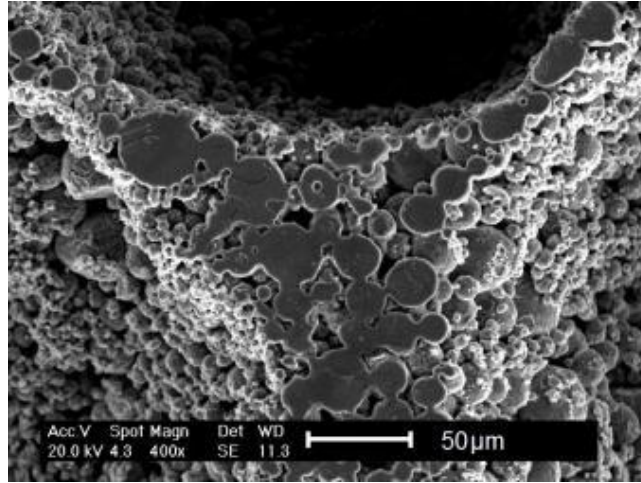


Fig. 4.6. Strut metallographic section

When struts are observed in section the micro-scale roughness become a micro porosity, as can be seen in Fig. 4.6.

An example of the polished scaffold metallographic section (x-y plane) is shown in Fig. 4.7. Pores are black and struts are white. As shown before, micro pores were found out in struts, but some regions also appeared pores free. It can be concluded that in some areas the compaction loading is more effective, leading to a higher densification.

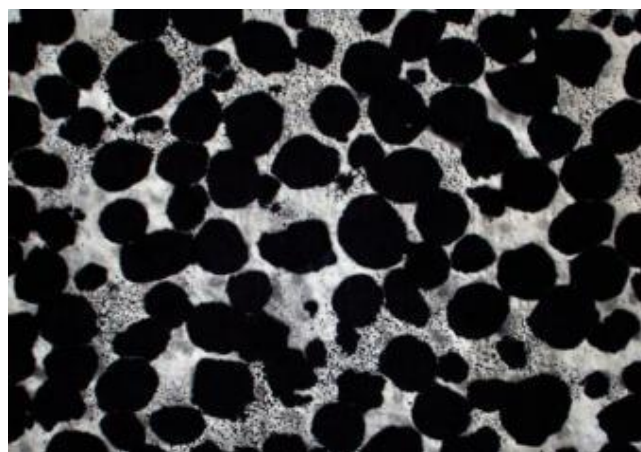


Fig. 4.7. Scaffold light optical micrograph

4.2 - Porosity Characterization

The porosity quantification was carried out by means of area fraction analyses (ImageJ ®). The total amount of porosity, micro and macro porosity as well as pores size and distribution were estimated.

All of these features are discussed on the basis of twenty images, but for the sake of simplicity only some selected images are shown here. The total amount of porosity was calculated from images similar to that shown in Fig. 4.7, as binary image. An amount of $71,55 \pm 4,01\%$ of total porosity was counted. This quantity is in accordance with the volumetric amount of space holder added to the blend. As the space holder particles were kept up final sintering no shrinkage occurred. Additionally, the micro and macro porosity were quantified individually: they result 1,73% and 69,67%, respectively. The sum of these quantities is 0,15% less than the total porosity. On micro porosity a satisfactory error of about 10% was achieved. On the other hand, taking into account the total porosity this error diminishes drastically to less than 0,2%.

Micropores distribution is shown in Fig. 4.8. It considers isolated pores only, since those connected to macropores are not recognized by Image Analysis as single pores. The frequency of pores size is concentrated on very small diameter and 15 μm seems to be the typical larger pores size.

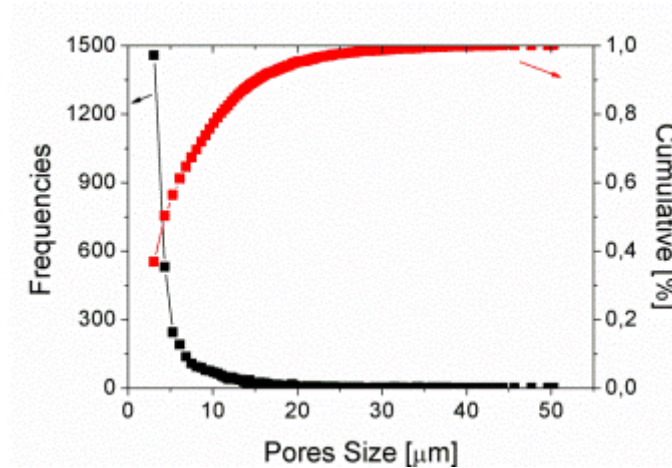


Fig. 4.8. Micro pores distribution

The three cumulative diameters used to describe the pore size distribution are reported in Table 4.2.

Table 4.2. Pore size distribution

Cumulative Diameter	Average size [μm]
d10	<3,15
d50	4,32
d90	15,43

Approximately 50% of the measured pores are concentrated below 5 μm thanks to the effect of compaction pressure and broad cp-Ti particles size distribution.

4.3 - Interfacial Interactions

An interfacial interaction between space holder particles and the metallic strut is expected due to high processing temperature. Fig. 4.10 shows the

product of interaction on the surface of a particle, whilst Fig. 4.10B shows a cross section view.

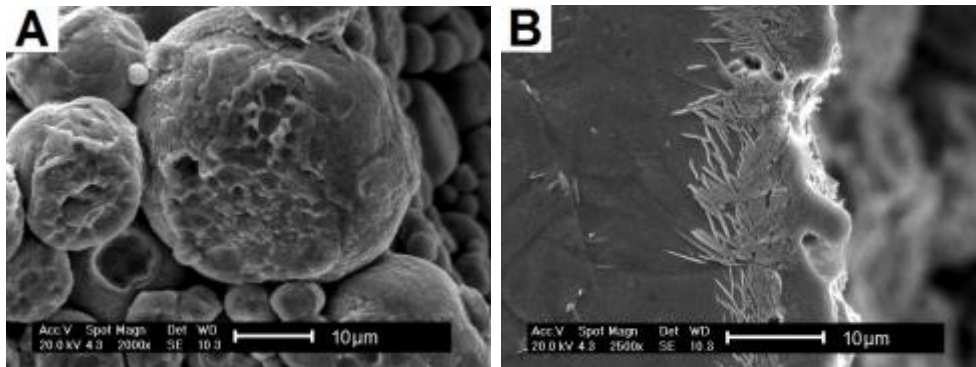


Fig. 4.10 - Products of interaction between Ti strut and calcium phosphate.

The compound shows a needle-like aspect. Interaction involves a layer of 20 µm maximum thickness. This thickness is only a few microns in contact with poor densified zones. Table 4.3 reports the chemical composition detected by EDX analyses.

Table 4.3 - Chemical composition of interaction products

Element	wt%
P	2,55
Ca	7,24
Ti	90,21

Several compounds can be formed from Ti-P reaction, mainly Ti_4P_3 and Ti_5P_3 are reported [99]. They are formed from diffusion of P ions into the titanium matrix, favored by a reducing sintering atmosphere. On the other hand, $CaTiO_3$ was also detected in HA coated metals [100].

4.4 - Mechanical Properties

This section addresses the mechanical properties of the scaffold in two subsections: the strength of the joint between the scaffold and the fully dense substrate (pull-off and shear tests) and the wear resistance.

4.4.1 - Adhesion Test

The scaffold offers a structure for bone ingrowth and interlocking. Its adhesion on the substrate has therefore to be ensured. Adhesion test (named pull-off test) following the ASTM F1141 was carried out. Fig. 4.11 shows a representative stress-displacement curve of the test.

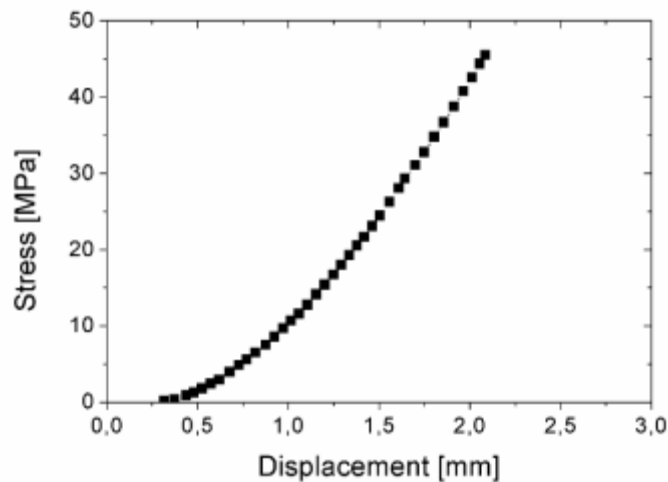


Fig. 4.11 - A representative stress-displacement curve of pull-off test.

It was observed that failure occurred the porous structure, and not at the interface. The average strength is 39,80 MPa with a standard deviation of 3,91 MPa, much higher than 22 MPa required by the ASTM standard.

4.4.2 - Static Shear Test

Interfacial shear stress is another type of mechanical loading to which the scaffold is subjected, mostly in the case of cementless implants. The scaffold has to withstand at least 20 MPa in static shear test. Fig. 4.12 shows a representative stress-displacement curve of the test.

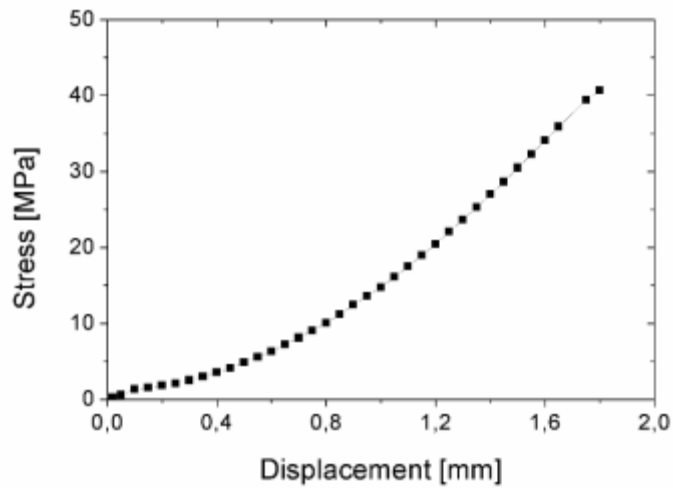


Fig. 4.12 - A representative stress-displacement curve of shear test.

Again, it was observed that the failure occurred on the porous structure. In this case, the average strength is 35,74 MPa with a standard deviation of 1,69 MPa, much higher than 20 MPa required by the ASTM F1044 standard.

4.4.3 - Fatigue Shear Test

The scaffold is subjected to cyclic shear loading. The samples and the test configuration are shown in Fig. 4.13.

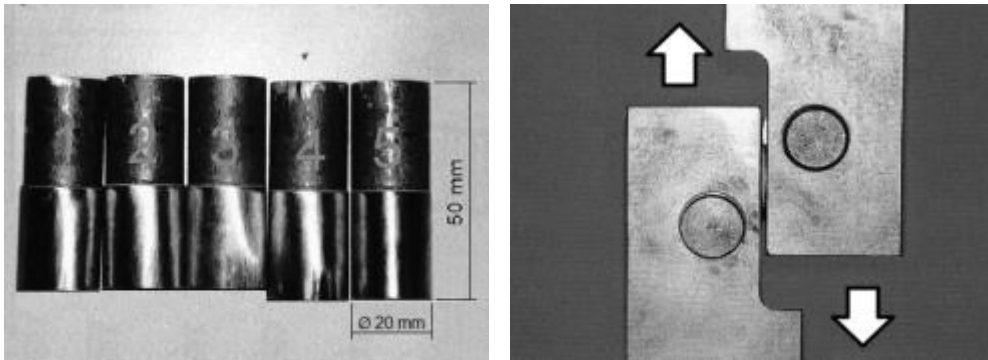


Fig. 4.13 - Fatigue shear test samples and test configuration.

Failure after 10 million cycles were not detected. The five specimens have all succeeded.

4.4.4 - Taber Abrasion Test

Taber test was carried out in order to evaluate the scaffold weight loss when subjected to wear. Fig. 4.14 shows the weight loss versus the number of cycles.

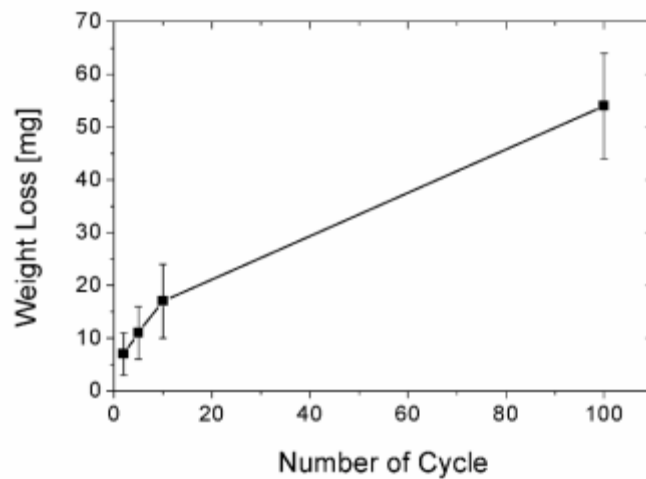


Fig. 4.14 - Weight loss versus number of cycles in taber abrasion test.

The weight loss rate decreases during the test likely because of the stabilization of the contact area and, consequently, of the contact stress. The material fully attained the ASTM F1978 standard, which requires a weight loss lower than 65 mg after 100 cycles.

4.5 - Summary of the Results

- The porous structure was produced by the space holder method, using a Calcium Phosphate as space holder material, which is resistant to the SPS temperature.
- The total volume of pores is very close to the volume of space holder (70%), meaning that shrinkage did not occur thanks to the stability of the space holder material.
- Same cracks were observed in the calcium phosphate particles. In any case, an overall porous structure integrity was ensured (no collapsing was verified).
- The porous structure is formed by two types of pores: macropores (interconnected macro porosity) and micropores, located on the struts. Micro pores (isolate pores on the struts) accounted to about 2% of total porosity; Macro pores are homogeneously distributed on the compaction plane and less homogeneously distributed on vertical plane, since a gradient of particles arrangement takes place during compaction.
- Macro pores are well interconnected.
- Struts are formed by partially sintered powder particles, which results in a micro scaled roughness.
- Some struts are pores-free, meaning that compaction pressure is not equally effective in all regions.

- Macropores size is in the range 400-600 μm , whilst micropores are mainly smaller than 15 μm .
- Interaction between the space holder and cp-Ti produces compound(s) with needle-like aspect, containing both calcium and phosphorus;
- Adhesion strength of the porous structure on the substrate is almost twice than that required by ASTM F1147 standard; fracture occurred on strut.
- Shear strength of the porous structure on the substrate is almost twice than that required by ASTM F1044 standard; fracture occurred on strut.
- All five specimens succeed the fatigue shear test following ASTM F1160.
- The weight loss during taber abrasion tests was low enough to satisfy the ASTM F1978 requirements.

Chapter 5 - FULL DENSITY SUBSTRATES

Full density materials are mandatory when wear and fatigue properties are concerned [101]. Insufficient fatigue resistance results in crack formation, propagation and subsequent failure [102], while insufficient wear resistance promotes ions release into the body [103].

This chapter describes the development of the Co-28Cr-6Mo alloy by presenting the effect of the sintering temperature, compaction pressure and powders. The impact of these variables was evaluated on the basis of density-microstructure-hardness interdependence.

Mechanical and corrosion properties are presented for both Co-28Cr-6Mo and Ti-6Al-4V. Cast and wrought materials were also characterized for sake of comparison.

5.1 Co-28Cr-6Mo

5.1.1 - Powder Microstructure

The gas atomized Co-28Cr-6Mo powder observed at SEM is shown in [Fig. 5.1](#).

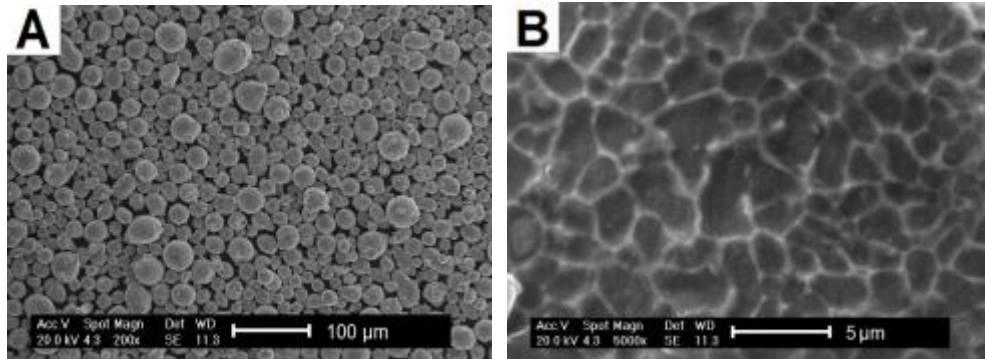


Fig. 5.1. Co-28Cr-6Mo powder. A) Particles; B) Microstructure.

Particles have a spherical shape. The microstructure (Fig. 5.1B) consists of quasi-equiaxed grains on the order of 1 to 5 μm with carbide [104] at grain boundary. Such arrangement is commonly called as cellular structure. The nominal chemical composition and particle size distribution provided by the powder supplier are reported in Table 5.1 and Table 5.2, respectively.

Table 5.1 - Typical chemical composition

Element	Wt [%]
Cr	29,2
Mo	5,6
Si	0,77
Mn	0,74
Fe	0,28
Ni	0,030
C	0,017
O	0,046
Co	BALANCE

Table. 5.2 - Typical particles size distribution

Cumulative [%]	Diameter
d10	22,4 μm
d50	33,9 μm
d90	51,1 μm
< 20 μm	4,4% (Vol.)

5.1.2 - Effect of Sintering Temperature

Samples were sintered at different temperatures, from 800 °C to 1050 °C with 50 °C steps, with 5 minutes isothermal holding and 45 MPa pressure. The SPS densification curve is shown in Fig. 5.2. Densification takes place intensely from 800 °C to 900 °C, when the maximum density is achieved. A further increase in temperature does not cause any densification enhancement. About 8,4% and 1,3% open porosity was found in materials sintered at 800 °C and 850 °C, respectively.

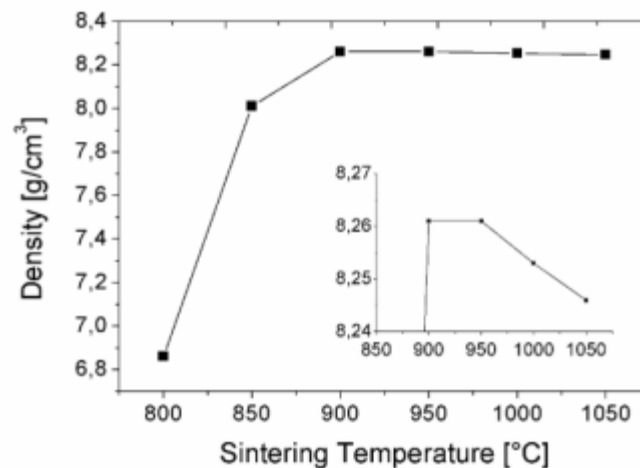


Fig. 5.2 - Co-28Cr-6Mo densification curve at various temperature; 5 min. and 45MPa.

The microstructures of the sintered materials are shown in Fig. 5.3. Pores are easily identified as black spots in the shiny unetched metallic matrix. They are random distributed, reaching 20 µm of size and irregular shaped. The materials sintered above 900 °C (included) show only isolated pores.

Larger pores in Fig. 5.3A and Fig. 5.3B tend to be orthogonal to the compaction direction.

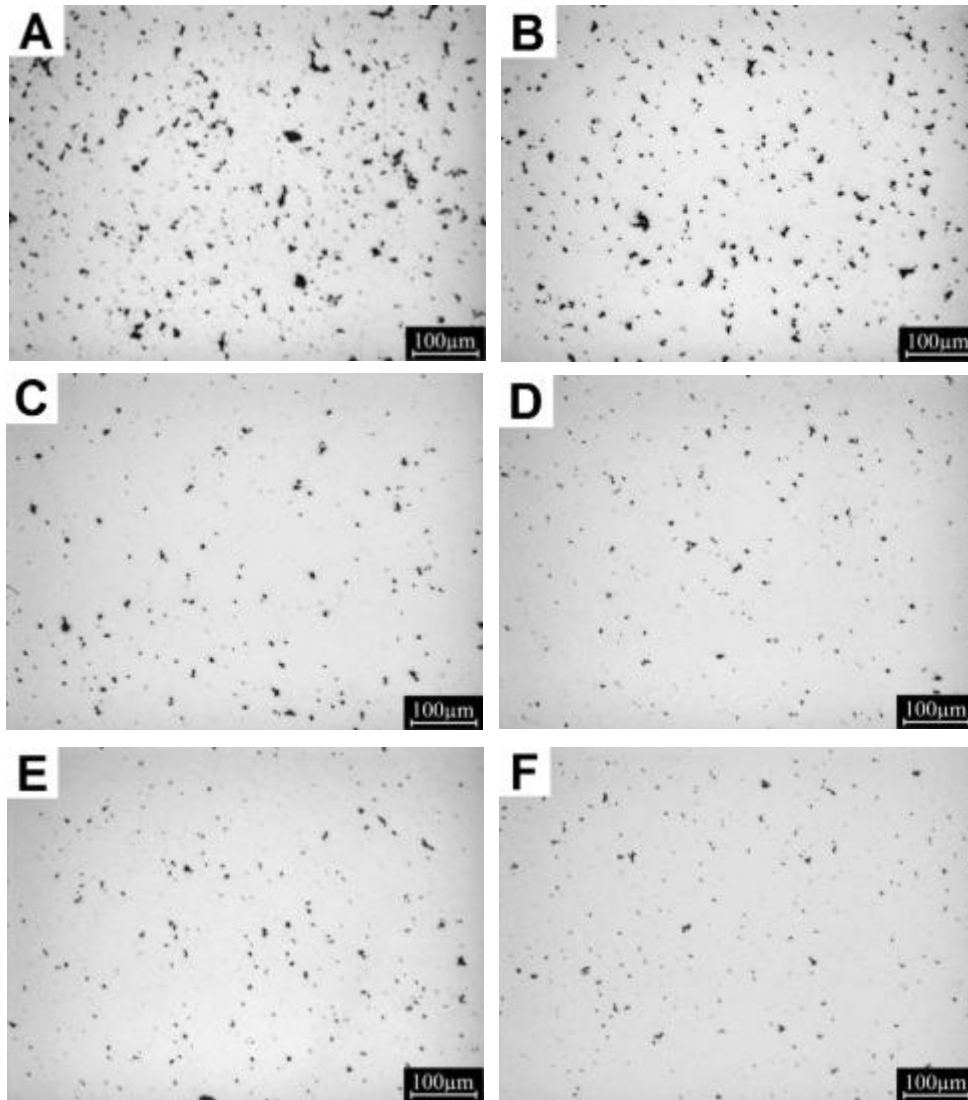


Fig. 5.3 - Unetched Co-28Cr-6Mo microstructures sintered at various temperatures, 5 min and 45 MPa. A) 800 °C, B) 850 °C, C) 900 °C, D) 950 °C, E) 1000 °C and F) 1050 °C

Etched microstructures are shown in Fig. 5.4.

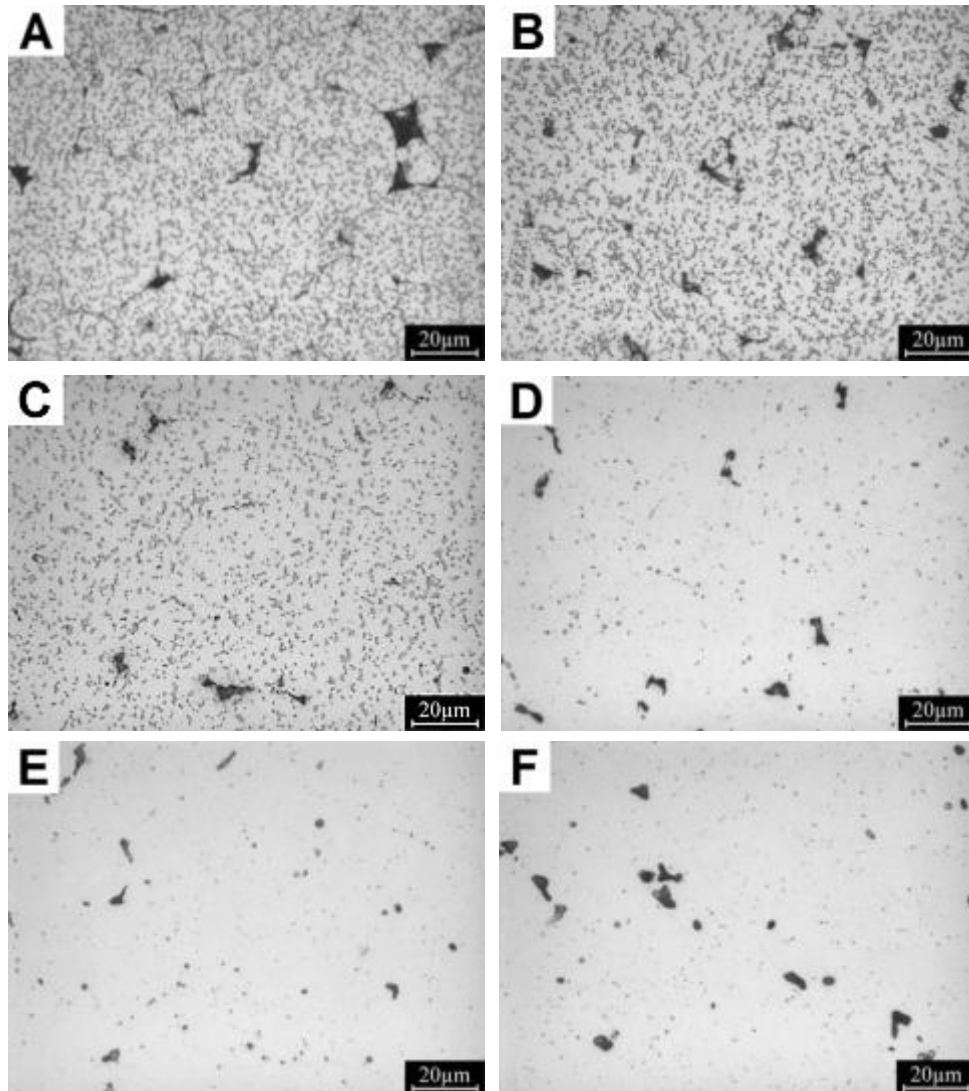


Fig. 5.4 - Etched Co-28Cr-6Mo microstructures sintered at various temperatures, 5 min and 45 MPa. A) 800 °C, B) 850 °C, C) 900 °C, D) 950 °C, E) 1000 °C and F) 1050 °C

In the material sintered at 800 °C pores are systematically located between particles. Precipitates are seen as small gray particles more evident in materials sintered at lower temperatures. Increasing SPS temperature promotes their gradual dissolution. In particular, an intensive dissolution is

observed above 950°C. The γ/ϵ transformation of the Co-28Cr-6Mo alloy occurs at around 1000 °C [105], and γ is stable above this temperature. Since the carbon solubility in γ phase is quite high [106], precipitates are promptly solubilized. The discrepancy between the temperature at which an almost precipitate-free microstructure is observed (950 °C) and the γ/ϵ equilibrium temperature can be attributed to the well-known difference among the actual temperature of the powder into SPS chamber and that measured on the external wall of the die.

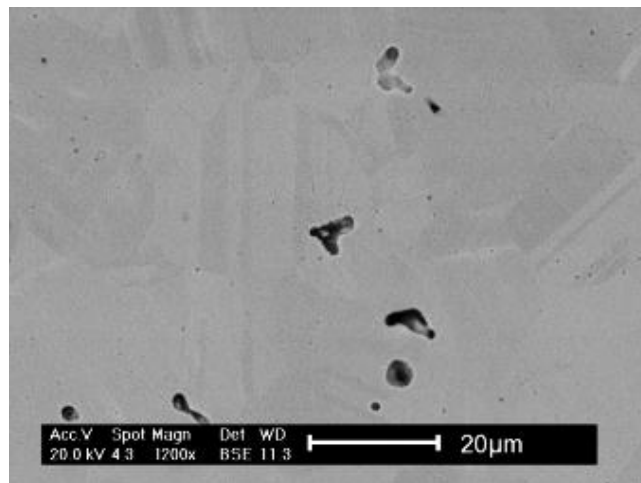


Fig. 5.5 - Co-28Cr-6Mo microstructure sintered at 1050 °C seen at SEM.

Carbides are completely dissolved at 1050 °C. Twins are revealed in this material (Fig. 5.5). They are formed during cooling from γ phase due to its low Stacking Fault Energy [50]. Once precipitate dissolution takes place, grain coarsening occurs. Hardness follows the density curve up to the maximum density (Fig. 5.6).

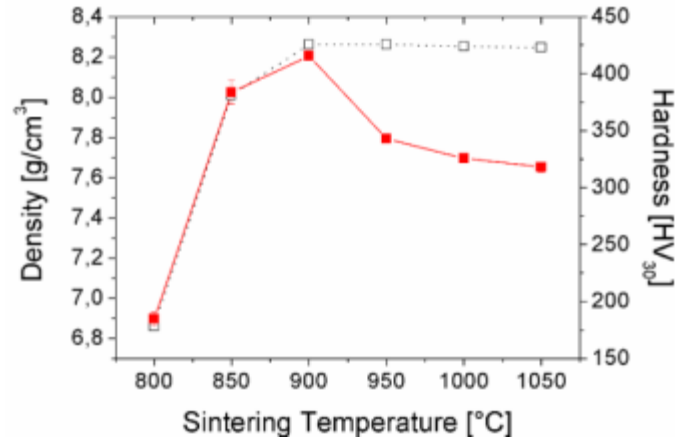


Fig. 5.6 - Hardness and density vs. SPS temperature.

As indentation involves solid and pores during deformation, this behavior was expected. Likewise, hardness significantly decreases at higher temperatures. This behavior finds explanation in the microstructure evolution. Precipitates strengthen the material and their dissolution drives down hardness. This means that the hardening promoted by carbon and alloying elements dissolution in the metallic matrix (solution hardening) combined to the change in the matrix microstructure is less effective than hardening promoted by precipitates (precipitation hardening). Moreover, hardness drops continuously on further increasing temperature, as a result of progressive dissolution of precipitates and grain growth.

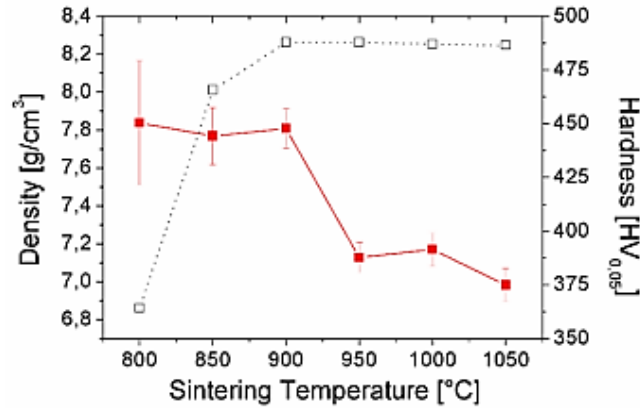


Fig. 5.7 - Microhardness and density vs. SPS temperature.

On the other hand, microhardness does not show an appreciable variation at low temperatures (up to 900 °C) (Fig. 5.7). It means that the amount of precipitates dissolved at that temperature slightly affects hardness. Standard deviation is straight correlated to microstructure, which is not well homogeneous at low temperature, and therefore it is higher at 800 °C and 850 °C. At 950 °C and above, precipitates undergo dissolution, mostly at 1050 °C. Standard deviation in this range of temperature is much more stable due to a better microstructure homogeneity. X-ray diffraction (XRD) completes the structural characterization (Fig. 5.8).

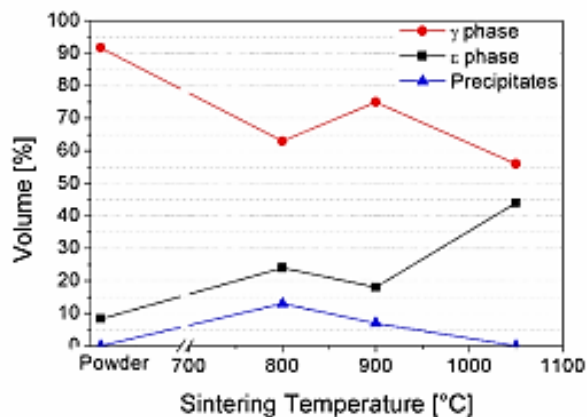


Fig. 5.8 - Microstructural constituents vs. SPS temperature.

Analyses on the powder revealed a massive presence of γ phase (f.c.c.) without any precipitate (metastable solid solution due to the fast undercooling during atomization). Huang and Lopez [107] verified that athermal ϵ martensite (h.c.p.) transformation is inhibited when grain size is less than 10 μm and therefore the structure of the atomized powder is justified by the fine cell size. Sintering at 800 °C promotes the formation of M_7C_3 carbides, as can be seen in the XRD pattern shown in Fig. 5.9, which destabilize austenite favoring the formation of ϵ phase up to 25%.

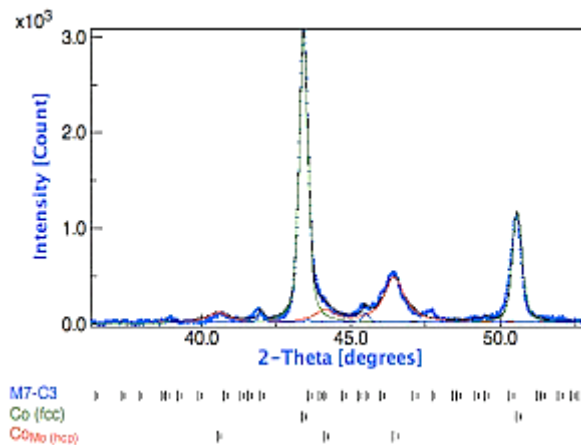


Fig. 5.9 - XRD pattern of Co-28Cr-6Mo sintered at 800°C.

On the other hand, by increasing sintering temperature up to 900 °C carbides dissolution is enhanced, increasing carbon content in cobalt matrix and stabilizing γ phase, which amount slightly increases. Finally, at highest temperature (1050 °C) carbides are completely dissolved, grain size grows and ϵ martensite transformation takes place. The constitution of the metallic matrix is then strongly correlated to SPS temperature and to its effect on the precipitation/solubilization of carbides.

Fig. 5.10 shows microhardness and the volume content of carbides at various temperatures.

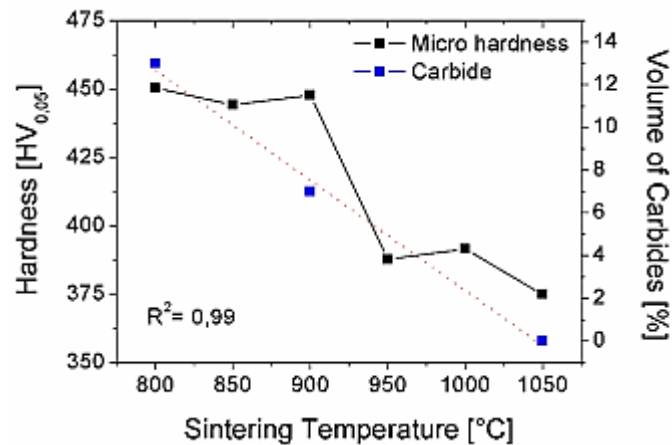


Fig. 5.10 - Hardness and carbide content vs. SPS temperature.

Microhardness shows a sudden transition temperature (900-950 °C), whilst carbides dissolution follows a linear behaviour, indicating the importance of γ and ϵ phases on microhardness.

5.1.2.1 - Relative Density

The actual theoretical density must be calculated from chemical composition. The Co-28Cr-6Mo ASTM F75-07 standards prescribes that chromium can vary from 27 to 30 wt% and molybdenum from 5 to 7 wt%, for instance. The calculation of the theoretical density limits and the theoretical density of the employed powder is shown in Table 5.3. The calculation considers elements as natural isolate species.

Table 5.3 - Theoretical density limits and of the powder.

Elements	Min. [wt%]	Max. [wt%]	Measured [wt%]
Cr	30	27	29,2
Mo	5	7	5,6
Ni		0,5	0,03
Fe	0,75		0,28
C	0,35		0,017
Si	1		0,77
Mn	1		0,74
W		0,2	
P	0,02		
Al	0,1		
Ti	0,1		
B	0,01		
Co	61,67	65,3	63,317
	Theoretical Range		Actual
Density [g/cm ³]	8,29	8,51	8,37

Table 5.4 reports the achieved relative densities at various temperature, for 5 min. and 45MPa.

Table 5.4 - Density and relative density at various temperature.

Sintering Temperature [°C]	Density [g/cm ³]	Relative Density [%]
800	6,86	81,9
850	8,01	95,7
900	8,26	98,7
950	8,26	98,7
1000	8,25	98,6
1050	8,24	98,5

Theoretical density = 8,37 g/cm³

In principle, relative density does not exceed 99%, the lower limit usually accepted to define “full density”. It has to be considered that the method used for calculation of theoretical density does not consider carbides and all the other precipitates. It may be then concluded that, within the uncertainty of the reference datum, SPS at 900-950 °C leads to a sintered density very close to the theoretical one.

5.1.3 - Effect of Pressure

The effect of compaction pressure on the densification during SPS process has been discussed by some authors [88, 108, 109]. Initially, it causes particles rearrangement, followed by elastic and plastic deformation of the contact regions, progressively propagated into the core of the particles [88]. These events are more or less effective depending on the nature and features of the powder. Ceramic powders, whose in essence are brittle, normally do not undergo plastic deformation. Moreover, usually they are non-electrical conductive, characteristic that is correlated to plastic deformation enhancement from thermal softening promoted by localized overheating on the particles contact points (electric current → Joule heating → overheating on necks → thermal softening) [87,88]. Particles rearrangement is therefore even more important in ceramic powders densification, mainly in the case of solid state sintering. Metallic powders, which are conductive and ductile, are expected to be very susceptible to compaction pressure during SPS. Keeping it in mind, compaction pressure was increased in order to improve densification.

Although some authors have used compaction pressures up to 200 MPa [109,111], the upper limit used in this work was 70 MPa. This limit is imposed by the quality of the graphitic dies.

The densification curve at 900 °C and 5 minutes isothermal holding and at two compaction pressures is displayed in Fig. 5.11. Early at 60 MPa density reaches the range of fully dense material (>99%), but it rises up to 99,4% at 70 MPa. It is supposed that density can be further improved, but critical situation regarding die failure was detected at 70 MPa. Therefore, 60 MPa was taken as the reliable compaction pressure in the experimental equipment used in the present study.

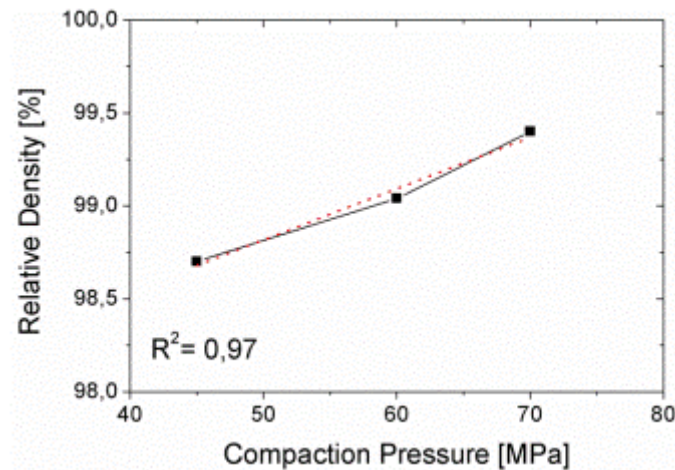


Fig. 5.11 - Relative density vs. compaction pressure; 5 min and 60 MPa.

The microstructures attained at 60 and 70 MPa (900 °C and 5 minutes) are shown in Fig. 5.12. Pores are sensibly reduced at 60 MPa and practically eliminated at 70 MPa. No effects on carbides are observed, as it was expected.

With pores continuously removed from the microstructure on increasing pressure, hardness increases correspondingly, as shown in Fig. 5.13.

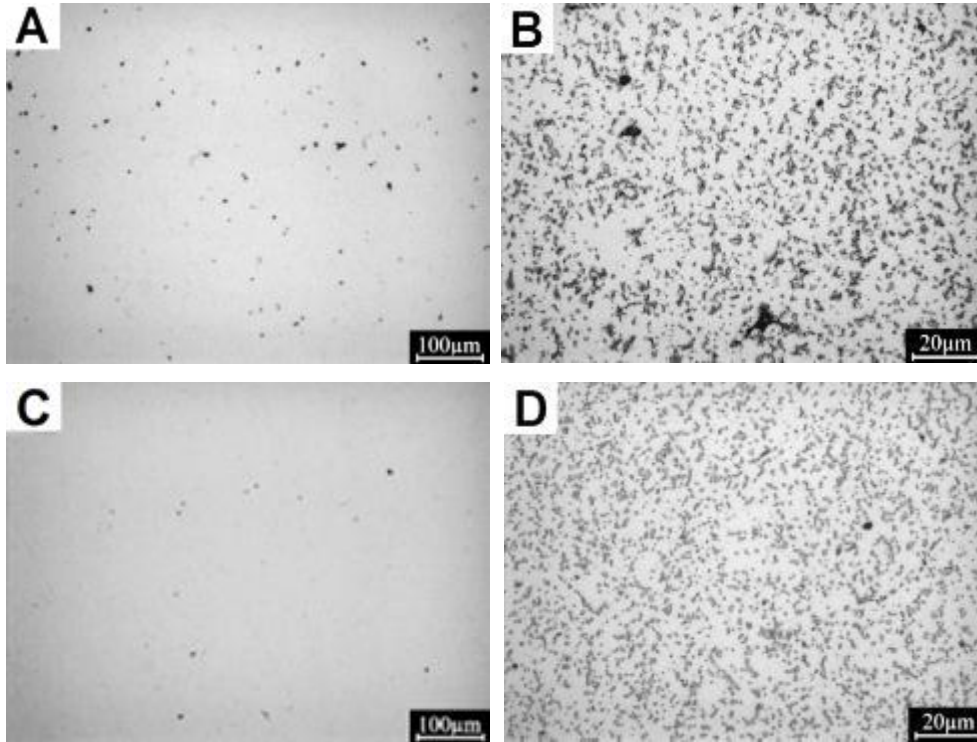


Fig. 5.12 - Co-28Cr-6Mo Microstructures sintered at two pressures, 900 °C and 5 min. A) and B) 60 MPa; C) and D) 70 MPa.

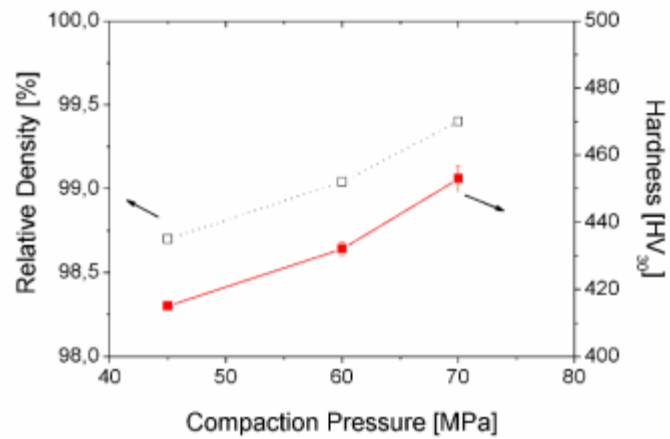


Fig. 5.13 - Hardness and density vs. pressure, 900 °C and 5 minutes.

On the other hand, as carbides do not undergo further dissolution, microhardness does not change significantly, as can be noticed in Fig. 5.14.

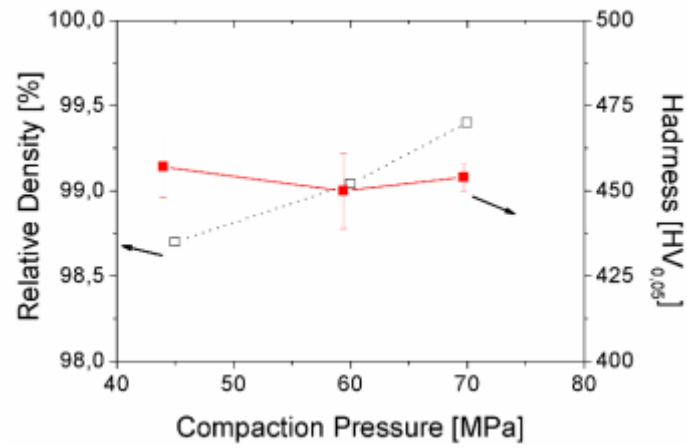


Fig. 5.14 - Microhardness and density vs. pressure, 900 °C and 5 minutes.

Fig. 5.15 shows the virtually pores-free Co-28Cr-6Mo microstructure when sintered at 900 °C, 5 min, 70 MPa.

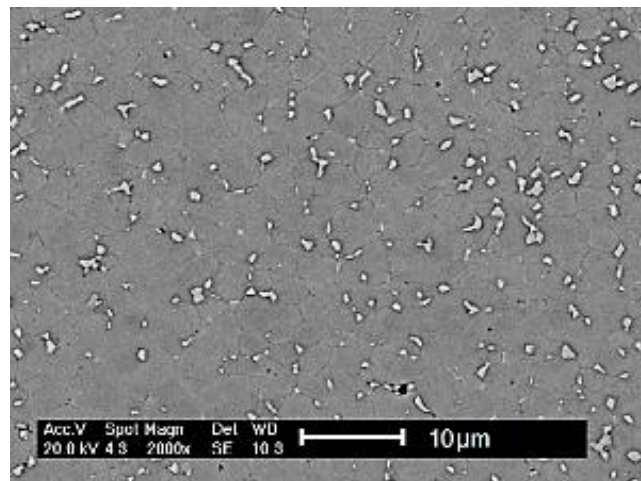


Fig. 5.15 - Co-28Cr-6Mo microstructure sintered at 900 °C, 5 min, 70 MPa.

In conclusion, the best properties interdependence by far is achieved by means of SPS at 900 °C, 5 minutes and 60 MPa.

5.1.4 - Influence of Powder

In view of exploring raw materials, three different Co-28Cr-6Mo powders by different suppliers were investigated. For sake of confidentiality the suppliers cannot be disclosed.

Fig. 5.16 displays the frequency and cumulative curves of particle size.

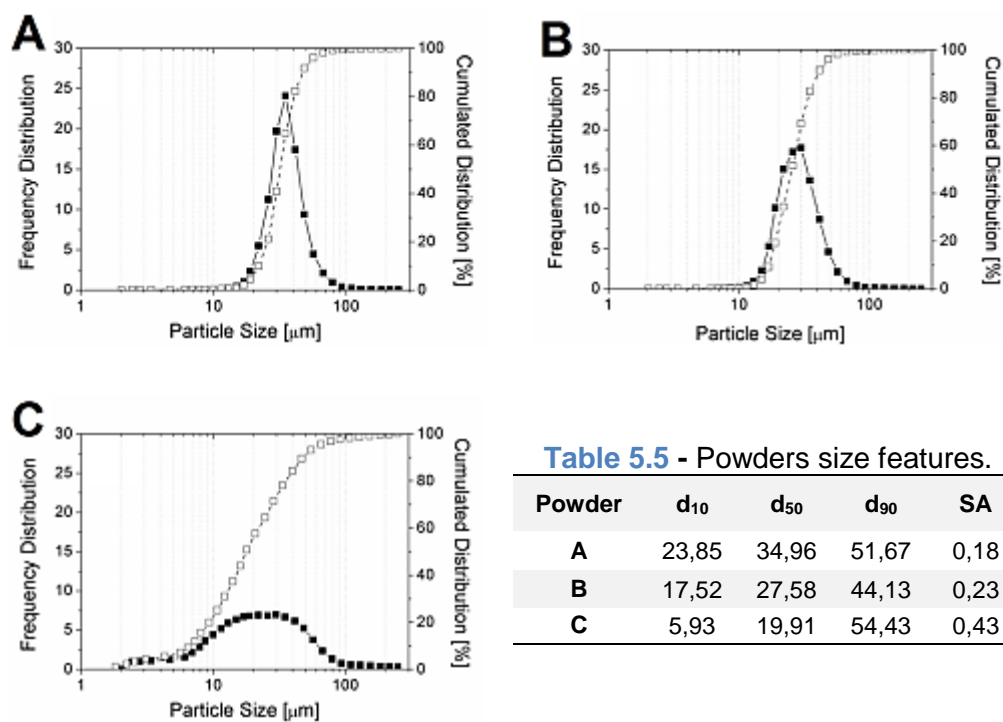


Fig. 5.16 - Powder particle size frequency and cumulative curves. A) Powder A; B) Powder B and C) Powder C. SA = surface area

Despite of the similar particle size distribution of powders A and B, the mean diameter of powder B is around 80% of the powder A. Since both powders have particles size restricted to around 100 μm , the largest mean diameter of powder A is correlated to the small amount of fine particles (<10 μm), resulting in a narrow distribution. Powder C shows a completely different trend. It displays a pronounced amount of fine particles (~20%). Consequently, its surface area is much larger (Table 5.5).

Table 5.6 reports the microhardness of the three powders as well as the concentration of the main alloying elements.

Table 5.6 - Hardness, Cr, Mo and C extents of the Co-28Cr-6Mo powders.

Powder Code	Hardness [HV _{0,02}]	Cr	Mo	C
A	415 ± 13	28,5	6,1	0,025
B	438 ± 13	29,2	5,6	0,017
C	413 ± 12	28.9	5.5	0,008

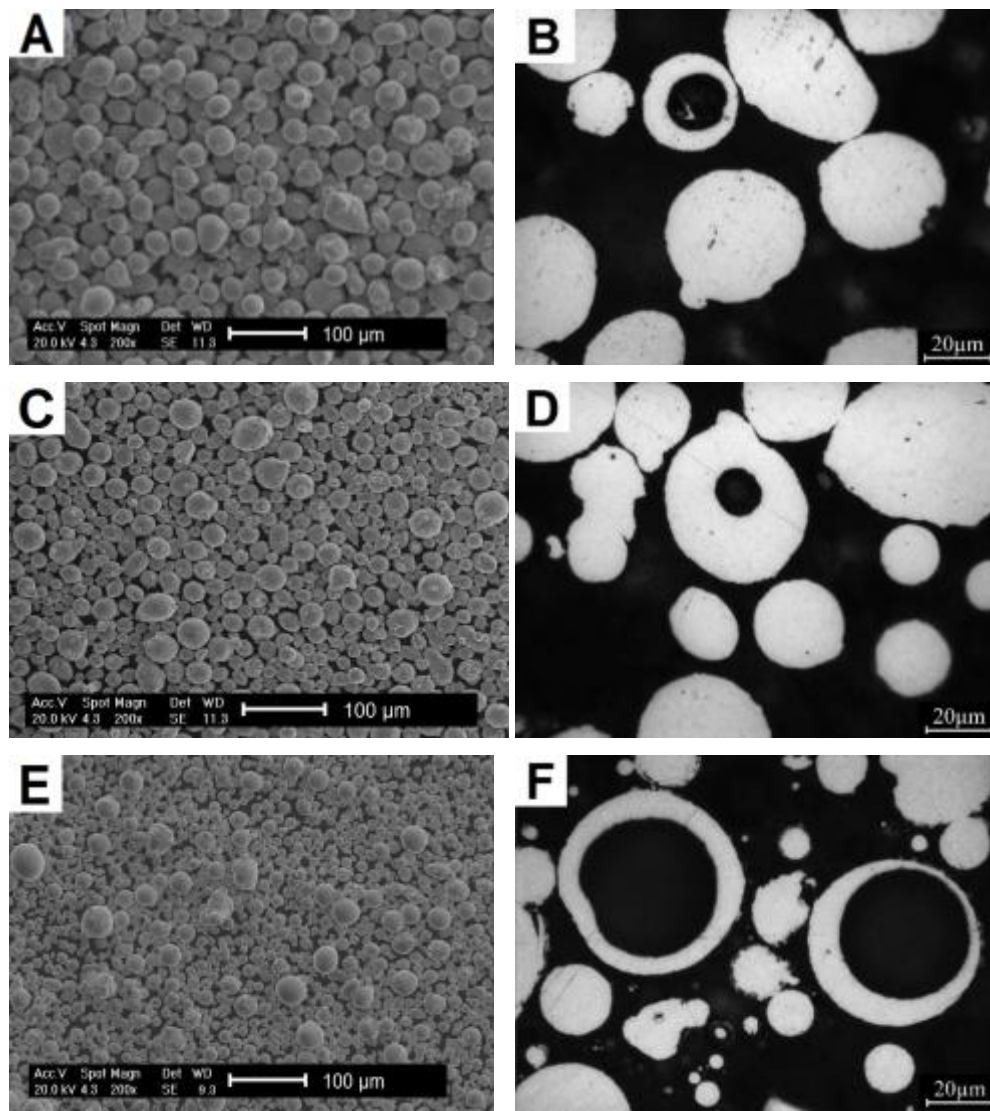


Fig. 5.17 - Particles shape and microstructure of powders. A) and B) Powder A; C) and D) Powder B; and E) and F) Powder C.

Another peculiar characteristic outcomes from the microstructural analysis (Fig. 5.17). The amount of particles containing voids is much higher in powder C than in the other two powders, which are instead very similar.

Figure 5.18 shows the microstructure of sintered specimens obtained with the three powders in the following conditions: 900 °C, 60 MPa, 5 minutes isothermal holding.

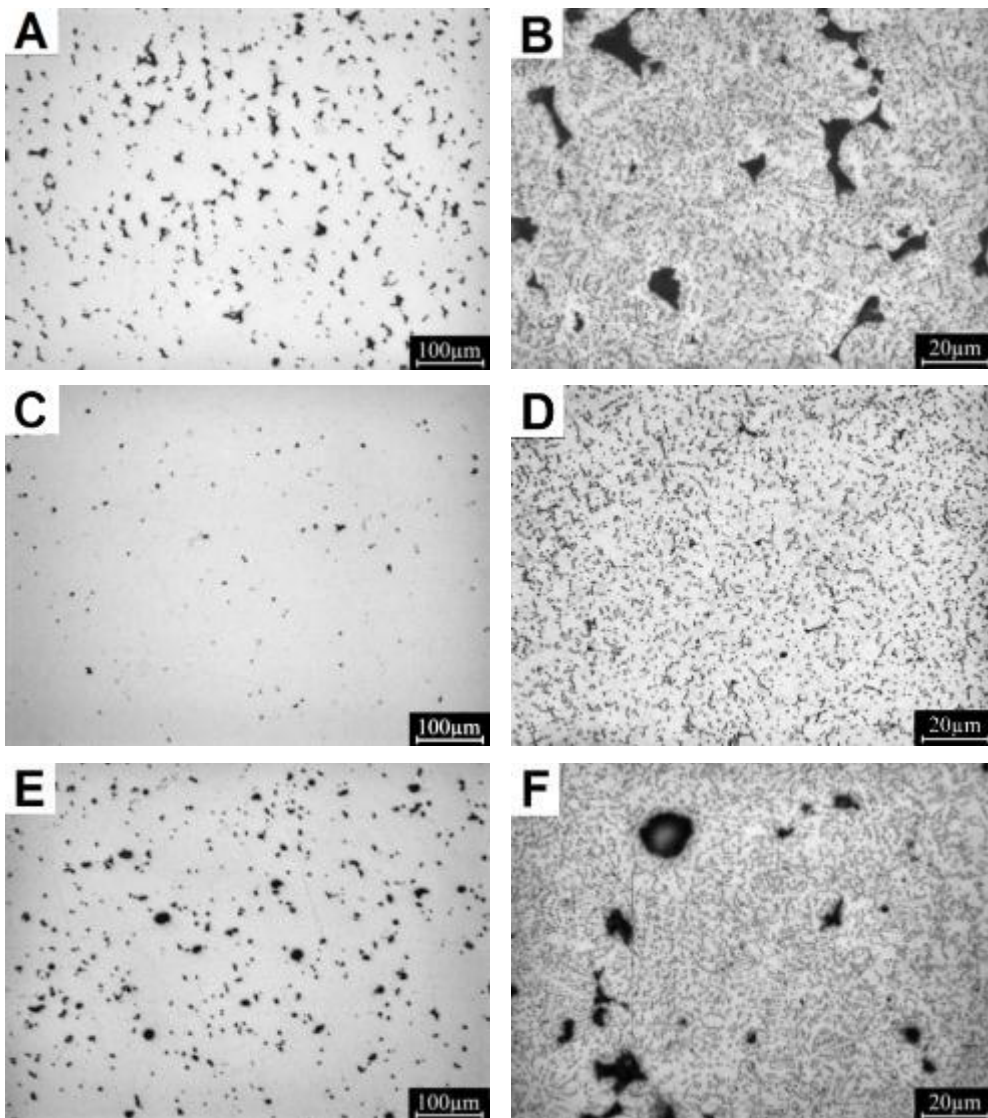


Fig. 5.18 - Microstructures of materials sintered at 900 °C, 5 minutes and 60 MPa. A) and B) Powder A; C) and D) Powder B; E) and F) Powder C.

The presence of pores in materials A and C is evident, resulting in a low relative density. In particular the material sintered with powder C shows two typologies of pores. The former is around 10 μm and is very irregular, lying between particles (incomplete sintering), the latter is about 20 μm and is relatively rounded, coming from particles containing voids. A particle containing unmodified preexisting void can be seen in Fig. 5.19. Density, hardness and microhardness of these three selected materials are reported in Table 5.7.

Table. 5.7 - Relative Density, Hardness and Microhardness attained after SPS at 900°C, 5 minutes and 60 MPa

Material Code	Relativity Density [%]	Hardness [HV ₃₀]	Hardness [0,05]
A	95,60	318 ± 3	451 ± 19
B	99,04	430 ± 2	462 ± 11
C	97,34	418 ± 4	455 ± 9

While hardness is dominated by density, microhardness is quite similar.

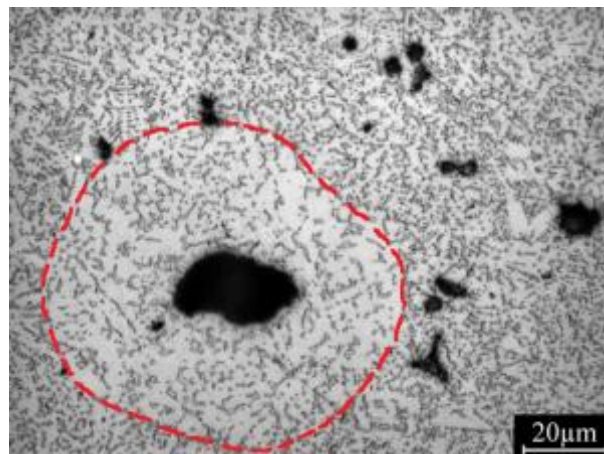


Fig. 5.19 - Microstructure of the material A. In evidence a preserved particle.

5.1.5 - Mechanical Properties

Tensile and bending reverse fatigue tests were carried out. Microstructures and fractographies are presented for complementary discussion. For sake of comparison the as cast material was tested as well.

5.1.5.1 - Tensile properties

Differently from the samples used for the optimization of the process parameters (sections 5.1.1 - 5.1.4), whose were discs of 20 mm in diameter and 10 mm of height, tensile specimens were machined from bars of 90 mm in length 10 mm in width and 7 mm in height. The microstructure of the gage section of the as cast tensile specimen is shown in [Fig. 5.20](#).

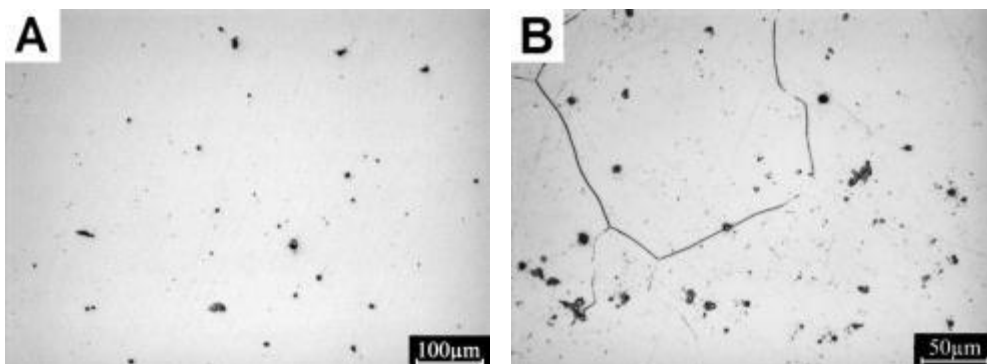


[Fig. 5.20](#) - Microstructures of as cast tensile specimen.

Microstructure is characterized by large grains with some residual micropores. Hardness and microhardness of materials are reported in [Table 5.8](#).

Table 5.8. Hardness and microhardness of materials sintered at 900°C, 950°C and of as cast material.

Material	Hardness [HV ₃₀]		Microhardness [HV _{0,05}]	
	gage region	grip region	gage region	grip region
SPS 900°C	435 ± 1	441 ± 2	446 ± 4	452 ± 9
SPS 950°C	369 ± 2	428 ± 3	427 ± 8	440 ± 8
As Cast	294 ± 6	297 ± 3	383 ± 5	382 ± 4

Authors [89,90] demonstrated that in some cases a temperature gradient as large as 150 °C can arise during sintering by SPS. In this case study, in specific in this asymmetrical geometry, a gradient of about 50 °C was experimentally confirmed. It is attributed to carbides dissolution since density is equivalent in the two regions and microhardness varied as well. Hardness and microhardness reported in Table 5.8 clearly establish the existence of such a temperature gradient, in particular in the tensile specimen sintered at 950°C. Fig. 5.21 shows the hardness (HRC) variation along the axis of the bar produced by SPS at 900 °C and 950 °C.

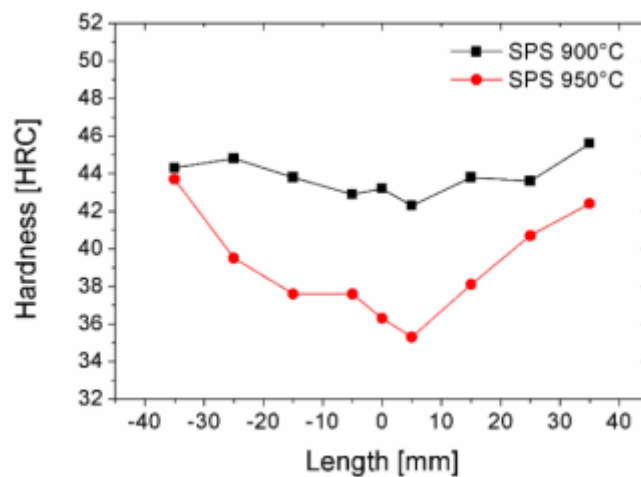


Fig. 5.21 - Hardness Rockwell C for tensile specimens sintered at 900 °C and 950 °C.

Fig. 5.22 shows the stress-strain curves of materials sintered at 900 °C and 950°C, and the as cast reference.

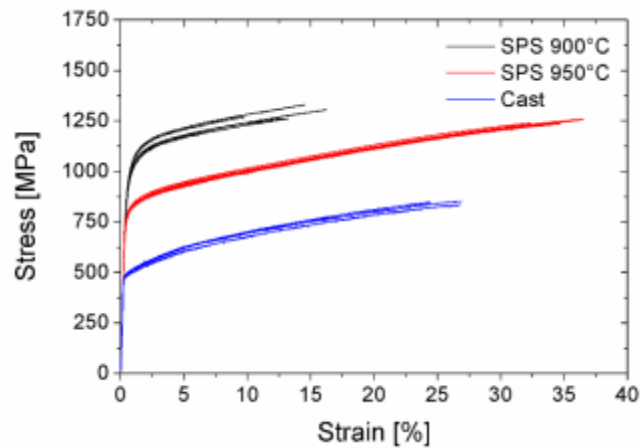


Fig. 5.22 - Tensile curves for materials sintered at 900°C and 950°C, and as cast version

SPS at 900 °C produces a material with the highest yield strength due to smaller grain size and carbides dispersion; in contrast the elongation is the worst. On the other hand, the material sintered at 950 °C exhibits both yield strength and Ultimate Tensile Strength (UTS) higher than the as cast reference, but also significantly greater ductility. Consequently, it shows the highest toughness due to the best combination of strength and ductility. Tensile properties are reported in Table 5.9 compared to the ISO biomedical standard specification.

Table 5.9 - Tensile properties of the materials sintered at 900°C and 950°C, as cast and ISO standard.

Material Condition	$\sigma_{0,2\%} \pm \text{STD}$ [MPa]	UTS $\pm \text{STD}$ [MPa]	$\Delta l \pm \text{STD}$ [%]
SPS 900°C	936 \pm 14	1284 \pm 31	13,3 \pm 3
SPS 950°C	778 \pm 7	1246 \pm 9	35,2 \pm 2
As Cast	490 \pm 8	845 \pm 8	26,7 \pm 2
ISO 5232-4	450	665	8,6

Both sintered and as cast materials match the ISO standards. Moreover, the material sintered at 900 °C shows the lowest but fully satisfactory percent elongation. Despite the higher amount of carbon (0,12%), large grain size is responsible for the inferior mechanical properties of cast material. Fracture surfaces of tensile specimens are shown in Fig. 5.23.

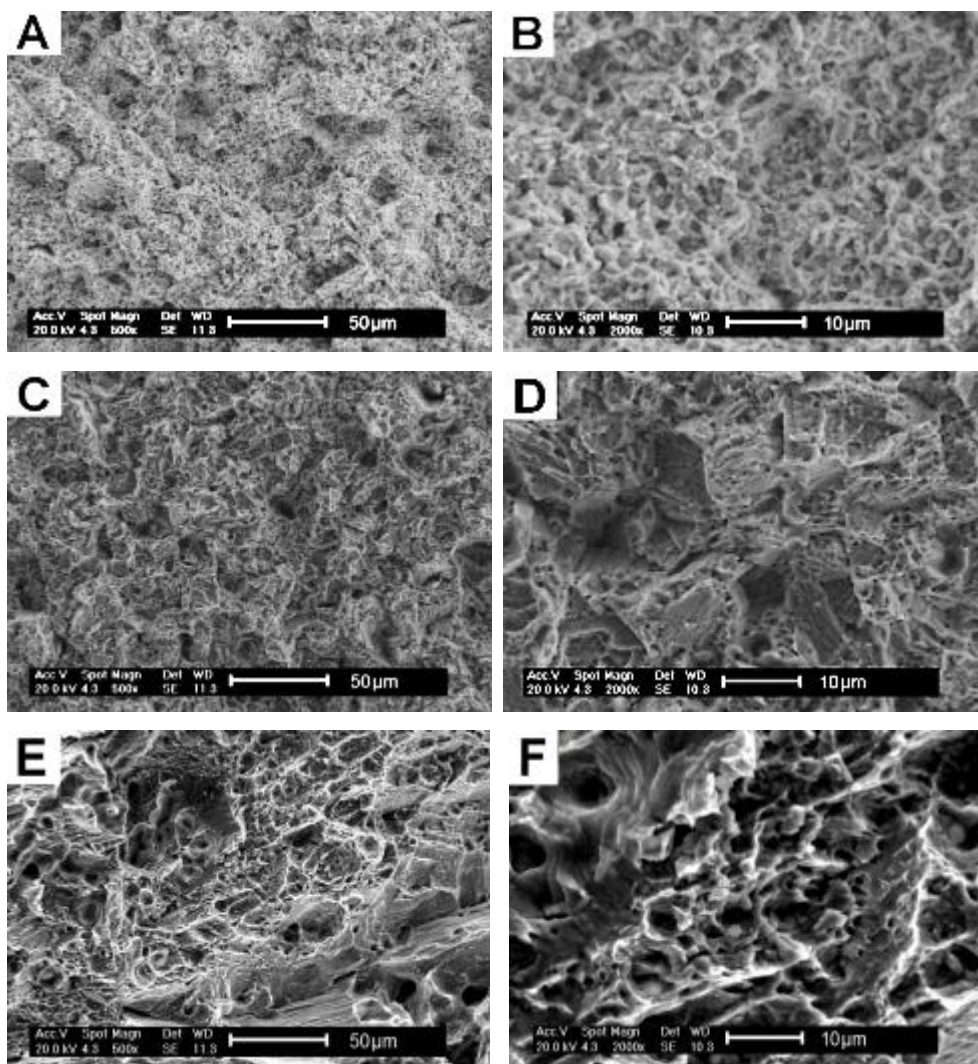


Fig. 5.23. Tensile fracture surfaces. A) and B) Sintered at 900 °C; C) and D) Sintered at 950 °C and E) and F) As Cast.

Dimples can be clearly seen in all surfaces, but those present in the as cast material are markedly larger than others, since grains are much larger, favoring void coalescences. Another noticeable characteristic is the occurrence of some flat surfaces indicating a fracture by quasi-cleavage, less intense in the material sintered at 950 °C, but evident in the as cast material. Finally, dimples in the material sintered at 900 °C are smaller than 2 microns and homogeneously distributed in whole fracture surface.

5.1.5.2 - Fatigue Properties

The fatigue resistance was investigated on the material with the higher yield strength and UTS, that is, that sintered at 900 °C. [Table 5.10](#) show the results of the stair case procedure on the sintered material and the as cast reference.

Table 5.10 - Stair case procedure table of sintered and cast materials.

Stress (MPa)	1	2	3	4	5	6	7	8	9	10	11	12	13	14	15
600	x														
585															
570															
555															
540		x													
525			x												
510															
495				x											
480						x						x			
465					o		x		x		o		x		x
450								o		o				o	
440	x														
425															
410															
395															
380		x													
365															
350			x												
335				x											
320					x										
305															
290						x									
275															
260							x		x						x
245								o		x		x		o	
230											o		o		

x = Failed; o = Run out; -- Sintered; -- As Cast.

Table 5.11 reports the fatigue resistance calculated by using the staircase procedure. As it can be seen, the sintered material is abundantly superior to the as cast one. The 50% survival probability fatigue resistance, as well as the yield stress in tensile tests, of the as cast material is indeed 52% of those shown by the sintered material.

Table 5.11 - Fatigue resistance of sintered and as cast version.

Material	Survival Probability		
	10%	50%	90%
SPS 900°C	494	464 ± 7	451
As Cast	256	245 ± 7	234

5.1.6 - Corrosion Properties

Corrosion can take place either localized or on the whole surface. In particular, the former case is much more common in cases related to implant failure [112]. This type of corrosion typically outcomes from pitting due to galvanic cell formation. Metal ions released from corrosion can induce tissue reactions, which in turn can seriously damage to some organs and vital functions [113].

5.1.6.1 - Open Circuit Potential (OCP) Test

Among the corrosion tests that metallic biomaterials have to fulfill for standards requirements, the OCP is the simplest. It consists in monitoring the potential between the material and the reference during immersion in a solution, either with purging gas or not. Basically, three aspects have to be considered: the free potential, the curve oscillation and the trend of potential variation.

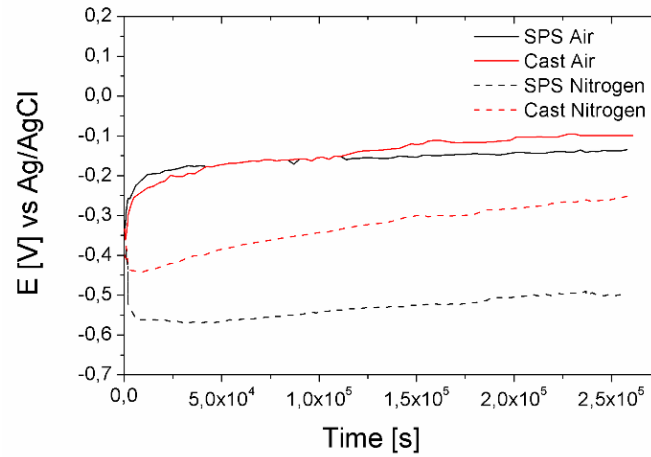


Fig. 5.24 - Open circuit potential curves for sintered and as cast materials

The sintered and the as cast materials responded very similarly to the OCP test in the purged air, as it can be seen in Fig. 5.24. Despite the presence of some peaks in the curve of the former, both materials show around -0,2V of free potential and a satisfactory stable curve, with tendentially increasing potential. Besides, the sintered material shows a pretty lower free potential in purged nitrogen environment (absence of oxygen). It may be correlated to the presence of larger grain boundary surface. Such evidence in any case does not mean a worse behavior, but it is an indication that materials respond differently to the absence of oxygen. Moreover, both materials present an increasing potential during the 72 hours of the test. This positive potential evolution in all cases indicates the formation of a protecting passivation layer, ensuring the long term application.

5.1.6.2 - Cyclic Potentialdynamic Polarization (CPP) Test

Metallic biomaterials contain a thin oxide protective layer (passivation layer). In order to evaluate the integrity of this protection the CPP test is usually carried out. Integrity is assessed by the well-known anodic polarization curve. The potential is varied and the range where the electric current is quasi-constant is denominated passivation range. The potential at the starting and at the end (breakdown potential) of this steady curve is an indication of the corrosion resistance. Moreover, the current density is related to the corrosion rate. The polarization curves for the sintered and the as cast materials are shown in Fig. 5.25.

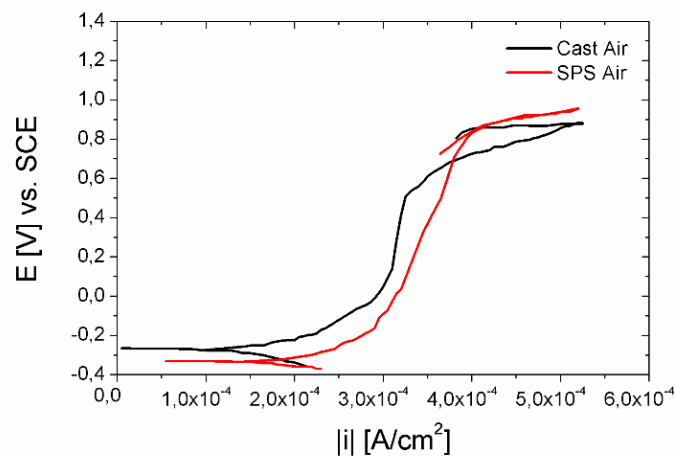


Fig. 5.25 - Anodic polarization curves of sintered and as cast materials

Both materials have a free potential around -0,2 V. By increasing the potential the current density slowly increases, but not considerably. It is called the passive region. The sintered material shows the passive behavior up to the breakdown of oxide layer (transpassivity) at around 0,8 V vs. Ag/AgCl with a passive current density of about 5×10^{-6} A/cm². The

as cast material shows a passive behavior up to the breakdown potential due to transpassivity of 0,6 V vs. Ag/AgCl with a passive current density of about 3×10^{-6} A/cm². Materials show similar corrosion potential and passive region, with a slightly higher density current for the sintered one.

In particular, if a damaged film is unable to repair itself, the cathodic reactions necessary to support corrosion can take place on the undamaged parts of the passive film, leading to rapidly accelerated corrosion at the damaged site.

5.2 - Ti-6Al-4V

The production of a fully dense Ti-6Al-4V alloy by SPS has been investigated and optimized in a previous work [114]. The SPS parameters are 850 °C, 5 minutes isothermal holding and pressure of 60 MPa. In the present study, the fatigue and corrosion properties have been investigated. The SPS parameters have been modified with respect to the previous work. Since compaction pressure was reduced from 60 MPa to 45 MPa, sintering temperature was increased up to 950 °C.

5.2.1 - Mechanical Properties

Tensile and bending reverse fatigue tests were carried out. Microstructures and fractographies are also presented for complementary discussion. For sake of comparison a wrought alloy (forged annealed hot rolled, in agreement with ASTM B348) was tested as well.

5.2.1.1 - Tensile Properties

The tensile specimen microstructures of the SPS and the wrought materials are shown in Fig. 5.26.

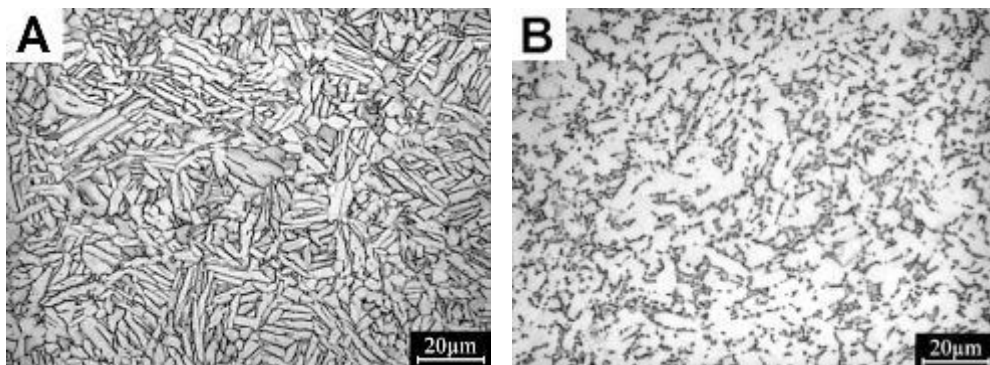


Fig. 5.26 - Microstructures of tensile specimen utile region.
A) Sintered and B) Wrought.

Some few pores are present in the sintered material, whose actually do not significantly alter density, denoting that selected SPS parameters were adequate. Microstructure of the sintered material consists of lamellar alpha phase plus interlaths beta phase. The wrought microstructure consists of globular alpha phase plus coarsened beta phase. Such a microstructure comes from the conventional thermomechanical treatment followed by annealing into alpha plus beta field. The wrought alloy has a slightly higher hardness than the sintered one, as reported in Table 5.12.

Table 5.12. Hardness and microhardness of material sintered at 950 °C and wrought version.

Material	Hardness [HV ₃₀]	Microhardness [HV _{0,05}]
Wrought	318 ± 3	333 ± 9
SPS 950°C	307 ± 2	318 ± 3

Such higher hardness is evidently related to the amount and arrangement of beta phase. Stress-strain curves of the sintered and the wrought materials are shown in Fig. 5.27.

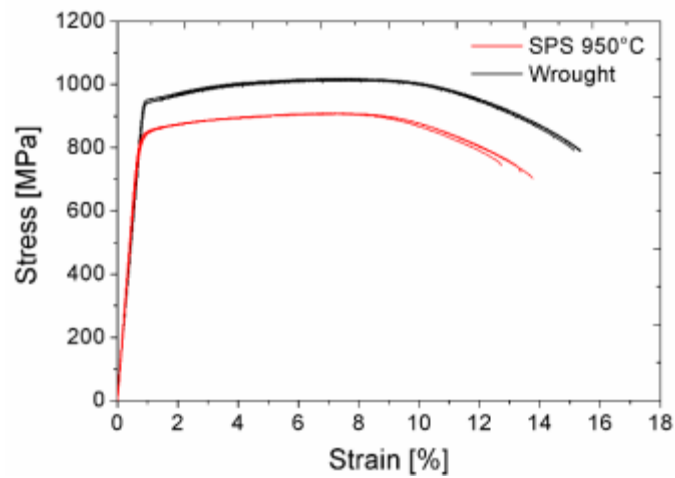


Fig. 5.27 - Tensile fracture surfaces.

Both elastic and plastic behaviors are very similar. The Ti-6Al-4V does not show significant strain hardening and plastic instability (necking) at the end of the plastic region is evident.

Tensile properties are summarized in Table 5.13. The sintered material presents lower strength and ductility than the wrought material. Properties are also lower than those shown by Molinari and Zadra [111]. In any case, sintered material fully attained the ASTM standards.

Table 5.13 - Tensile properties of material sintered at 950 °C and wrought version.

Material	$\sigma_{0,2\%} \pm \text{STD}$ [MPa]	UTS $\pm \text{STD}$ [MPa]	$\Delta l \pm \text{STD}$ [%]
SPS 950°C	841 \pm 3	907 \pm 1	13 \pm 0,4
Wrought	950 \pm 4	1015 \pm 3	15 \pm 0,2
ASTM F1472 – 02	780	860	10

Fracture surfaces of sintered tensile specimens are shown in Fig. 5.28.

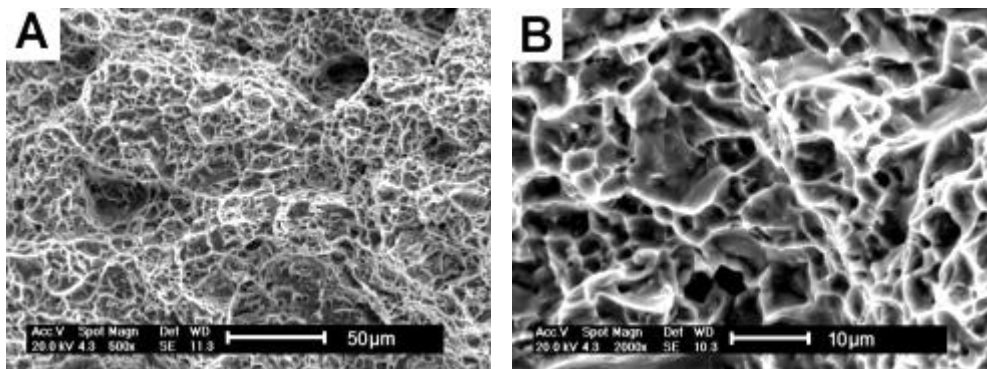


Fig. 5.28 - Fracture surfaces of sintered tensile specimens.

Fracture surfaces are quite similar. Slight larger dimples are seen in the wrought material. This behavior is supported by the coarse microstructure of the wrought material, which favors void coalescence. On the other hand, thin alpha lamellae promote dislocation pile-up and, in turn, lower ductility and smaller dimples.

5.2.1.2 - Fatigue Properties

Table 5.14 reports the results of the staircase procedure.

Table 5.14 - Staircase procedure table.

Stress (MPa)	1	2	3	4	5	6	7	8	9	10	11	12	13	14	15
595	x														
580															
565	x														
550		x													
535															
520		x	x											x	
505					x				x		x		o		o
490			x	o	x	x		o		o	x	o		x	
475				o			xo			o			o		
460						o			o			o			x
445								o							
430															
415															

x = Failed; o = Run out; -- Wrought; -- SPS 950°C

Table 5.15 summarizes the fatigue resistance. The superior fatigue resistance shown by the wrought material is due to the globular alpha phase, which enhances high cycle fatigue (HCF) resistance [58].

Table 5.15 - Fatigue resistance of sintered and wrought materials.

Material	Survival Probability		
	10%	50%	90%
SPS 950°C	490	472 ± 13	454
Wrought	515	500 ± 11	484

5.2.2 - Corrosion Properties

As in the case of the Co-28Cr-6Mo alloy, both OCP and CPP corrosion tests were carried out.

5.2.2.1 - Open Circuit Potential (OCP) Test

Open circuit potential curves for the sintered and the wrought material are shown in Fig. 5.29.

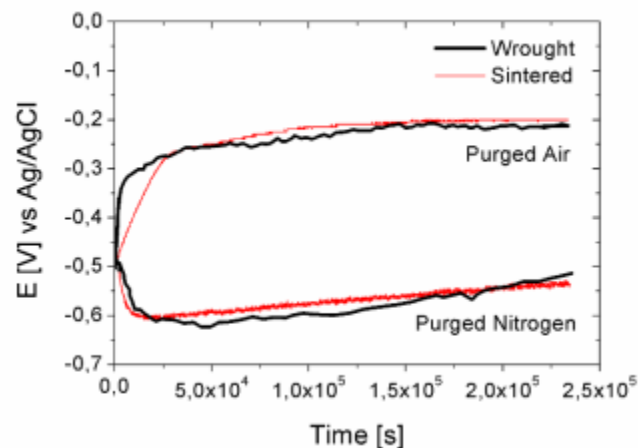


Fig. 5.29 - Open circuit potential curves for sintered and wrought materials.

Despite the presence of some instability in the curves of the wrought material, both materials reached the free potential at around -0,5 V. When purged air the sintered material takes more time to reach the steady state, but all curves have a tendency to increase. This positive potential evolution in all cases indicates the formation of a protecting passivation layer, ensuring the long term application.

5.2.3.2 - Cyclic Potentialdynamic Polarization (CPP) Test

In order to evaluate the integrity of the oxide protective layer and the current density at passive region the CPP test was carried in purged nitrogen.

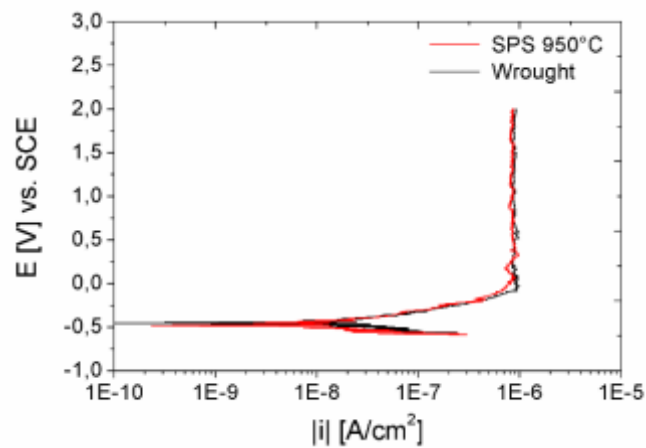


Fig. 5.30 - Cyclic anodic polarization curves of sintered and wrought

Both materials have a free potential around -0,5 V, as shown in Fig. 5.30. By increasing the potential the current density increases up to reach the stable region (passive region). Corrosion oxide layer breakdown (transpassivity) was not attained in both cases up to 2 V vs. Ag/AgCl. Passive current density was about $1 \times 10^{-6} \text{ A/cm}^2$ for both materials. Materials show a very similar corrosion free potential and passive region.

5.3 - Summary of the Results

Full Density Substrate (Co-28Cr-6Mo):

- Almost full density (98,7%) was achieved at 900 °C using 5 minutes of dwell time and 45 MPa of compaction pressure. A higher temperature does not improve density. Pores are isolated.
- The maximum density (99,4%) was achieved at 900 °C, 5 minutes and 70 MPa. A full density (100%) was not achieved due to the limit imposed by mechanical resistance of the dies.
- Only M_7C_3 carbides were identified; .
- Carbides are slightly dissolved in the matrix up to 900 °C. partially dissolved at 950 °C and completely dissolved at 1050°C.
- Pressure does not affect carbides dissolution.
- At 1050 °C an appreciable grain growth take place.
- Hardness follows the densification curve up to the maximum density. Increasing temperature promotes carbide dissolution and hardness decreases. Consequently, interstitial carbon on the matrix is less effective than carbides in hardening the material.
- Microhardness does not change up to 900 °C. At higher temperature it decreases as in the case of hardness.
- Voids located within the powder particles are not eliminated during SPS at the processing parameters used;
- Sintering at 900 °C, 5 minutes and 60 MPa resulted in Yield Strength and UTS twice of those of the cast material, taken as a reference, while percent elongation at fracture is about 50% lower.
- Sintering at 950 °C, 5 minutes and 60 MPa resulted in a material with Yield Strength and UTS and percent elongation at fracture significantly higher than those of the cast material.

- Fatigue resistance follows tensile properties; the material sintered at 900 °C is about two times more resistant than the cast material.
- A lower free potential is achieved by the sintered material in comparison to the cast material when nitrogen was purged during OCP test. Both materials show a trend of increasing potential.
- On the cyclic potentiodynamic polarization tests a very similar behavior was observed between SPS and cast material. Both materials re-passivate after transpassivity.

Full Density Substrate (Ti-6Al-4V):

- Tensile properties of the material sintered at 950 °C, 5 minutes and 45 MPa of pressure are slightly lower than those of the wrought material taken as a reference.
- Fatigue resistance follows tensile properties. The sintered material has a slightly lower fatigue resistance than the wrought one.
- Corrosion tests are definitely similar for both materials.

Chapter 6 - CO-SINTERING

Co-sintering of different materials may lead to insufficient densification as well as to extensive interfacial reactions. SPS, on the other hand, is expected to limit such drawbacks since sintering is enhanced by pressure and by the specific heating mechanisms, leading to a low heat input.

Co-sintering of either the Co-28Cr-6Mo and Ti-6Al-4V alloys with the cp-Ti is discussed in this chapter. Microstructural investigation and diffusion calculations at the interfaces are the main topics. For both the systems the study of the fatigue resistance of a substrate with a porous coating is presented at the end of each section.

6.1 - Cp-Ti/Co-28Cr-6Mo

Two strategies are proposed to obtain the joining of materials: co-sintering and sinter-bonding. The former consists in the concurrently sintering of both powders. The latter consists in the sintering of a powder on other previously sintered material. Both sintering the cp-Ti powder on previously sintered Co alloy and sintering the Co alloy powder on previously sintered cp-Ti were carried out.

6.1.1 - Microstructure

The Co-28-Cr-6Mo alloy microstructure when co-sintered at 1000 °C, 5 minutes and 45 MPa or 60 MPa is shown in [Fig. 6.1](#).

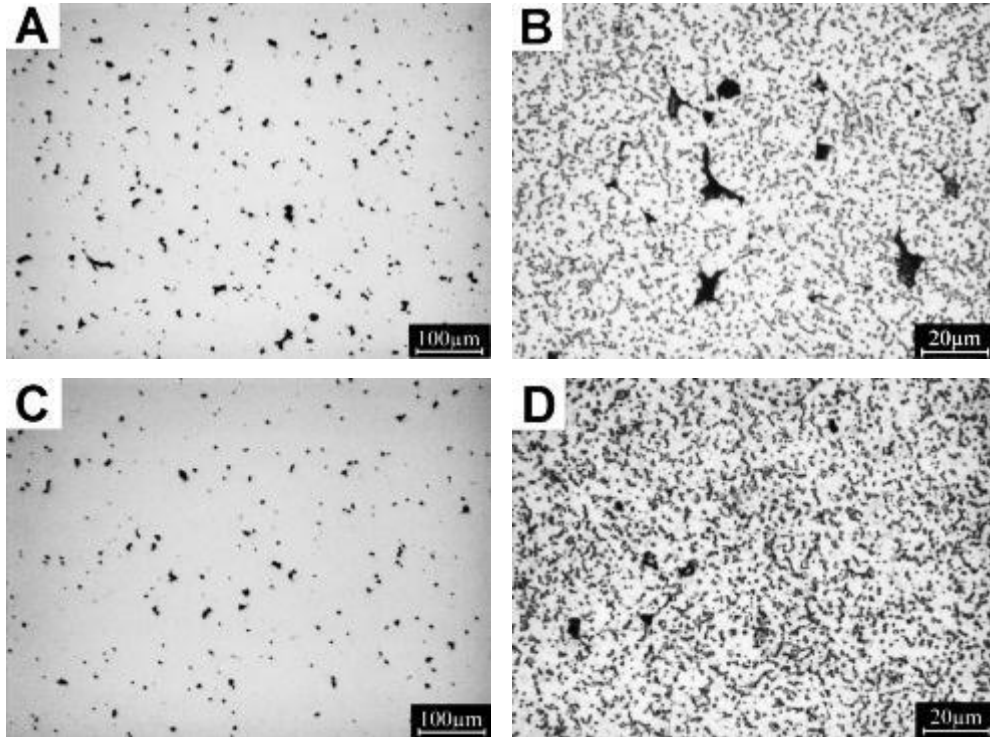


Fig. 6.1 - Microstructure of the Co-28Cr-6Mo sintered at 1000 °C, 5 minutes and 45 MPa (A and B) or 60 MPa (C and D).

The amount of carbides is larger than that obtained after sintering of Co alloy alone at the same nominal temperature, and corresponds to that observed after sintering at a lower temperature (~ 900 °C, chapter 5). Pores are seen in higher amount in the material co-sintered at 45 MPa than at 60 MPa, as it was expected. Co-sintering resulted in densities of 97,2% and 98,4%, respectively. It denotes a noticeable reduction in sintering efficiency in comparison to that in the Co alloy alone, since at 900 °C density was 98,7% and 99,04%, respectively. As in SPS powders are heated up by pulsed electric current, an ohmic resistance is imposed in the system by the presence of material. When two powders are concurrently sintered (co-sintering) this ohmic resistance is altered.

Fig. 6.2 shows the interface microstructure after etching.

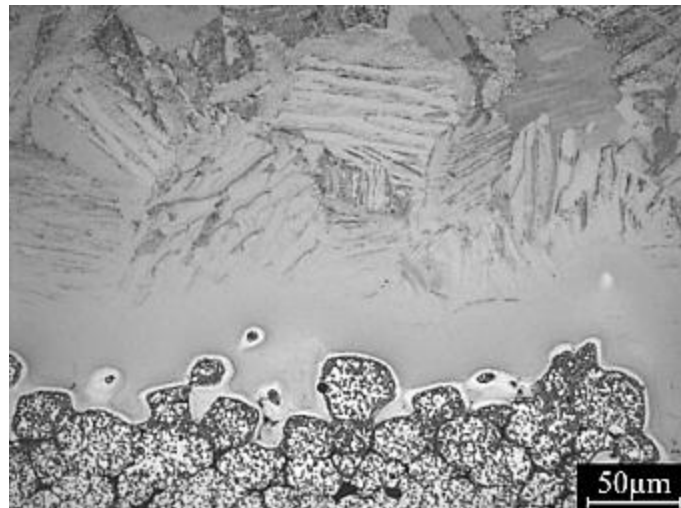


Fig. 6.2 - Etched Interface microstructure after co-sintering at 45 MPa.
Upper side Ti, lower side Co alloy.

Despite of the different densities, co-sintering at 45 MPa and 60 MPa produces an interface region with the same features. It is irregular due to the penetration of the Co alloy particles in the cp-Ti, since the former has a higher hardness. The cp-Ti microstructure shows a layer of around 50 μm close to the interface and a lamellar layer up to a distance of around 200 μm . Beyond this distance the typical microstructure of the cp-Ti₂ is observed. The microstructure of the cp-Ti in the interface region is thus modified, likely by the presence of diffused alloying elements. On the other hand, the Co alloy does not show a different microstructure between the interface region and the bulk. Moreover, on the Co alloy interface a lower sintering efficiency is denoted by the morphology of the particles, which appear as only slightly deformed.

6.1.2 - Sinter-bonding

Pre-sintering and sinter-bonding cycles were carried out at 1000 °C, 5 minutes and 60 MPa. The microstructure of the interface after sinter-bonding is shown in Fig. 6.3.

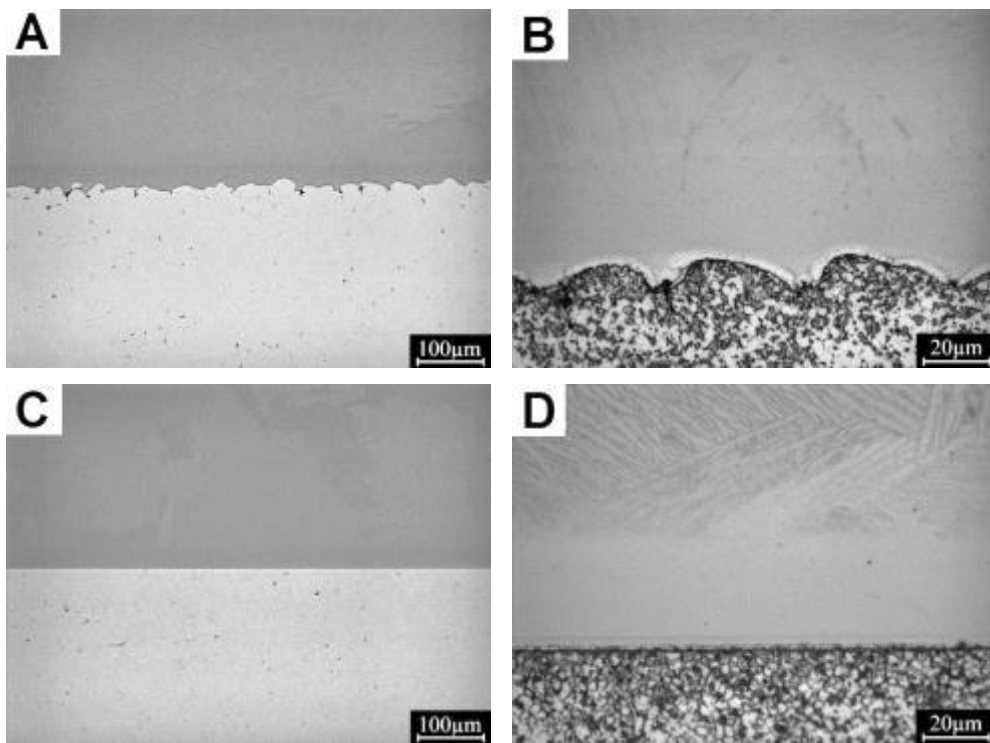


Fig. 6.3 - Interface microstructure after sinter-bonding. A) and B) Sinter-bonding of Co alloy powder on a pre-sintered cp-Ti; C) and D) Sinter-bonding of cp-Ti powder on a pre-sintered Co alloy.

In the case of the sinter-bonding of Co alloy powder on the pre-sintered cp-Ti (Fig. 6.3A and 6.3B), the interface is still irregular owing to the harder Co particles indentation of the sintered titanium substrate. In the other case

(Fig. 6.3C and 6.3D), the interface is quite flat since the Ti particles cannot indent the sintered Co alloy substrate due to their lower hardness. In both sinter-bonding configurations cp-Ti attained full density (no pores). Co alloy on the other hand attained 98,7% of density when sinter-bonded on the pre-sintered cp-Ti and 99,2% when pre-sintered.

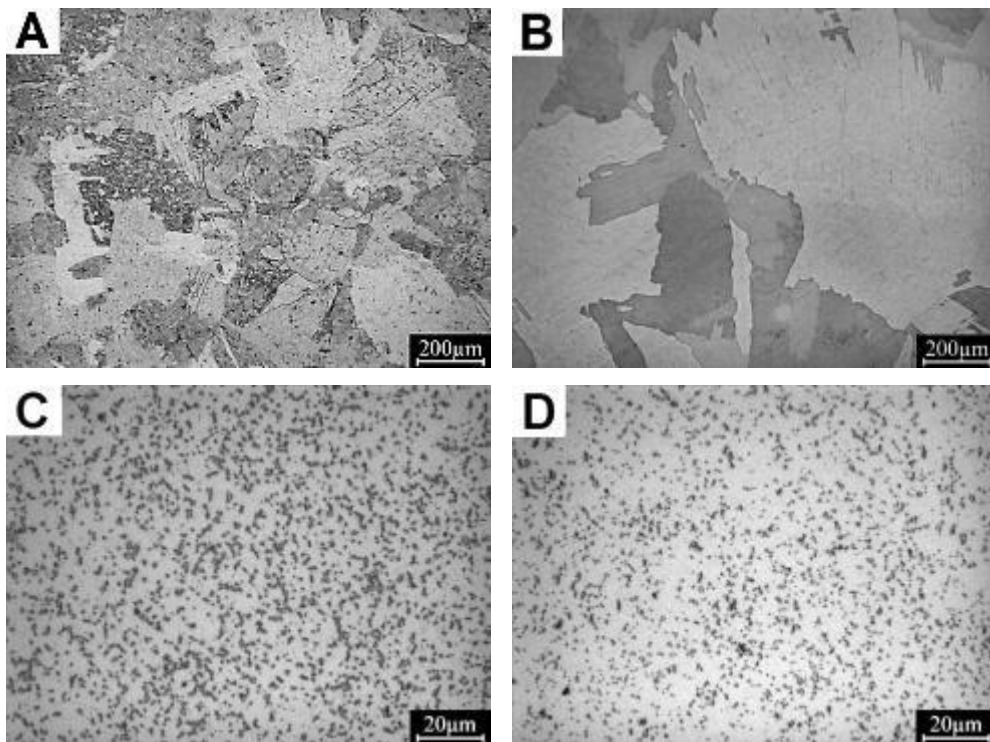


Fig. 6.4 - Microstructure of materials sintered (left) and subsequent sinter-bonded (right). A) and B) titanium, C) and D) cobalt alloy.

An interesting difference between the two sinter-bonded materials is related to grain growth in the previously sintered material, which is exposed to two SPS cycles (sintering followed by sinter-bonding). In the Co alloy carbides are only slightly dissolved; their presence prevents grain growth thanks to

grain boundary pinning. On the contrary, the cp-Ti undergoes an extensive grain growth. Fig. 6.4 shows the cp-Ti and Co alloy after sintering and after sinter-bonding.

6.1.3 - Interface Characterization

Fig. 6.5 shows the Ti, Co, Cr and Mo concentration line profiles measured by EDXS across the interface of the specimen obtained by sinter-bonding the cp-Ti powder on the previously sintered Co alloy. This profile is representative of the other two specimens discussed, since the significant difference among them is rather correlated to the interfacial contour.

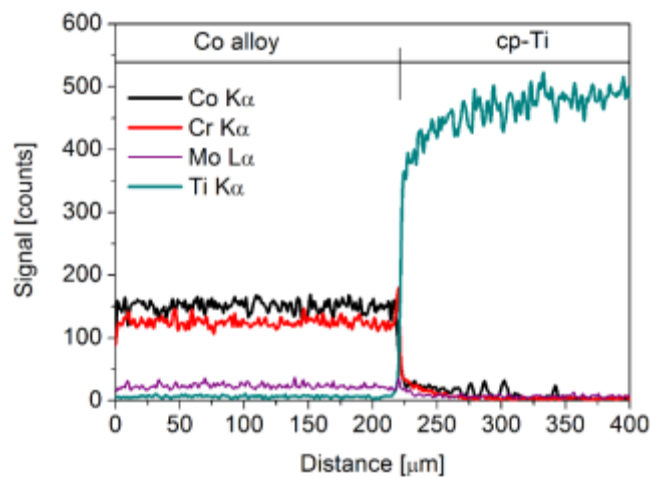


Fig. 6.5 - EDXS line profile analysis at the interface of sinter-bonded cp-Ti powder on the pre-sintered Co alloy.

Titanium does not diffuse into the Co alloy, whilst Co, Cr and Mo diffuse into cp-Ti. The total diffusion depth corresponds to about 200 μm and the diffusion distances of Co, Cr and Mo are different.

EDXS analyses were carried out on areas of approximately $6\ \mu\text{m} \times 12,5\ \mu\text{m}$ (longer dimension orthogonal to the interface) every $25\ \mu\text{m}$ from the interface. The diffusion profiles are reported in Fig. 6.6.

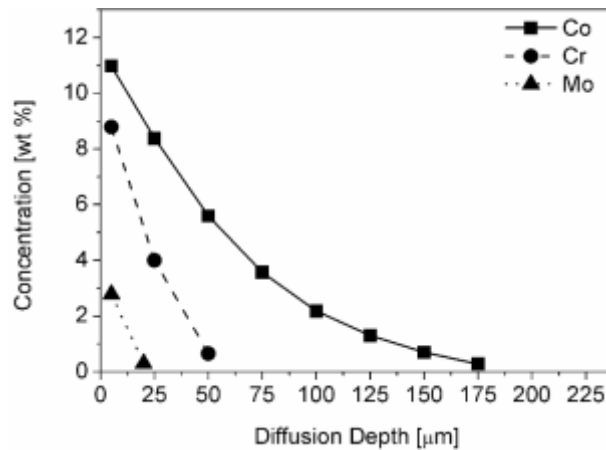


Fig. 6.6 - Diffusion profiles of Co, Cr and Mo into cp-Ti.

The distance reported in the x axis is relevant to the position of the center of the selected area. The diffusion distance of Mo, Cr and Co are <25 , 50 and $175\ \mu\text{m}$, respectively. As the three elements are beta stabilizers [58], the $50\ \mu\text{m}$ thick white layer close to the interface (Fig. 6.3 B) is beta-Ti phase. The thickness of this layer is comparable to the Cr diffusion depth. Where only cobalt is present a lamellar alpha-beta phase is formed. A similar microstructure evolution in titanium was observed when it was co-sintered with duplex stainless steels by [115,118], stabilized by chromium diffusion.

The microstructural analysis shows that the thickness of the lamellar alpha-beta phase is around $200\ \mu\text{m}$, slightly greater than the distance from interface at which the cobalt concentration detected by area microanalyses falls to zero. Spot analyses were then carried out on the beta lamellae. Here, the cobalt content was systematically higher than the average value

measured at the same distance, as shown in Fig. 6.7, and the diffusion depth of cobalt corresponds to the thickness of the biphasic lamellar microstructure.

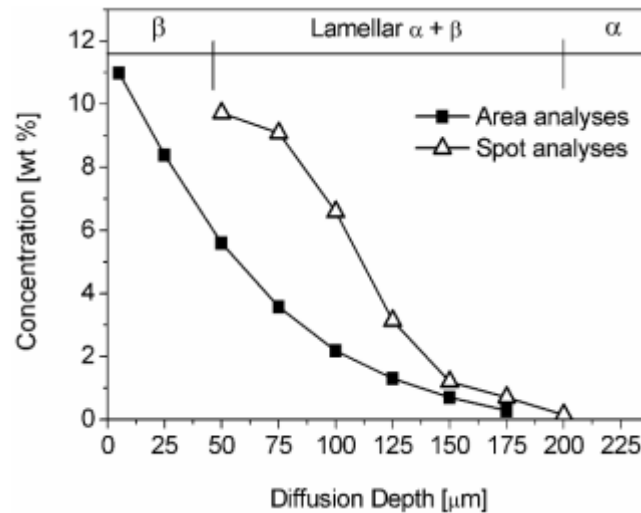


Fig. 6.7 - Spot analyses on the beta-Ti lamellae.

Since lamellae are very thin, their higher cobalt concentration is not detected by the area microanalysis, since it gives the average concentration in the whole area involved. The agreement between the microstructure and the Co concentration in the lamellae is satisfactory.

Fig. 6.8 shows a combination of EDXS analysis and the microstructural image in a 3D map.

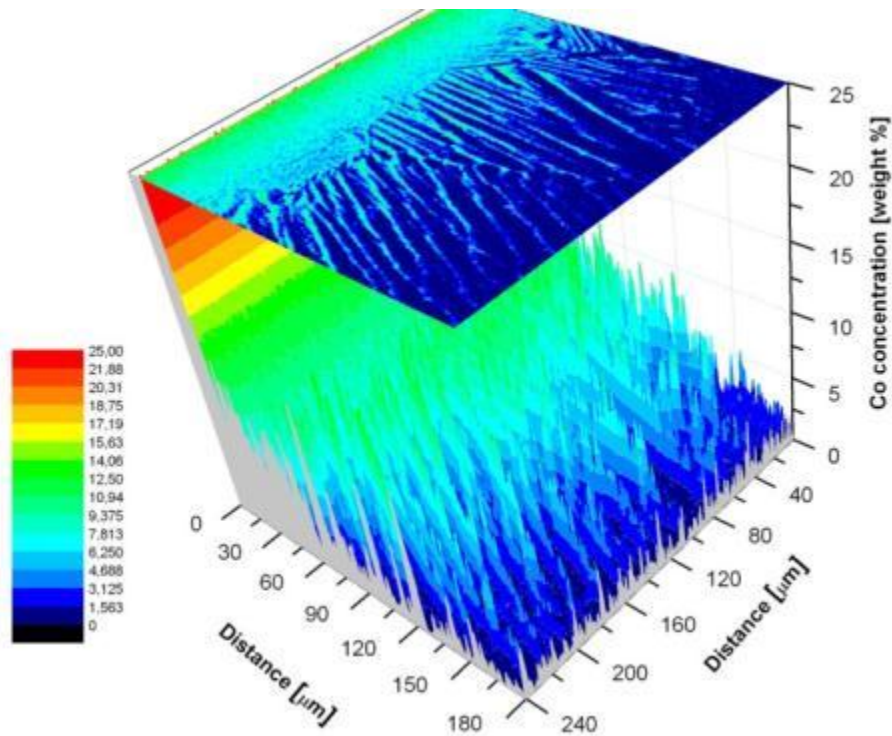


Fig. 6.8 - Cobalt concentration map combined to the lamellar beta Ti microstructure. 3D view.

Cobalt content gradually decreases, but a higher concentration in comparison to area analyses is detected in the lamellae. It occurs due to the cobalt partitioning during phase transformation.

The different diffusion distances of the three elements are due to different diffusion coefficients. The diffusion depths can be calculated to confirm the results of the microanalysis.

Table 6.1 reports the frequency factor (D_0) and activation energy (Q_d) for diffusion of Co, Cr and Mo in beta-Ti [119]. The diffusion coefficient D at 1273 K is calculated with Equation (1)

$$D = D_0 \exp(-Q_d/RT) \quad (1)$$

and is reported in the third column of the [Table 6.1](#). The diffusion depth x at which the concentration of the three elements is 0,01% was calculated by means of [Equation \(2\)](#) and is reported in the last column of the same table.

$$(C_x - C_0) / (C_s - C_0) = 1 - \operatorname{erf}[x/2(Dt)^{1/2}] \quad (2)$$

Here C_x is the concentration at the distance x and time t , C_s is the concentration at the interface and C_0 is the initial concentration in titanium. The interface concentrations measured by EDXS after 300 s at 1273 K are 10,98, 8,79 and 2,78 wt.% for Co, Cr and Mo, respectively. The concentrations at the interface are in a different ratio than the composition of the Co alloy. In particular, the Cr/Co ratio is around 0,5 in the alloy and 0,8 in beta-Ti at the interface; and the Mo/Co ratio is 0,1 and 0,3, respectively. This relative enrichment of Cr and even more of Mo is due to the different solubility of the three elements in beta titanium at the sintering temperature reported in the fourth column of [Table 6.1](#).

Table 6.1 - Frequency factor (D_0), activation energy (Q_d), diffusion coefficient (D), solubility (S), diffusion depth ($x_{0,01\%}$) of Co, Cr and Mo at 1273 K for 300 s in β -Ti

	$D_0 \cdot 10^{-7}$ ($\text{m}^2 \text{s}^{-1}$)	Q_d (KJ mole^{-1})	$D \cdot 10^{-13}$ (m^2/s)	S (wt %)	$x_{0,01\%}$ (μm)
Co	12,0	30,6	66,9	17,8	212
Cr	9,5	37,6	3,2	32,8	50
Mo	8,0	43,0	0,3	100	14

The calculated diffusion depth of the three elements corresponds quite well with the measured one by the microanalysis.

The interface zone of the specimen obtained by sinter-bonding the cp-Ti powder on the previously sintered Co alloy is shown in Fig. 6.9 at high magnification. It is very similar to that formed in the specimens produced with the other two strategies.

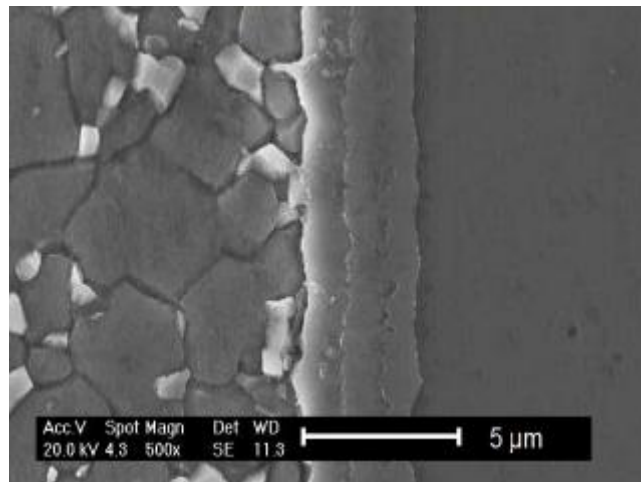


Fig. 6.9 - Interface region showing a layer constituted of three sub-layers.

An interaction layer is revealed, 3-4 μm thin, and constituted by three sub-layers of about 1 μm thickness. The concentration line profiles (Fig. 6.10) confirm that the layer is effectively constituted by three sub-layers of similar thickness (around 1 μm).

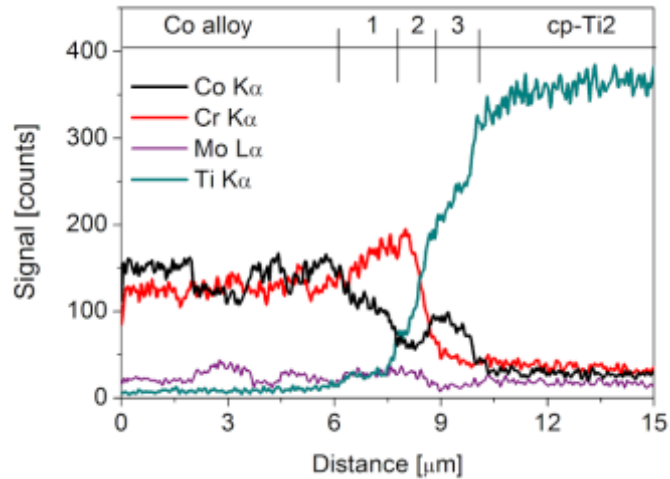


Fig. 6.10 - Concentration line profiles concerning the thin layer.

On moving from the Co alloy (layer 1) towards cp-Ti (layer 3) it may be observed that:

- i) Ti increases continuously;
- ii) Co decreases (layer 1) then increases reaching a maximum at the interface between the second and the third layers and then decreases;
- iii) Cr first increases (layer 1), then decreases sharply (layer 2) and stabilizes (layer 3);
- iv) Mo is stable in the first layer, then decreases in the second layer and remain stable in the third one.

The concentration profiles of Cr in the first layer and of Co in the second layer are not consistent with the concentration gradients. The effect of migrating elements on activity is responsible for this apparent ambiguity. For instance, Kundu and Chatterjee [115-118] show similar chromium enrichment at the interface between a duplex stainless steel and titanium, due to the effect of titanium migrating towards the stainless steel, which decreases the chromium activity. As a consequence, chromium diffusion takes place down the activity gradient that is different from the

concentration gradient. The same effect can be hypothesized here to justify the inversion of the chromium gradient in the layer close to cobalt alloy. An analogous effect could justify the cobalt profile in the second layer. [Table 6.2](#) reports the average Co, Cr, Mo and Ti concentrations in the three layers.

[Table 6.2](#) - Chemical composition of the three bonding layers

Layer	Weight %			
	Ti	Co	Cr	Mo
1	3,8	46,0	41,3	8,8
2	19,9	30,6	39,5	10,0
3	47,1	37,5	12,5	2,8

The system is rather complex and no reference data are available in literature to interpret the constitution of the three layers. The binary and ternary phase diagrams [120,121] do not support a reliable interpretation. On the basis of the analyses and of the reference data, it may be only hypothesized that the layers contain some intermetallic compounds as sigma phase in layer 1, TiCo and TiCr₂ in layers 2 and 3 and Ti₂Co in layer 3. This hypothesis has to be verified by a detailed characterization of the three layers. objectives futures

6.1.4 - Fatigue Properties

Fatigue specimens were prepared by sinter-bonding the presintered cp-Ti/CP blend with the Co-28Cr-6Mo alloy with subsequent calcium phosphate extraction.

The porous structure is very similar to that discussed in chapter 3. Samples were produced according to the following procedure:

- i) Mixed blend pre-sintering at 600 °C and 20 MPa without any holding time (1,5 x 12 mm² section and 30 mm length);
- ii) Positioning of the pre-sintered body into a proper cut-down punch (inferior), centered and aligned with the lengthier die cavity axis;
- iii) Die feeding with the Co-28Cr-6Mo powder to fill-up a post sintering volume of 6 mm height, 12 mm width and 90 mm length;
- iv) Positioning of the second pre-sintered body into the another cut-down punch (superior) with subsequent die closing;

Table 6.3 reports the results of the staircase procedure of the full density and the porous Ti coated cobalt alloy.

Table 6.3 - Stair case procedure for fully dense and porous coated material

Stress (MPa)	1	2	3	4	5	6	7	8	9	10	11	12	13	14	15
600	x														
585															
570															
555	x														
540		x													
525			x												
510		x													
495				x		x									
480					o		x				x		x		
465			x					x		o		o		x	
450									x						o
435				x				x							
420					x		o		x		x				x
405						o				o		x		x	
390													o		
375															

x = Failed; o = Run out; -- Full Density; -- Porous Ti Coated.

Table 6.4 reports the fatigue resistance calculated by using the stair case procedure.

Table 6.4 - Fatigue resistance of full density and porous Ti coated Co alloy.

Material	Failure Probability		
	10%	50%	90%
Sintering - Fully Dense	494	464 ± 7	451
Porous Ti Coated	419	405 ± 9	391

As it can be seen, the porous coating (scaffold) decreases the fatigue resistance down to 85% of the full density one. This drop in fatigue resistance is related to stress concentration close to the pores. But the porous cp-Ti coated Co-28Cr-6Mo material has a remarkable fatigue resistance that can be attributed to reduced notch sensitivity.

6.2 - Cp-Ti/Ti-6Al-4V

Co-sintered specimens were produced at 950 °C, 5 minutes and 45 MPa. Since no significant microstructural differences from the two materials when sintered alone were observed, sinter-bonding experiments were not carried out.

6.2.1. Microstructure

Fig. 6.11 shows the Ti-6Al-4V and the cp-Ti microstructures after co-sintering.

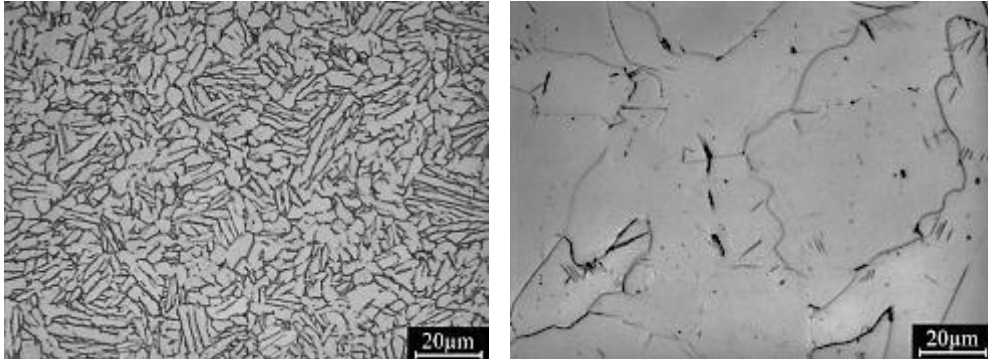


Fig. 6.11 - Microstructure of materials co-sintered. A) Ti-6Al-4V and B) Cp-Ti.

The Ti-6Al-4V microstructure consists of lamellar alpha phase plus interlaths beta phase, whilst the cp-Ti consists of alpha phase. The Ti alloy does not suffer grain growth due to the presence of beta phase, which prevents grain growth. At 950 °C the Ti alloy still not overcome the beta transus temperature [57]. On the other hand, grain growth takes place in the cp-Ti. Moreover, at 950 °C cp-Ti is into beta phase field. As the self-diffusion coefficient of beta Ti is higher than that of alpha Ti [57] grain growth is enhanced.

6.2.2 - Interface Characterization

Fig. 6.11 shows the interface region. On the left side the Ti-6Al-4V microstructure is constituted of alpha + beta phases, whilst in the right side the cp-Ti consists in alpha phase.

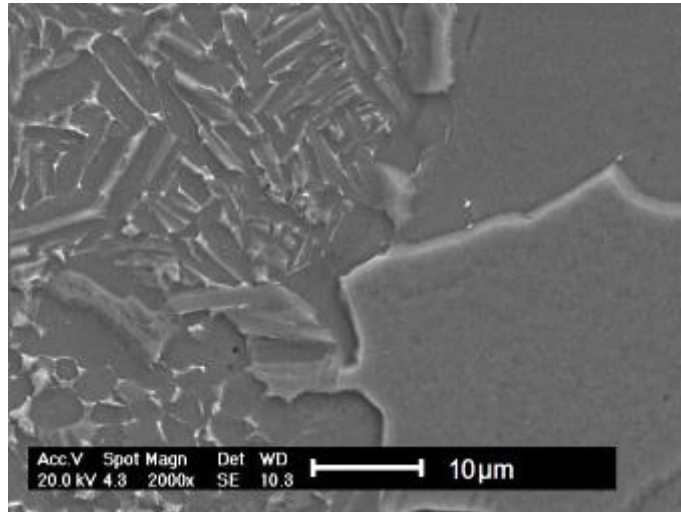


Fig. 6.11 – Microstructure at the interface between Ti-6Al-4V and cp-Ti after co-sintering.

The interface region is characterized by alloying elements diffusion from the Ti alloy towards to the cp-Ti. Fig. 6.12 shows an example of the EDXS line profile across the interface.

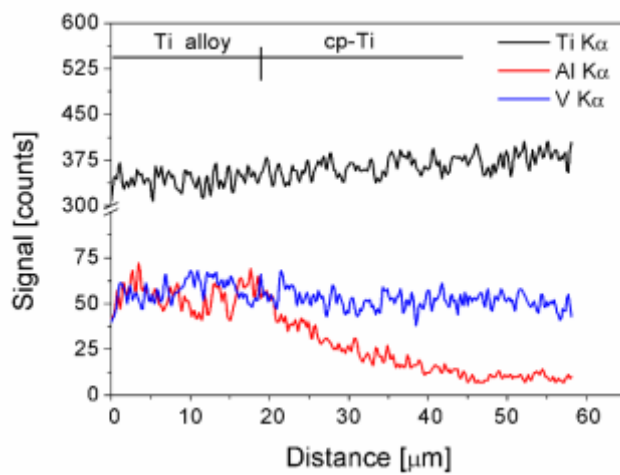


Fig. 6.12 - EDXS line profile analysis at the interface.

The Ti content increases from the Ti-6Al-4V alloy towards cp-Ti, whilst Al decreases gradually. The V profile is uncertain, since the V K α peak is situated right at the same energy of the Ti K β one. For a quantitative assessment, EDXS spot analyses every 10 μm from the interface were performed, as shown in Fig. 6.13.

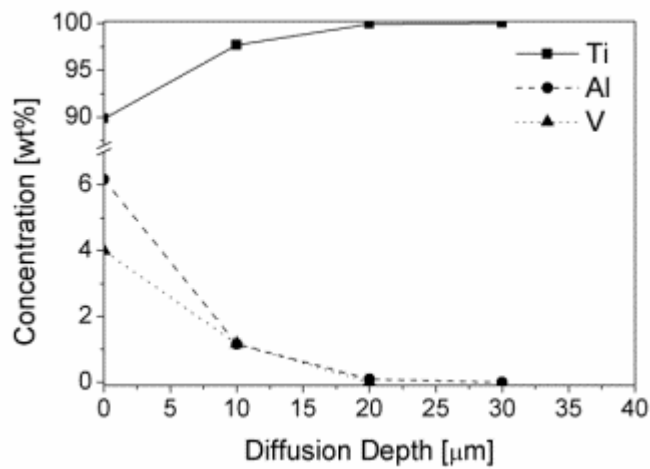


Fig. 6.13 - Diffusion profiles of Al and V into cp-Ti.

Here, V and Al present very similar and small diffusion depths, reaching 20 μm and 30 μm , respectively. In order to interpret the experimental results the diffusion distances were calculated using Equation 1 and Equation 2. The calculation considers the full concentration of the two elements in the Ti alloy: 6 wt.% for Al and 4 wt.% for V. Fig. 6.14 show the theoretical curves.

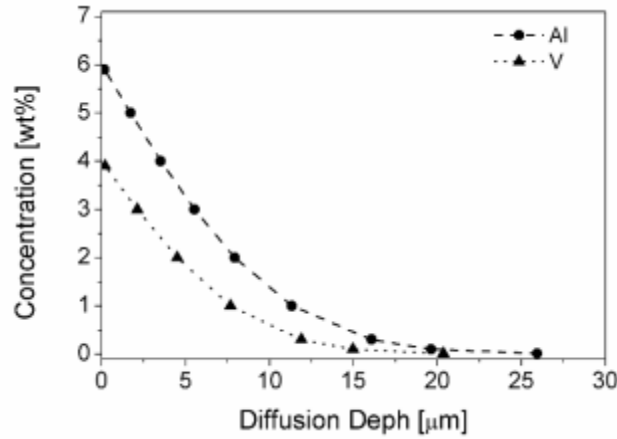


Fig. 6.14. Theoretical Al and V profile diffusion curves.

Frequency factor (D_0), activation energy (Q_d), diffusion coefficient (D), solubility (S) and the diffusion depth x at which the concentration of the elements is 0,01% are shown in Table 6.5.

Table 6.5. Frequency factor (D_0), activation energy (Q_d), diffusion coefficient (D), solubility (S), diffusion depth ($x_{0,01\%}$) of Al and V at 1223 K for 300 s in β -Ti

Elements	$D_0 \cdot 10^{-8}$ ($m^2 s^{-1}$)	Q_d (KJ mole $^{-1}$)	$D \cdot 10^{-13}$ (m^2/s)	S (wt. %)	$x_{0,01\%}$ (μm)
Al	0,14	91,7	1,12	6	26
V	600	170	0,74	100	21

Theoretical diffusion profiles satisfactorily fit the experimental data. In any case, aluminum diffuses more than vanadium as in accordance to experimental results.

6.2.2 - Fatigue Properties

Table 6.6 reports the results of the staircase procedure of the full density and the porous coated materials.

Table 6.6 - Staircase procedure of fully dense and porous coated materials

Stress (MPa)	1	2	3	4	5	6	7	8	9	10	11	12	13	14	15
595															
580															
565	x														
550															
535															
520		x													
505															
490			x		x						x			x	
475				o			x			o			o		
460						o			o			o			x
445								o							
430															
415															
400															
385															
370															
355															
340															
325															
310	x														
295															
280															
265															
250		x													
235															
220						x								x	
205			x		o		x		x				o		o
190				o				o		x		o			
175											o				
160															

x = Failed; o = Run out; -- Full Density; -- Porous Coated.

Table 6.7 reports the fatigue resistance calculated by using the staircase procedure.

Table 6.7 - Fatigue resistance of full density and porous coated materials.

Material	Failure Probability		
	10%	50%	90%
Sintering - Fully Dense	452	472 ± 13	493
Cp-Ti Porous Coated Ti Alloy	205	193 ± 8	181

The porous coating decreases the fatigue resistance significantly, as expected. It is known that both Co–Cr–Mo alloys and Ti–6Al–4V alloys experience reductions in fatigue strength when fabricated as porous coatings on solid core structures [122-125]. The decrease of fatigue resistance due to the porous layer is around 60%, similar to that reported by Cook [126] who found that the high cycle fatigue strength of porous coated Ti–6Al–4V alloy is approximately one-third that of the solid alloy [127]. Here, the decrease is slightly smaller.

6.3 - Summary of the Results

Co-sintering (Cp-Ti/Co-28Cr-6Mo):

- A noticeable reduction in the sintering efficiency in comparison to that obtained by sintering the two materials alone was observed on the Co alloy microstructure.
- The interface between materials is irregular due to the different hardness of the materials.

- Close to the interface the cp-Ti microstructure consists of a β -Ti layer of around 50 μm . From 50 μm a lamellar $\alpha+\beta$ layer up to a distance of around 200 μm is verified.
- Close to the interface the Co alloy microstructure does not undergo significant modification, but particles appear as only slightly deformed.

Sinter-bonding (Cp-Ti/Co-28Cr-6Mo):

- Sinter-bonding of Co alloy powder on the pre-sintered cp-Ti produces an interface less irregular than that in the case of co-sintering. The cp-Ti microstructure undergoes an extensive grain growth.
- Sinter-bonding of cp-Ti powder on pre-sintered Co alloy produces a quite flat interface. In this case, the Co alloy microstructure does not undergo an extensive grain growth. A very slight carbide dissolution was verified.
- The microstructure of the interface is similar to that of the co-sintered material: a β -Ti layer of around 50 μm and a lamellar $\alpha-\beta$ layer up to a distance of around 200 μm is verified.
- The Co, Cr and Mo, diffusion profile is comparable in all three cases (co-sintering and both cases of sinter-bonding).
- While titanium does not diffuse into Co alloy, the Co, Cr and Mo elements diffuse into cp-Ti.
- The total diffusion depth corresponds to about 200 μm . Mo, Cr and Co diffusion depths are about <25, 50 and 175 μm , respectively; they correspond to those calculated on the basis of the diffusion coefficients at the SPS temperature.
- Cobalt content was systematically higher in β lamellae, due to the cobalt partitioning during phase transformation.

- At higher magnification an interaction layer is revealed, 3-4 μm thin, and it is constituted by three sub-layers of about 1 μm thickness.
- The concentration profiles of Cr in the first layer and of Co in the second layer are not consistent with the concentration gradients, rather they result from a Darken's diffusion phenomenon driven by the activity of the elements in the three layers.
- The porous coating (scaffold) decreases the fatigue resistance down to 85% of the full density one.

Co-sintering (Cp-Ti/ Ti-6Al-4V):

- The Ti-6Al-4V microstructure consists of lamellar alpha phase plus interlaths beta phase, whilst the cp-Ti consists of alpha phase.
- The interface region is characterized by alloying elements diffusion from the Ti alloy towards to the cp-Ti; vanadium and aluminum present very similar and small diffusion depths, reaching 20 μm and 30 μm , respectively.
- Theoretical diffusion profiles satisfactorily fit the experimental data.
- The porous coating (scaffold) decreases the fatigue resistance down to 40% of the full density one.

Chapter 7 - CONCLUSIONS

This work was carried out in the frame of an industrial research project in cooperation with K4Sint Srl (Pergine Valsugana, Trento), and Eurocoating SpA (Pergine Valsugana, Trento). It was aimed at the development of the production of commercial pure titanium, Ti-6wt.%Al-4wt.%V (Ti-6Al-4V) and Co- 28wt.%Cr-6wt.%-Mo (Co-28Cr-6Mo) alloys by Spark Plasma Sintering for biomedical application.

The final objective was the definition of the process parameters for the production of a highly porous (cp-Ti), full density materials (Ti-6Al-4V and Co-28Cr-6Mo), and their combination in a surface functionalized full density substrate. The process parameters can be summarized as follow:

Co-28Cr-6Mo alloy: 900 °C, 5 minutes and 60 MPa;

Co-sintering of the cp-Ti/Co alloy: 1000 °C, 5 minutes and 60 MPa;

Co-sintering of the cp-Ti/Ti-6Al-4V alloy: 950 °C, 5 min. and 45 MPa;

As a general conclusion it may be assessed that the processing parameters for the production of the investigated biomaterials have been defined and the microstructural characteristics, as well as mechanical, corrosion properties and wear resistance satisfy the requirements on the international standards. The results have been used to produce implants which are under test.

REFERENCES

- [1] Sivakumar, R., On the relevance and requirements of biomaterials. *Bulletin of Materials Science*. 1999, 22 (3), 647-655.
- [2] Park, J.B., Lakes, R.S., *Biomaterials - An Introduction*, 2nd Ed, , London: Plenum Press, New York, (1992).
- [3] Bhat, S.V., *Biomaterials*, Alpha Science International Ltd., New Delhi, India, (2002).
- [4] Guelcher, S.A., Hollinger J.O., *An introduction to biomaterials*, 2nd Ed, CRC Press, New York, (2011).
- [5] Ratner, B.D., Hoffman, A. S., Schoen, F.J., and Lemons, J.E. (eds.), *Biomaterials science: an introduction to materials in medicine*, Elsevier Sci., New York, (1996).
- [6] Geetha M., Singh A.K., Asokamani R., Gogia A.K., Ti based biomaterials , the ultimate choice for orthopaedic implants – A review. *Progress in Materials Science*. 2008, 54 (3), 397-425.
- [7] Buttaro M.A., Mayor M.B., Van C.D., Piccaluga F., Fatigue fracture of a proximally modular, distally tapered fluted implant with diaphyseal fixation. *Journal of Arthroplasty*, 2007, 22, 780–783.
- [8] Lam L.O., Stoffel K., Kop A., Swarts E., Catastrophic failure of 4 cobalt-alloy fit hip arthroplasty femoral components. *Acta Orthopedic*, 2008, 79, 18-21.
- [9] Jacobs, J.J., Skipor, A.K., Black, J., Urban, R.M., and Galante, J.O., Release and excretion of metal in patients who have a total hip-replacement component made of titanium-base alloy. *Journal of Bone and Joint Surgery*, 1991, 73-A, 1475-1486.
- [10] Jacobs, J.J., Skipor, A.K., Black, J., Hastings, M.C., Schavocky, J., Urban, R.M., and Galante, J.O., Metal release and excretion from

cementless titanium total knee replacements. *Transactions of Orthopedic Research Society*, 1991, 16, 558-562.

[11] Black J., Hastings G.W., *Handbook of biomaterials properties*. Chapman and Hall; London, (1998).

[12] Pilliar R.M., Cameron H.U., Binnington A.G., Szivek J., Macnab., Bone ingrowth and stress shielding with a porous surface coated fracture fixation plate. *Journal of Biomedical Materials Research*, 1979, 13, 799-810.

[13] Yaszemski, M.J., *Biomaterials in Orthopedics*, Marcel Dekker Ltd., New York, (2003).

[14] Hoar T.P., Mears D.C., Corrosion resistant alloys in chloride solutions, materials for surgical implants. *Proceedings of the Royal Society of London*. 1966, 294, 486-493.

[15] Hallab N.J., Messina C., Skipor A., Jacobs J.J., Differences in the fretting corrosion of metal-metal and ceramic-metal modular junctions of total hip replacements. *Journal of orthopaedic research*, 2004, 22, 250-259.

[16] Gilbert, J.L., Buckley, C.A., and Jacobs, J.J., In vivo corrosion of modular hip prosthesis components in mixed and similar metal combinations. The effect of crevice, stress, motion, and alloy coupling. *Journal of Biomedical Materials Research*., 1993, 27, 1533-1544.

[17] Van Blitterswijk, C.A., Thomsen, P., *Tissue engineering*. Academic Press, London, (2008).

[18] Narayan R., *Biomedical Materials*. Springer Science, New York, 2009.

[19] Spiekermann H. *Implantology*. Quintessence: Color Atlas of Dental Medicine. Chicago, (1995).

[20] Zarb G.A., Albrektsson T. Osseointegration: a requiem for the periodontal ligament?, *International Journal Periodontal Research Dent*, 1991, 11, 88-91.

- [21] Le Guéhennec L, Soueidan A, Layrolle P, Amouriq Y. Surface treatments of titanium dental implants for rapid osseointegration. *Dental materials*. 2007, 23, 844-854.
- [22] Degischer H. P., Kriszt B. (Eds.), *Handbook of Cellular Metals*, Wiley, Weinheim, (2002).
- [23] Dunand D.C., Processing of Titanium Foams. *Advanced Engineering Materials*. 2004, 6 (6), 369-376.
- [24] Donachie M.J., *Advanced Materials Processing*, 1998, 7, 63-70.
- [25] Gibson L.J., *Journal of Biomechanics*, 2005, 38, 377-381.
- [26] Lorna J.G., Michael F.A., *Cellular Solids: Structure and Properties*, 2th Ed., Cambridge University Press, Cambridge, (1988).
- [27] Ryan G., Pandit A., Apatsidis D.P., Fabrication methods of porous metals for use in orthopaedic applications. *Biomaterials*. 2006, 27, 2651-2670.
- [28] Galante J., Rostoker W., Lueck R., Ray R.D., Sintered fiber metal composites as a basis for attachment of implants to bone. *Journal of Bone Joint Surgery*, 1971, 53 (A), 101-114.
- [29] Pilliar R.M., Surgical Prosthetic Device with porous metal coating, *US Patent 3,855,638*, 1974.
- [30] Cook S.D., Walsh K.A., Haddad Jr R.J., Interface mechanics and bone growth into porous Co–Cr–Mo alloy implants. *Clinical Orthopedic*, 1985, 271–280.
- [31] Dabrowski J.R., Use of powder metallurgy for development of implants of Co–Cr–Mo alloy powder. *Biomed Tech (Berlin)*, 2001, 46,106–108.
- [32] Amigo V., Salvador M.D., Romero F., Solves C., Moreno J.F., Microstructural evolution of Ti-6Al-4V during the sintering of microspheres of Ti for orthopedic implants. *Journal of Materials Processing Technology*. 2003, 141, 117-122.

- [33] Oh I.H., Nomura N., Masahashi N., Hanada S., Mechanical properties of porous titanium compacts prepared by powder sintering. *Scripta Materialia*, 2003, 49, 1197–1202.
- [34] Banhart J., Manufacture, characterization and application of cellular metals and metal foams *Progress in Materials Science*, 2001, 46, 559-632.
- [35] Ye B., Dunand D.C., Titanium foams produced by solid-state replication of NaCl powders. *Materials Science & Engineering A*. 2010, 528, 691-697.
- [36] Liang-jian C., Ting L.I., Yi-min L.I., Hao H.E., You-hua H.U., Porous titanium implants fabricated by metal injection molding. *Transaction of Nonferrous Metals Society of China*. 2009, 19, 1174-1179.
- [37] Esen Z., Bor S., Processing of titanium foams using magnesium spacer particles. *Scripta Materialia*. 2007, 56, 341-344.
- [38] Ibrahim A., Zhang F., Otterstein E., Burkel E., Processing of Porous Ti and Ti5Mn Foams by Spark Plasma Sintering. *Materials and Design*. 2010, 32, 146-153.
- [39] Xiong J., Li Y., Wang X., Hodgson P., Wen C., Mechanical properties and bioactive surface modification via alkali-heat treatment of a porous Ti-18Nb-4Sn alloy for biomedical applications. *Acta Biomaterialia*. 2008, 4, 1963-1968.
- [40] Bram M., Stiller C., Buchkremer H.P., Stöver D., Baur H., High-Porosity Titanium, Stainless Steel, and Superalloy Parts. *Advanced Engineering Materials*. 2000, 2 (4), 196-199.
- [41] Li X., Wang C., Zhang W., Li Y., Fabrication and characterization of porous Ti-6Al-4V parts for biomedical applications using electron beam melting process. *Materials Letters*. 2009, 63, 403-405.
- [42] Dinda G.P., Song L., Mazumder J., Fabrication of Ti-6Al-4V Scaffolds by Direct Metal Deposition. *Metallurgical and Materials Transactions A*. 2008, 39, 2914-2922.

- [43] Heini P., Muller L., Korner C., Singer R.F., Muller F.A., Cellular Ti-6Al-4V structures with interconnected macro porosity for bone implants fabricated by selective electron beam melting. *Acta Biomaterialia*. 2008, 4, 1536-1544.
- [44] Vandenbroucke B., Kruth J.P., Selective laser melting of biocompatible metals for rapid manufacturing of medical parts. *Rapid Prototyping Journal*, 2007, 13 (4), 196-203.
- [45] Donglu, Shi. *Introduction to Biomaterials*. Tsinghua University Press, Beijing, (2006).
- [46] Nordin M., Frankel V.H., *Basic Biomechanics of the Musculoskeletal System*. 3rd ed. Lippincott Williams & Wilkins, Philadelphia, (2001).
- [47] <http://training.seer.cancer.gov/anatomy/skeletal/tissue.html> on Feb. 2012.
- [48] Betteridge W., *Cobalt and Its Alloys*, Ellis Horwood Limited, London, (1982).
- [49] Davis J.R., *Nickel, cobalt and their alloys*. ASM International, Materials Park, OH , (2000).
- [50] Baboian R., *Corrosion Tests and Standards, Application and Interpretation*, 2nd ed., ASTM International, PA, (2005).
- [51] Huang P., Lopez H.F., Strain induced E-martensite in a Co-Cr-Mo alloy: grain size effects. *Materials Letters*. 1999, 39, 244-248.
- [52] Lopez H.F., Saldivar-Garcia A.J., Martensitic Transformation in a Cast Co-Cr-Mo-C Alloy. *Metallurgical and Materials Transactions A*. 2008; 39, 8-18.
- [53] Huang P., Liu R., Wu X.J., Yao M.X., Effects of Molybdenum Content and Heat Treatment on Mechanical and Tribological Properties of a Low-Carbon Stellite Alloy, *Journal of Engineering Materials and Technology*, 2007, 129 (4), 523-529.

- [54] Dobbs H. S., Robertson J. L. M., Heat Treatment of Cast Co-Cr-Mo for Orthopaedic Implant Use. *Journal of Materials Science*, 1983, 18, 391-401
- [55] Daud Z.C., Jamaludin S.B., Bari F., Characterization of Co-28Cr-6Mo Alloy Produced by Solid State Sintering. *Advanced Materials Research*. 2011, 173, 106-110.
- [56] Muterlle P., Zendron M., Zanella C., Perina M., Bardini R., Molinari A., Effect of microstructure on the properties of a biomedical Co-Cr-Mo alloy produced by MIM, *Advances in Powder Metallurgy & Particulate Materials*, 2009, 1 (4), 60-69.
- [57] Gaytan S.M., Murr L.E., Martinez E., Martinez J.L., Machado B.I., Ramirez D.A., Medina F., Collins S., Wicker R.B. Comparison of Microstructures and Mechanical Properties for Solid and Mesh Cobalt-Base Alloy Prototypes Fabricated by Electron Beam Melting. *Metallurgical and Materials Transactions A*. 2010, 41 (12), 3216-3227.
- [58] Vandenbroucke B., Kruth J.-P., Selective laser melting of biocompatible metals for rapid manufacturing of medical parts. *Rapid Prototyping Journal*, 2007, 13 (4), 196-203.
- [59] Ogden, H.R., in: A.H. Clifford (Ed.), *Rare Metals Handbook*, Rinhdd Publishing Corporation, Chapman & Hall Ltd., London, (1961).
- [60] Collings E.W., *The physical metallurgy of titanium alloys*, in: H.L. Gegel (Ed.), *ASM Series in Metal Processing*, Edward Arnold Publications, Cleveland, Metals Park, OH, (1984).
- [61] C. Leyens, M. Peters, *Titanium and Titanium Alloys*, Wiley-VCH, Cologne, 2003.
- [62] Prasad Y.V.R.K., Sasidhara S., (Eds.), *Hot Working Guide: A Compendium of Processing Maps*, ASM International, Materials Park, OH, (1997).
- [63] Polmear J.J., *Titanium alloys*, in: *Light Alloys*, Edward Arnold Publications, London, (1981).

- [64] Lütjering G., Williams J.C.: *Titanium, Engineering Materials and Process*, Springer, Berlin, Germany,(2003).
- [65] Bania P.J., in: D. Eylon, R.R. Boyer, D.A. Koss (Eds.), *Titanium Alloys in the 1990's*, The Mineral, Metals & Materials Society, Warrendale, PA, (1993).
- [66] Donachie, M. J., *Titanium - a Technical Guide*, 2° Ed., ASM, Metals Park, OH, (2000)
- [67] Schutz R.W., in: D. Eylon, R.R. Boyer, D.A. Koss (Eds.), *Beta Titanium Alloys in the 1990's*, The Mineral, Metals& Materials Society, Warrendale, PA, (1993).
- [68] Norgate T.E., Wellwood G. The Potential Applications for Titanium Metal Powder and Their Life Cycle Impacts. *JOM*. (2006);September, 58-63.
- [69] Moxson VS, Senkov ON, Froes FH. Innovations in Titanium Powder Processing. *JOM*. 2000; May, 24-26.
- [70] ASM Handbook, *Volume 7 Powder Metal Technologies and Applications*. 2nd Ed., Materials Park, ASM International, OH, 1998.
- [71] Shibo G, Xuanhui Q, Xinbo H, Ting Z, Bohua D., Powder injection molding of Ti-6Al-4V alloy. *Journal of Materials Processing Technology*. 2006;173:310-314.
- [72] Facchini L., Magalini E., Robotti P., Molinari A., Microstructure and mechanical properties of Ti-6Al-4V produced by electron beam melting of pre-alloyed powders", *Rapid Prototyping Journal*, Vol. 15 (3), 2009, 171 – 178.
- [73] Facchini L., Magalini E., Robotti P., Molinari A., Hoges S., Wissenbach K., Ductility of a Ti-6Al-4V alloy produced by selective laser melting of prealloyed powders, *Rapid Prototyping Journal*, 16 (6), 2010, 450–459.

- [74] Zadra M., Casari F., Girardini L., Molinari A., Microstructure and Mechanical Properties of CP-Titanium Produced by Spark Plasma Sintering, *Powder Metallurgy*, 51 (1), 2008, 59-65.
- [75] Taylor G.F., Apparatus for Making Hard Metal Compositions, U.S. Patent 1,896,854, 1933.
- [76] Cremer G.D, US Patent No. 2,355,954, 1944.
- [77] Lenel V. F, Transactions of AIME 203, 1955, 158
- [78]. Shon I. J., Munir Z.A., *Materials Science Engineering A*, 1995, 202, 256.
- [79] Xie G., Ohashi O., Song M., Mitsuishi K., Furuya K., *Applied Surface Science*, 2005, 241, 102.
- [80] Goldberger W.M., Merkle B., Boss D., *Advanced Powder Metallurgy and Particulate Materials*, 1994, 6, 91.
- [81] Tokita M., *Materials Science Forum*, 1999, 83, 308–311.
- [82] Hulbert D.M., Anders A., Andersson J., Lavernia E.J., Mukherjee A.K., A discussion on the absence of plasma in spark plasma sintering. *Scripta Materialia*. 2009, 60, 835-838.
- [83] Lee J.W., Munir Z.A., Shibuya M., Ohyanagi M., *Journal of American Ceramic Society*, 2001, 84 (6), 1209-1216
- [84] Groza J.R., Zavaliangos A., Sintering activation by external electrical field. *Materials Science and Engineering A*. 2000, 287, 171-177.
- [85] Anderson K.R., Groza J.R., Fendorf M., Echer C.J., Surface oxide debonding in field assisted powder sintering. *Materials Science and Engineering A*. 1999, 270, 278-282.
- [86] Chen W., Anselmil-Tamburini U., Garay J.E., Groza J.R., Munir Z.A., Fundamental investigations on the spark plasma sintering / synthesis process I . Effect of dc pulsing on reactivity, *Materials Science and Engineering A*, 2005, 394, 132-138.

- [87] Song X., Liu X., Zhang J., Neck formation and self-adjusting mechanism of neck growth of conducting powders in spark plasma sintering, *Journal of the American Ceramic Society*, 2006, 89 (2), 494–500.
- [88] Diouf S., Molinari A., Densification mechanisms in spark plasma sintering: Effect of particle size and pressure. *Powder Technology*. 2012, 221, 220-227.
- [89] Anselmi-tamburini U., Gennari S., Garay J.E., Munir Z.A., Fundamental investigations on the spark plasma sintering / synthesis process II . Modeling of current and temperature distributions. *Materials Science and Engineering A*. 2005, 394, 139-148.
- [90] Eriksson M., Shen Z., Nygren M., Fast densification and deformation of titanium powder. *Powder Metallurgy*. 2005, 48 (3), 231-236.
- [91] Matsugi K, Kuramoto H, Yanagisawa O, Kiritani M., A case study for production of perfectly sintered complex compacts in rapid consolidation by spark sintering. *Materials Science and Engineering A*. 2003, 354, 234-242.
- [92] Lutterotti L., Matthies S., Wenk H.R., Shultz A.S., Richardson J.W., Combined texture and structure analysis of deformed limestone from time-of-flight neutron diffraction spectra. *Journal of applied physics*, 1997, 81, 594-600.
- [93] Lonardelli I., Wenk H.R., Lutterotti L., Goodwin M., Texture analysis from synchrotron diffraction images with the Rietveld method: dinosaur tendon and salmon scale. *Journal of Synchrotron Radiation*, 2005, 12, 354-360.
- [94] Liu X., Chu P.K., Ding C., Surface modification of titanium, titanium alloys, and related materials for biomedical applications. *Materials Science and Engineering R*. 2004, 47, 49-121.
- [95] Lowenberg B.F., Pilliar R.M., Aubin J.E., Sodek J., Melcher A.H., Cell attachment of human gingival fibroblasts in vitro to porous-surfaced

- titanium alloy discs coated with collagen and platelet-derived growth factor. *Biomaterials*. 1988, 9, 302-309.
- [96] Eriksson M., Andersson M., Adolfsson E., Carlström E., Titanium - hydroxyapatite composite biomaterial for dental implants. *Powder Metallurgy*. 2006, 49 (1), 70-77.
- [97] Cordonnier T., Sohier J., Rosset P., Layrolle P., Biomimetic Materials for Bone Tissue Engineering – State of the Art and Future Trends . *Advanced Biomaterials*. 2011, 13, 1-16.
- [98] Chen J., Paetzell E., Zhou J., Lyons L., Soboyejo W., Osteoblast-like cell ingrowth, adhesion and proliferation on porous Ti-6Al-4V with particulate and fiber scaffolds. *Materials Science and Engineering C*. 2010, 30, 647-656.
- [99] Ji H., Marquis P.M., Effect of heat treatment on the microstructure of plasma-sprayed hydroxyapatite coating, *Biomaterials*, 1993, 14 (1), 64-68.
- [100] Wei M., Ruys A.J., Swain M.V., Milthorpe B.K., Sorrell C.C., Hydroxyapatite-coated metals: Interface reactions during sintering, *Journal of Materials Science: Materials in Medicine*, 2005, 16, 101-106.
- [101] Fleck N.A., Smith R.A., Effect of density on tensile strength, fracture toughness, and fatigue, crack propagation behavior of sintered steel. *Powder Metallurgy*, 1981, 24, 121-125.
- [102] Kumar P., *Elements of fracture mechanics*, Wheeler Publishing, New Delhi, (1999).
- [103] Hanawa T., Metal ion release from metal implants. *Materials Science Engineering C*, 2004, 24, 745–52.
- [104] España F.A., Balla V.K., Bose S., Bandyopadhyay A., Design and fabrication of CoCrMo alloy based novel structures for load bearing implants using laser engineered net shaping. *Materials Science & Engineering C*. 2010, 30, 50-57.

- [105] Chiba A., Kumagai K., Takeda H., Nomura N., Mechanical Properties of Forged Low Ni and C- Containing Co-Cr-Mo Biomedical Implant Alloy, *Materials Science Forum*, 2005, 475-479, 2317-2322.
- [106] Ishida K., Nishizawa T., The C–Co (carbon–cobalt) system, *Journal of Phase Equilibria*, 1991, 12, 417–424.
- [107] Huang P., Lopez H.F., Athermal ϵ -martensite in a Co-Cr-Mo alloy: grain size effects. *Materials Letters*, 1999, 39, 249-253.
- [108] Guillard F., Allemand A., Lulewicz J-daniel, Galy J., Densification of SiC by SPS-effects of time , temperature and pressure. *Journal of the European Ceramic Society*. 2007, 27, 2725-2728.
- [109] Maglia F., Anselmi-Tamburini U., Chiodelli G., Electrical, structural, and microstructural characterization of nanometric $\text{La}_{0.9}\text{Sr}_{0.1}\text{Ga}_{0.8}\text{Mg}_{0.2}\text{O}_{3-\delta}$ (LSGM) prepared by high-pressure spark plasma sintering. *Solid State Ionics*. 2009, 180 (1), 36-40.
- [110] Munir Z.A., Anselmi-tamburini U., Ohyanagi M., The effect of electric field and pressure on the synthesis and consolidation of materials: A review of the spark plasma sintering method. *Journal of Materials Science*. 2006, 41, 763-777.
- [111] Shen Z., Johnsson M., Zhao Z., Nygren M., Spark Plasma Sintering of Alumina, *Journal of the American Ceramic Society*, 2002, 85 (8), 1921-1927
- [112] Lopez G.D., Biodeterioration and corrosion of metallic implants and prostheses. *Medicina (B Aires)* 1993, 53 (3), 260–74.
- [113] Steinemann S., *Corrosion of Implant Alloys. Technical Principles, Design and Safety of Joint Implants*. Hogrefe & Huber Publ., Seattle-Toronto-Bern-Göttingen, (1990).
- [114] Molinari A., Zadra M., Influence of the sintering temperature on microstructure and tensile properties of Ti6Al4V produced by Spark Plasma Sintering, PM2008.

- [115] Kundu S., Chatterjee S., Diffusion bonding between commercially pure titanium and micro-duplex stainless steel. *Materials Science and Engineering A*, 2008, 480, 316-322.
- [116] Kundu S., Ghosh M., Chatterjee S., Diffusion bonding of commercially pure titanium and 17-4 precipitation hardening stainless steel. *Materials Science and Engineering A*, 2006, 428, 18–23.
- [117] Ghosh M., Chatterjee S.. Diffusion bonded transition joints of titanium to stainless steel with improved properties. *Materials Science and Engineering A*, 2003, 358, 152-158.
- [118] Ghosh M., Bhanumurthy K., Kale G.B., Krishnan J., Chatterjee S.. Diffusion bonding of titanium to 304 stainless steel. *Journal of Nuclear Materials*, 2003, 322, 235–241.
- [119] Hood G. M.. The mechanisms of diffusion in the anomalous BCC metals. *Journal of Physics F: Metal Physics*, 1976, 6, 19-26.
- [120] Metals Handbook, *Alloy Phase Diagram* , 3 Ed., ASM International, Materials Park, OH, (1992).
- [121] Gupta A., *Journal of Phase Equilibria*, 2001, 22, 52-59.
- [122] Yue S., Pilliar R.M., Weatherly G.C., The fatigue strength of porous-coated Ti–6% Al–4%V implant alloy. *Journal of Biomedical Materials Research*, 1984, 18, 1043–58.
- [123] Kohn D.H., Ducheyne P., A parametric study of the factors affecting the fatigue strength of porous coated Ti–6Al–4V implant alloy. *J Biomed Mater Res* 1990;24:1483–501.
- [124] Crowninshield R.D., Mechanical properties of porous metal total hip prostheses. *Instructural Course Lecture*, 1986, 35, 144–148.
- [125] Manley M.T., Kotzar G., Stern L.S., Wilde A., Effects of repetitive loading on the integrity of porous coatings. *Clinical Orthopedic Relator Research*, 1987, 293–302.

[126] Cook S. D. *et al.*, *Journal of Biomedical Materials Research*, 1988, 22, 287-302.

[127] Wolfarth D, Ducheyne P., Effect of a change in interfacial geometry on the fatigue strength of porous-coated Ti-6Al-4V. *Journal of Biomedical Materials Research*, 1994, 28, 417-425.

ACKNOWLEDGEMENTS

My acknowledgments to the whole group of professors, technicians and secretaries of the University of Trento, in particular those from the Department of Materials Engineering and Doctoral School in Materials Engineering.

I wish to precise my all respect and my special gratitude to my supervisor, Prof. Dr. Alberto Molinari.

This project was co-founded by the *Eurocoating Spa*, my sincere thanks for such confidence. I would like to thank Francesco Bucciotti and Luca Facchini, whose are collaborators in this company.

I would like to thank Francesco Casari, from K4Sint, for discussions and cooperation.

Special thanks also to all laboratory colleagues, especially to Anna Fedrizzi, Melania Pilla, Ketner Bendo Demetrio, Palloma Mutterle Vieira, Ligia Dione da Costa, Cinzia Menapace, Lorena Maines, Saliou Diouf, Elena Santuliana, Ivan Lonardelli, Ibrahim Metinoz, Marco Cazzolli and László Lábiscsák.

I wish to express my love and gratitude to my family, my awesome wife and friends.

PUBLICATIONS

(concerning the thesis)

N. Vicente, F. Casari, F. Bucciotti, A. Molinari. *“Microstructures and tensile properties of Co₂₈Cr₆Mo alloy produced by Spark Plasma Sintering”*. PM2011, European Congress & Exhibition, Shrewsbury UK: EPMA, 2011, Vol. 2, p. 483-488.

N. Vicente, A. Fedrizzi, N. Bazzanella, F. Casari, F. Bucciotti, A. Molinari. *“Microstructural interface investigation between Ti and Co-Cr-Mo alloy co-sintered and sinter-bonded by Spark Plasma Sintering”*. MATERIALS CHARACTERIZATION. [Submitted 17th Feb 2012]

(during the doctorate)

L. Facchini, N. Vicente, I. Lonardelli, A. Molinari. *“Metastable austenite in 17-4 precipitation hardening stainless steel produced by selective laser melting and its effect on tensile properties”*. ADVANCED ENGINEERING MATERIALS, 2010, Vol. 12 (3), p. 184-188.

N. Vicente, I. Lonardelli, E. Magalini, A. Molinari. *“Strain hardenability of metastable 17-4PH Stainless Steel produced by Selective Laser Melting”*. PM2010, World Congress & Exhibition, Shrewsbury UK: EPMA, 2010, p. 195-200.

L. D. Da Costa, A. P. G. Nogueira, N. Vicente, G. Straffelini. *“Characterization of magnesium AZ91 alloy and AZ91 alloy with rare earth elements addition produced via Spark Plasma Sintering”*. Proceedings SENAFOR, Porto Alegre, Brazil, 2010.

C. Menapace, N. Vicente, A. Molinari. *"Forging of Spark Plasma Sintered Ti64 Powder Preforms"*. PM2011, European Congress & Exhibition, Shrewsbury UK: EPMA, 2011, Vol. 3, p. 339-344.

N. Vicente, C. Menapace, A. Molinari. *"Hot deformation of the Ti-6Al-4V alloy preforms obtained by Spark Plasma Sintering of powders"*. COBEM2011, Brazilian Congress in Mechanical Engineering, CD-ROM , 2011, Paper 18741.

C. Zanella, N. Vicente, F. Casari, A. Molinari., F. Deflorian. *"Electrochemical behavior of CoCrMo biomedical alloy in presence of localized impurities"*. ICC, International Corrosion Congress; 2011, Paper 416.

C. Menapace, N. Vicente, A. Molinari. *"Hot forging of Ti6Al4V alloy preforms produced by Spark Plasma Sintering of powders"*. POWDER METALLURGY. [Accepted 28th Jan 2012].